Shear-induced Phenomena of a Collapsed Polymer

im Fachbereich Physik der Freien Universität Berlin
eingereichte Dissertation

zur Erlangung des akademischen Grades
eines Doktors der Naturwissenschaften (Dr. rer. nat.)

vorgelegt von

Matthias Radtke

Berlin, 2015

Erster Gutachter:	Prof. Dr. Roland R. Netz, Freie Universität Berlin
Zweiter Gutachter:	Prof. Dr. Joachim Dzubiella, Helmholtz-Zentrum Berlin Humboldt-Universität zu Berlin
Tag der Disputation:	2. März 2016

Contents

Chapter 1

Introduction and Outline

Biopolymers like nucleic acids, polysaccharides and proteins are of central importance in all biological processes. These chain-like macromolecules consisting of covalently bond repeating units exhibit extraordinary features due to the vast number of conformational degrees of freedom. The various biological functions of biopolymers are closely related to the specific spatial structure. It is determined by the chemical composition, specifically the primary structure and the presence of charged groups that account for physical properties like the degree of flexibility and topological constrains. The advances in the field of polymer physics are therefore partially driven by the ambition to understand complex biological phenomena and processes based on polymers as one of the basic components of all living organisms [1, 2].

Many molecular processes involving biopolymers are associated with static polymer properties such as the average size of coiled chains or collapsed globules. In this context, a prominent example is the self-assembly of proteins into their functional native state that can be described as a folding transition from coiled into globular polymer conformations. While dynamical properties of dilute polymer solutions are mainly governed by hydrodynamic interactions, the viscoelastic behavior of polymer melts consisting of long chains is determined by entanglement effects [3]. Fundamental interest in non-equilibrium dynamics of polymer systems is derived from such extraordinary rheological phenomena as non-Newtonian thinning and thickening of polymer solutions and melts in response to shear flow [4]. Another important aspect is the relevance for industrial and technological application. In particular, synthetic polymers are designed to mimic the behavior of the complex biopolymers that nature has evolved. A fundamental understanding of the remarkable dynamical features of polymeric systems is indispensable in order to develop novel polymer-based materials with potential self-healing properties, controlled response to flow and stress, or targeted drug delivery systems [5–7].

The present dissertation seeks to contribute to the understanding of a specific complex biological system, the blood protein von Willebrand factor (VWF). The main focus lies on the non-equilibrium dynamical aspects of multimeric proteins when subject to flow conditions, as it is the case in the bloodstream. From a fundamental point of view, non-equilibrium behavior of multimeric proteins raise a number of interesting questions in theoretical polymer physics. On the biological side, the flow-response of proteins in solution has important implications on the protein function, the interactions with

other objects (e.g. aggregation), the interaction with interfaces (adsorption), as well as degradation. Biophysical research in this field led to the discovery of novel phenomena such as reversible polymer-colloid aggregate formation in flow [8], catch bond behavior of special bond complexes [9], and shear-induced adhesion and degradation [10], all of which remain to be fully understood.

1.1 Von Willebrand factor and blood coagulation

The multimeric glycoprotein von Willebrand factor (VWF) is one of the largest proteins in the human body. It plays an essential role in the initiation of primary hemostasis, where platelets form a plug at the site of an injury of a damaged blood vessel in order to stop bleeding [11, 12]. VWF also acts as a carrier protein preventing the degradation of factor VIII [13], another essential blood clotting protein. Endothelial cells line the blood vessels and contain Weibel-Palade bodies, which are the main storage of VWF [14, 15].

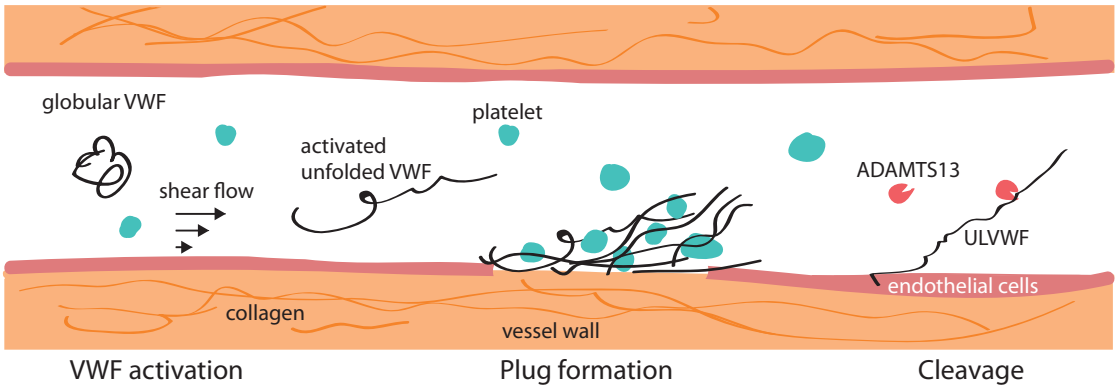

Figure 1.1: Schematic illustration of important VWF associated processes in the bloodstream. Shear flow activates VWF (black) by an unfolding transition from a globular configuration to an elongated state. At a site of an injury, VWF initiates the coagulation cascade by adhering to the exposed collagen and simultaneously mediating plug formation of platelets (green). The protease ADAMTS13 (red) presents the size regulatory mechanism that cleaves ultra large von Willebrand factor (ULVWF) after secretion from the endothelial cells as well as VWF circulating in the bloodstream and thus prevents pathological thrombus formation.

Upon stimulatory conditions VWF is secreted into the blood flow in an ultra large form [15, 16] that has to be cleaved by ADAMTS13 [17]. This process is schematically illustrated on the right hand site of in fig. 1.1. The cleavage enzyme represents the regulatory mechanism for the length of VWF and prevents spontaneous VWF-platelet aggregation that might lead to pathogenic thrombus formation. Prior to VWF degradation the A2 domain opens and exposes the cleavage site for ADAMTS13 [18, 19]. The exponential size distribution of VWF, which is controlled by ADAMTS13, has been determined recently experimentally [20].

A number of diseases are connected to the length distribution of VWF in the blood plasma. It is important to note that only long multimers of more than ten repeating units are hemostatically active. Whereas the relatively common bleeding disorder von Willebrand disease (VWD) can be caused by a quantitative VWF deficiency due to mutations and a lack of long VWF multimers [21, 22], a defect of the VWF-specific cleavage enzyme ADAMTS13 may lead to abnormally long multimers with a high potential of platelet binding and consequently to life threatening thrombotic thrombocytopenic purpura [23].

VWF's monomeric unit consists of 2050 amino acids [24] and is structured in multiple domains which are related to different functions [11, 16, 24]. As schematically illustrated in fig. 1.2a, there are binding sites for platelet's glycoprotein Ib (GPIb) [25], collagen [26], factor VIII [13] as well as sites for dimerization and multimerization, and a cleavage site for ADAMTS13 [17, 27]. During the biosynthesis in the endothelium, dimers are formed, shown in fig. 1.2b, which constitute the repeating units that are assembled to the VWF biopolymer, as shown in fig. 1.2c. The average size of these dimers is about 70 nm and 10 nm along the long and the short axis, respectively [28, 29], but depending on conditions like the pH, a maximal length up to 82 nm [17] is observed. VWF multimers in the bloodstream reach up to $40 - 200$ repeating units corresponding to contour length of $3 - 14\,\mu$m [27].

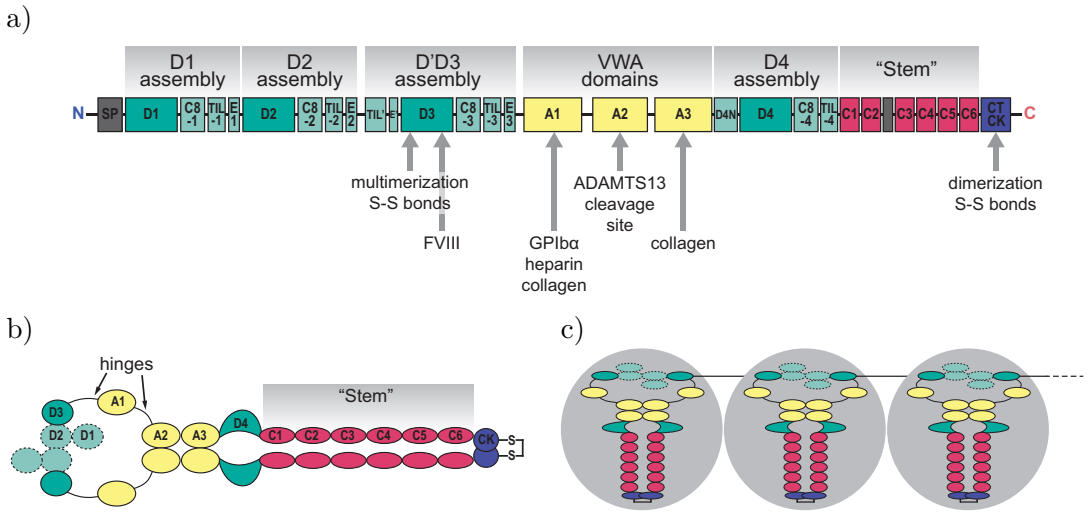

Figure 1.2: a) Von Willebrand factor domain annotations and attributed binding sites [24]. b) Schematic structure of the dimerized VWF repeating unit that form the c) multimeric protein. In coarse-grained simulations, VWF dimers are typically represented by spherical beads (gray) that are connected to a chain and interact effectively via pairwise Lennard-Jones potentials.

Under normal blood flow conditions VWF has a globular inactive form but in elevated hydrodynamic shear stress, as found in small vessels [30] or at vasoconstriction sites caused by injuries, it unfolds and thereby becomes activated [16, 31], see fig. 1.1. Note

that throughout this work the focus lies on the response of VWF polymers on mechanical stress but also chemical activation is possible, e.g. a variation of the pH will change the critical shear rate of unfolding [16]. The VWF activation occurs exactly in situations where needed, most importantly at a lesion in the vessel wall where subendothelial collagen is exposed, as schematically depicted in the middle of fig. 1.1. The elongated VWF can bind via a large number of binding sites to the collagen and thus initiates the coagulation cascade [32]. In the next step platelets adhere and form a VWF-mediated agglomeration, which finally becomes stable by a cross-linked network formation of fibrin, a complex process which involves a number of further clotting factors like thrombin and factor VIII. The detailed mechanisms of blood coagulation consists of a large number of chemical and physical processes which are far from being fully understood.

1.2 Polymers in shear flow

The physics of polymer systems can be probed experimentally in a collective manner with light [33] or neutron [29] scattering that yield ensemble-averaged information of the polymer configurations. More insight into the microscopic dynamics in biological systems was made possible by recently developed experimental techniques for the observation of single cells or molecules [34, 35]. As an example, fluorescent labels are used to track the motion of individual molecules within living cells with high spatial and temporal resolution microscopy [36]. Fluorescence correlation spectroscopy (FCS) analyzes fluctuations of the fluorescence intensity in a confocal volume [37, 38] and can be used to measure the dynamics of molecules in crowded environments [39] such as blood plasma [20]. Since many biological processes are governed by the force response of soft matter objects, a common way to resolve the underlying molecular mechanism is to either directly applying external stretching forces, e.g. by atomic force microscopy and optical tweezers [40], or by the study of the system dynamics in shear flow. Shear flow represents a commonly generated non-equilibrium condition as it occurs when a fluid flow passes a solid boundary, a situation ubiquitous in experimental setups such as microfluidic devices with a high surface to volume ratio.

From a theoretical point of view, polymers in a dilute solution are usually studied based on the description of single chains since for sufficiently low concentration the inter-polymer interactions can be neglected. The physical description of the chain mainly relies on methods from statistical mechanics [1]. Static properties of simple polymer models such as the bead-spring model which might include chain stiffness, excluded volume effects and different solvent conditions are described in detail in introductory chapters of numerous books on the topic [2, 3, 41]. In particular, good solvents tend to swell the polymer chain as the effective interaction between monomers is repulsive. In bad solvents the interaction is attractive and the polymer collapses with a minimal size determined by steric effects [42]. Concerning the dynamical behavior of single polymers, Rouse [43]

presented the first model for ideal, flexible chains, which was later expanded by Zimm [44] by inclusion of hydrodynamic interactions between monomers.

The dynamics of a single polymer in good solvent subject to simple shear flow is a well-studied problem. Theoretical descriptions primarily use dumbbell models, introduced by de Gennes [45], in order to examine dynamic quantities such as viscosity and rotational frequencies [46–48]. The average chain extension was predicted to increase continuously with increasing shear rate as it is observed in experiments [33, 49, 50]. For large shear rates non-monotonic stretching effects can be observed [51], i.e. polymer compression occurs reflected in a minimum of the average extension, which saturates for higher shear at about forty percent of the contour length [4]. Whereas de Gennes [45] predicted a continuous transition in simple shear flow from coiled to stretched polymer configurations, a polymer subject to elongational flow undergoes a first order coil-stretch transition at a critical value of the strain rate [52–54].

In terms of its time-dependent configuration a polymer in shear flow does not reach a stationary state as periodic elongation and relaxation with large fluctuations in the extension occur. Furthermore, end-over-end tumbling is observed for shear rates even smaller than the inverse polymer relaxation time [49, 50]. A similar behavior is observed for surface-grafted polymers [55]. It can be rationalized by decomposing simple shear flow into equal amounts of rotational and elongational flow in which the polymer is rotated and thus subject to periodic compressional and elongational flow.

Polymers dissolved in bad solvents collapse and form globules. Understanding the dynamical behavior of polymeric globules is important for instance in the context of the stability of folded proteins in shear flow [56, 57]. As opposed to polymers in good solvent, high cohesion opposes hydrodynamic drag forces, causing a different dynamical behavior. It is for this reason that the unfolding in simple shear flow is a smooth transition for good solvents [45], but collapsed polymers in bad solvent conditions unfold above a well-defined critical shear rate [58] as discussed in the following.

The force response of globular polymers was first theoretically examined by application of extensional forces on the polymer ends, where a first-order like unfolding transition at a critical force was characterized [59]. A similar discontinuous transition was found for the case of grafted collapsed polymers in shear flow above a critical shear rate [60]. Since relaxation of stretching forces on unconstrained globules in shear flow occurs due to the rotation, the mechanism for shear-induced unfolding is different. Studies of Alexander-Katz and Netz [58, 61] showed that thermally excited protrusions from the globular surface induce the unfolding mechanism of free, nongrafted polymeric globules in shear. At a critical shear rate the hydrodynamic drag force on a protrusion overcomes the restoring cohesive force and the polymer is able to fully elongate. The scaling analysis of this nucleation model reveals a different dependence of the critical shear rate on the globule size for free draining conditions compared to the non-draining case, i.e. there is flow stagnation within the globule when hydrodynamic interactions are taken into account. The dependence of the protrusion-induced instability mechanism on temperature

and the monomer size was also worked out. As a matter of fact, the dependence of the critical shear rate on the monomer size explains why the VWF with its large repeating units unfolds at physiologically relevant shear rates [31]. Furthermore, it was shown that the presence of a surface presenting a hydrodynamic no-slip boundary enhances the globule unfolding in shear [62], which corroborates the shear-induced VWF activation near vessel walls. This stands in contrast to many earlier studies where hydrodynamic interactions where neglected with the argument that close to a no-slip surface long-ranged hydrodynamic interactions are screened [63].

In general, hydrodynamic interactions of particles in the presence of a no-slip boundary at a surface become relevant when considering non-equilibrium properties such as the adsorption behavior of polymers in shear flow. Numerous studies investigate polymer adsorption in shear flow under good solvent conditions by means of simulations [64–69], experimentally [70, 71] as well as analytically [72–74]. But less attention received the case of collapsed polymer adsorption under shear [75, 76].

1.3 Shear-induced adhesion

Analytical theories predict that the adsorption of soft compact objects such as vesicles or platelets on a surface under flow conditions is suppressed by hydrodynamic lift forces [77, 78]. This result was experimentally confirmed for droplets [79] and adhering vesicles and leukocytes in shear flow, which roll and detach from the surface at a critical shear rate and remain unbound for stronger flow [80, 81]. Similar behavior is observed for flexible polymers [48, 82–84], which experience a shear-induced repulsion from the surface caused by the hydrodynamic interactions. Adsorption of such deformable objects is thus typically suppressed by shear flow.

By contrast, experiments on adhesion of platelets mediated by VWF show the opposite behavior, i.e. adsorption is enhanced by elevated shear rates [85]. Also the initial deposition of VWF polymers on a collagen substate was shown to exhibit such a counterintuitive behavior of shear-induced adsorption [31]. It transpires that a more complex binding mechanism might play a role in the force response of such systems. In fact, there is experimental evidence for catch bond [86] or flex bond [87] behavior of the receptor ligand complex between the VWF A1 domain and platelets GPIbα. Most biological bonds consist of a receptor and a corresponding ligand and display the intuitive behavior of decreased lifetime upon application of tensile forces [88]. The monotonic behavior of the average bond lifetime of such slip bonds is shown in fig. 1.3a as a green dashed line. In contrast, some biological bonds undergo a transition from a weak state to a strong and long-lived state upon applied tensile force [9, 89], a so-called catch bond behavior [90]. The corresponding average bond lifetime, shown in fig. 1.3a as a red solid line, has a maximum at non-vanishing tensile forces. In a simple conceptual picture, fig. 1.3b, an energy barrier separates the bound state from the unbound state in the energy landscape of the bond interaction. Whereas the effect of tensile force on a slip bond is a decreased

energy barrier and a higher dissociation rate, a larger energy barrier leads to longer lifetimes of catch bonds.

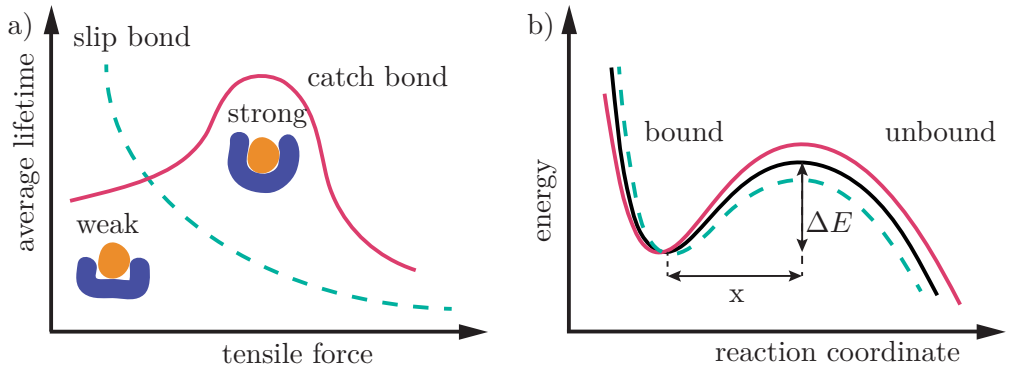

Figure 1.3: a) The average bond lifetime as a function of tensile force acting along a receptor-ligand catch bond exhibits a maximum at intermediate force as depicted by the red solid line. Force induces a transition form weak binding between the receptor (blue) and the ligand (orange) to a strong binding configuration. In contrast, the lifetime of a slip bond, shown as a dashed green line, monotonically decreases with increasing tensile force. b) The bond interaction potential exhibits an energy barrier of height ΔE separating the bound from the unbound state. The distance between the bound state and the transition state along the reaction coordinate is denoted by x. Compared to the case when no tensile force is applied (black solid line), for a slip bond (green dashed line) the barrier is decreased by applied force favoring bond dissociation, whereas for catch bonds (red solid line) the energy barrier increases with increasing force leading to prolonged lifetime.

The counterintuitive catch bond phenomenon has been experimentally observed for instance for some selectin-ligand interactions [91–93] that are relevant for adhesion and rolling of leukocyte on vascular surfaces [94, 95]. Further examples are catch bonds between actin and myosin [96], VWF and GPIbα [86], integrin and its ligand fibronectin [97] as well as for the cell adhesion protein cadherin [98, 99]. Interestingly, also ideal bonds [98] were found that exhibit an average bond lifetime being unaffected by tensile force. On the theoretical side, Sing and Alexander-Katz [76] considered the interplay of the shear-induced globule stretching and the adsorption transition and found that slip-resistant catch bonds are instrumental for observing shear-induced globule adsorption at a surface.

Several models for catch bonds were proposed but the detailed molecular mechanism is still not fully understood [89]. Whereas in the deformation model [100], schematically depicted in fig. 1.4a, force directly alters the structure of the receptor or the ligand, the allosteric model [101, 102], fig. 1.4b, assumes that upon applied force the bond changes to a conformation that binds stronger caused by pulling away an allosteric inhibitor distal to the binding site [9] . The sliding-rebinding model [86, 103], shown in fig. 1.4c, on the other hand, assumes that force changes the relative orientation of receptor and ligand leading to the formation of new contacts, e.g. additional hydrogen bonds [99], and

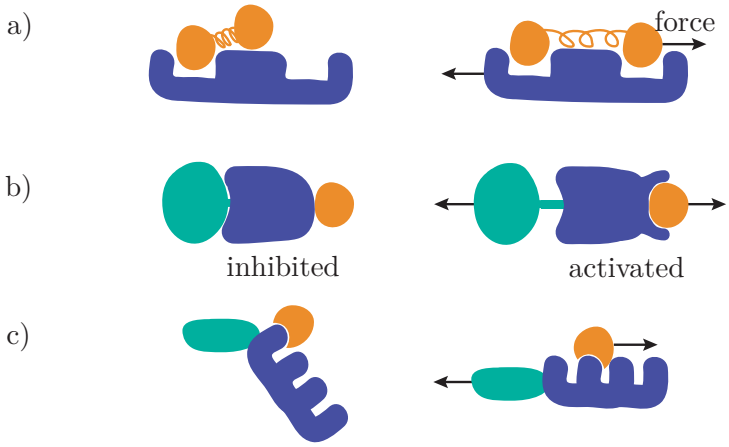

Figure 1.4: Conceptual models for catch bonds between receptor (blue) and ligand (orange). The left hand side depicts the bond complex in the absence of force, on the right hand side a tensile force is applied, indicated by black arrows. a) The deformation model assumes that the ligand can deform to better match with the binding domain when a force is applied. b) The allosteric model considers an inhibitor, shown in green, which is pulled away from the binding domain and thereby activates a conformation that binds stronger. c) In the sliding-rebinding model, applied force changes the relative orientation between the receptor and the ligand leading to a different dissociation pathway where new contacts can form.

thus to another dissociation pathway [9]. Theoretical models such as the two-pathway model [104, 105] involve either two distinct dissociation pathways from a bound state in the free energy landscape, or the existence of a second bound state which is stabilized by force [92, 106]. Another explanation assumes the dissociation in a multidimensional energy landscape where the reaction coordinate does not coincide with the direction of pulling [107, 108]. Each of the models are able to describe some of the experiments but there is no universal agreement and only limited capability to determine the underlying structural mechanism of catch bonds [89].

1.4 Outline of this work

In the present dissertation we study flow-induced features of multimeric proteins in general in order to contribute to the understanding of the physiological function of VWF in particular. The aim is to devise models, as simple as possible, which capture the essential physical properties of the real biological system, as observed in experiments. We are optimistic that the combination of theoretical concepts from polymer physics and numerical simulations can provide important insights into details of microscopic mechanisms that might be difficult to acquire from experiments. The main part of this thesis focuses on the initial adhesion process of VWF prior to platelet adsorption, but also the cleavage process of VWF is considered. We investigate a coarse-grained

homopolymer model and analyze hydrodynamic simulations based on the Langevin equation supplemented by hydrodynamic interactions.

In Chapter 2, we construct potential-based binding models on homogeneous and inhomogenous surfaces and investigate the dynamics and adsorption behavior of a collapsed homopolymer in shear flow. The goal is to understand the competition between shear-induced globule unfolding, surface-attraction induced adsorption, hydrodynamic repulsive lift force, and friction effects due to surface inhomogeneity. The present thesis investigates the interplay of all these aspects, which have been examined in past only separately. We map out detailed adsorption state diagrams as a function of the characteristic parameters such as shear rate, cohesive strength, and adhesive strength. Various dynamical states such as rolling and slipping of globular and coil-like configurations with either isotropic or prolate shape are characterized.

In Chapter 3, we study the VWF adsorption behavior with stochastic two-state surface-monomer bonds, a model that for particular parameter values was previously shown to lead to the counterintuitive phenomenon of shear-induced adsorption [76]. It allows to include the transition from slip to catch bond behavior in a heuristic manner. We present adsorption state diagrams as a function of shear rate, the surface-monomer bond dissociation and association rates and an effective catch bond parameter that describes the continuous change from slip to catch bond behavior. The stochastic two-state surface-monomer bond model is compared with a binding scenario based on conservative surface-monomer potentials, similar to that used in Chapter 2, in order to estimate the conservative potential parameters necessary to observe shear-induced surface adsorption phenomena.

Apart from the VWF adsorption behavior, another debated research topic concerns the relation between shear flow, VWF unfolding, opening of the VWF A2 domain, and the activity of the cleavage enzyme ADAMTS13. In Chapter 4, we consider the shear-dependent internal tension distribution along the contour of a collapsed polymer in an unbound fluid shear flow. From a polymer physics point of view, we substantiate the instability mechanism that leads to shear-induced globule unfolding based on the existence of polymeric protrusions. With a theoretical approach using scaling predictions and an quasi-equilibrium theory we determine average properties of the protrusions formed at the surface of a globule in shear. On the biological side, we establish the connection between the shear-induced internal tension along the coarse-grained polymer model of VWF and shear-dependent proteolysis of VWF by its specific cleavage enzyme ADAMTS13. We formulate a simple stochastic model for the force-dependent VWF A2 domain opening and exposure of the cleavage site. Using simulation results of the tension distribution we explain experiments from Dr. Svenja Lippok and Prof. Dr. Joachim Rädler (LMU Munich) on the ADAMTS13-mediated cleavage of full-length VWF in blood plasma.

Chapter 5 briefly summarizes all results of this thesis and possible future work is discussed.

Chapter 2

Shear-induced dynamics of polymeric globules at adsorbing homogeneous and inhomogeneous surfaces

2.1 Introduction

The behavior of polymers near surfaces is not only of fundamental and technological relevance, but also plays an important role in many biological processes [74]. As most technological and biological applications involve dissipation, there is general interest in understanding non-equilibrium aspects such as the adsorption of macromolecules in shear flow [9, 95, 109]. The present study is motivated by recent investigations [31] on the von Willebrand factor, a blood protein involved in hemostasis [27]. Experimental findings suggest the unfolding and activation of the von Willebrand factor at elevated shear rates as they are found in smaller blood vessels or at constriction sites [31] and subsequent binding to the vessel wall, which initiates the coagulation process [27, 110]. This represents an example of a biological regulation mechanism that presumably involves protein unfolding by a purely physical mechanism and therefore is of particular interest for polymer theory.

Many theoretical studies focused on the equilibrium adsorption of stiff and flexible polymer chains [64, 73, 74]; also the scenario of surface-grafted chains was considered in detail [69, 111]. When considering non-equilibrium effects, e.g. by inclusion of simple shear-flow [66, 67, 75], it has been shown that hydrodynamic interactions and the presence of a no-slip boundary is crucial and therefore has to be taken into account [68, 84, 112, 113].

In contrast to the adsorption of polymers in good solvent conditions, only very few works focused on the non-equilibrium adsorption of collapsed polymers. In a pioneering study, Sing and Alexander-Katz considered the interplay of the shear-induced globule stretching and the adsorption transition in detail [76]. They found that catch bonds are instrumental for observing shear-induced globule adsorption at the surface. This raises the interesting question what the minimal ingredients are in order to observe the counterintuitive phenomenon of shear-induced adhesion of a polymeric globule on a surface.

In the present work, we approach this problem by studying the dynamical states of a single globular polymer in shear flow at an adsorbing surface that is modeled on different levels of resolution. Using Brownian dynamics simulations including hydrodynamic interactions, we map out detailed dynamic adsorption state diagrams for three different kinds of surface models: i) a homogeneous adsorbing surface, ii) a homogeneous surface with a stagnant boundary layer within which the monomer mobility is reduced, and iii) a laterally inhomogeneous surface consisting of discrete binding sites with varying potential range. In particular, we consider the dynamics of the adsorbed globule and distinguish rolling states from slipping deformed states. Our study can thus be viewed as an extension of previous works on the rolling characteristics of a non-deformable sphere on a surface with discrete binding sites [109]. We obtain new dynamic states where the shear forces deform the adsorbed polymer into a prolate shape; this occurs both for coil-like conformations at low cohesion as well as for globular conformation at high cohesion. As a result, we find rich dynamic state diagrams as a function of shear rate and varying adhesive and cohesive strength, featuring various rolling and slipping states of globular and coil-like configurations with either isotropic or prolate shape. With the advent of advanced microscopy techniques such shape changes can be conveniently observed experimentally [31, 49]. In addition, we find different cyclic transformations depending on whether the globule is adsorbed or desorbed, indicative of fundamentally different surface-induced dissipative processes.

In the presence of hydrodynamic interactions we only observe shear-induced desorption of the polymeric globule from the surface; however, in the absence of hydrodynamic interactions, in which case shear-induced lift forces are absent, and for a hydrodynamically stagnant boundary layer, shear-induced adsorption is obtained. All our simulations are based on a potential-based Hamiltonian, meaning that the surface-polymer bonds correspond to slip bonds. One conclusion from our work is that a necessary condition for shear-induced adsorption are hydrodynamic screening effects as well as catch bond behavior between polymeric units and the surface, as was convincingly demonstrated by Sing and Alexander-Katz [76].

2.2 Simulation details

2.2.1 Low Reynolds number hydrodynamics at planar no-slip boundary

Particles in a suspension hydrodynamically interact through the continuous fluid in which they are immersed, i.e., the motion of one particle influences the fluid flow around another. The most general description of the dynamics in a viscous fluid is given by the Navier-Stokes equation [114]. When inertial forces are small compared to viscous forces, as it is the case for biological systems on the micro- and nanometerscale considered in this thesis, the linearized Stokes equation is applicable [115], given by

$$\nabla p(\mathbf{r}) - \eta \nabla^2 \mathbf{v}(\mathbf{r}) = \mathbf{f}(\mathbf{r}), \tag{2.1}$$

with the condition of an incompressible fluid

$$\nabla \cdot \mathbf{v}(\mathbf{r}) = 0. \tag{2.2}$$

The pressure p is related to the velocity field $\mathbf{v}$ and any external force density $\mathbf{f}(\mathbf{r})$. In other words, we deal with systems in the limit of low Reynolds number $Re = \rho l v/\eta$ [116], which is defined as the ratio of inertial and viscous contribution of an object of size l moving with velocity v in a fluid of density ρ and viscosity η.

2.2.1.1 An unbound fluid

We consider a point force $\mathbf{f}_s(\mathbf{r}) = \mathbf{f}_s\delta(\mathbf{r}-\mathbf{r}')$ with a magnitude f_s located at $\mathbf{r}'$, a so-called Stokeslet. The solution of the Stokes equation (2.1) is then obtained by the hydrodynamic Green's function $\boldsymbol{\mu}(\mathbf{r},\mathbf{r}')$ and the corresponding velocity field is $\mathbf{v}(\mathbf{r}) = \boldsymbol{\mu}(\mathbf{r},\mathbf{r}')\cdot\mathbf{f}_s$. In an unbound fluid and under the assumption of a vanishing flow field at infinity, the Green's function for a point force is commonly referred to as Oseen tensor,

$$\boldsymbol{\mu}^{\mathrm{O}}(\mathbf{r},\mathbf{r}') = \boldsymbol{\mu}^{\mathrm{O}}(\mathbf{r}-\mathbf{r}') = \frac{1}{8\pi\eta\,|\mathbf{r}-\mathbf{r}'|}\left(\mathbf{1} + \frac{(\mathbf{r}-\mathbf{r}')\otimes(\mathbf{r}-\mathbf{r}')}{|\mathbf{r}-\mathbf{r}'|^2}\right), \tag{2.3}$$

which can be obtain for instance by Fourier transform on eqs. (2.2),(2.1) [3, 115]. Notice that hydrodynamic interactions are long range as they decay with the inverse distance. Due to the linearity of the Stokes equation, superposition can be used to obtain the solution for a general force density, e.g. a number of N particles at $\mathbf{r}_j$. The velocity for particle i is then given by $\mathbf{v}_i(\mathbf{r}_i) = \sum_j \boldsymbol{\mu}_{ij}(\mathbf{r}_i,\mathbf{r}_j)\cdot\mathbf{f}_j$, with the mobility matrix $\boldsymbol{\mu}_{ij} = \boldsymbol{\mu}_{ij}(\mathbf{r}_i,\mathbf{r}_j)$.

The interaction between particles having a finite size can be described by the Oseen tensor only for large separations. For small separations, as it is the case for monomers assembled to a polymer, the particle size is approximately taken into account via a multipole expansion [117] to second order in terms of the particle radius a leading to the mobility matrix

$$\boldsymbol{\mu}^{\mathrm{RP}}(\mathbf{r}_i,\mathbf{r}_j) = \left(1 + \frac{a^2}{6}\nabla^2_{\mathbf{r}_i} + \frac{a^2}{6}\nabla^2_{\mathbf{r}_j}\right)\boldsymbol{\mu}^{\mathrm{O}}(\mathbf{r}_i,\mathbf{r}_j), \tag{2.4}$$

which is referred to as Rotne-Prager tensor [118],

$$\boldsymbol{\mu}^{\mathrm{RP}}(\mathbf{r}_i,\mathbf{r}_j) = \boldsymbol{\mu}^{\mathrm{RP}}(\mathbf{r}) = \mu_0 \begin{cases} \frac{3a}{4r}\left(\left(1+\frac{2a^2}{3r^2}\right)\mathbf{1} + \left(1-\frac{2a^2}{r^2}\right)\frac{\mathbf{r}\otimes\mathbf{r}}{r^2}\right) & r \geq 2a \\ \left(1-\frac{9r}{32a}\right)\mathbf{1} + \frac{3r}{32a}\frac{\mathbf{r}\otimes\mathbf{r}}{r^2} & r < 2a, \end{cases} \tag{2.5}$$

where $\mathbf{r} = \mathbf{r}_i - \mathbf{r}_j$ and $r = |\mathbf{r}|$. Although particle overlap is mostly prevented by the repulsive excluded volume interactions, the Yamakawa tensor [119] is included in eq. (2.5) for $r < 2a$ so that the mobility matrix is always positive definite. The self-mobility of a particle is given by the bare Stokes mobility of a sphere $\mu_0 = 1/6\pi\eta a$; the full mobility matrix for particles in an unbound fluid reads thus

$$\boldsymbol{\mu}_{ij} = \delta_{ij}\mu_0\mathbf{1} + (1-\delta_{ij})\boldsymbol{\mu}^{\mathrm{RP}}(\mathbf{r}_i,\mathbf{r}_j) \tag{2.6}$$

2.2.1.2 No-slip boundary at a plane surface

Interfaces alter the hydrodynamics of a fluid and thereby the motion of close objects. The flow field created by a point particle close to a plane no-slip boundary at $z = 0$ can be described by the Blake tensor [120] that is constructed using a method of images,

$$\boldsymbol{\mu}^{\mathrm{B}}(\mathbf{r}_i, \mathbf{r}_j) = \boldsymbol{\mu}^{\mathrm{O}}(\mathbf{r}) - \boldsymbol{\mu}^{\mathrm{O}}(\bar{\mathbf{r}}) + \boldsymbol{\mu}^{\mathrm{D}}(\bar{\mathbf{r}}) - \boldsymbol{\mu}^{\mathrm{SD}}(\bar{\mathbf{r}}). \tag{2.7}$$

It contains the Oseen contributions, eq. (2.3), of the original Stokeslet with the distance $\mathbf{r} = \mathbf{r}_i - \mathbf{r}_j$ and the image Stokeslet located at $\bar{\mathbf{r}}_j = (x_j, y_j, -z_j)$, where the distance is denoted by $\bar{\mathbf{r}} = \mathbf{r}_i - \bar{\mathbf{r}}_j$. In order to satisfy the no-slip condition at the planar surface, additional so-called image doublets are required: the Stokes doublet,

$$\mu^{\mathrm{D}}_{\alpha\beta}(\bar{\mathbf{r}}) = \mu_0 \frac{3}{2} z_j^2 \left(1 - 2\delta_{\beta z}\right) \left(\frac{\delta_{\alpha\beta}}{\bar{r}^3} - \frac{3\bar{r}_\alpha \bar{r}_\beta}{\bar{r}^5} \right), \tag{2.8}$$

with α, β being cartesian coordinates, and a Source doublet,

$$\mu^{\mathrm{SD}}_{\alpha\beta}(\bar{\mathbf{r}}) = \mu_0 \frac{3}{2} z_j \left(1 - 2\delta_{\beta z}\right) \left(\frac{\delta_{\alpha\beta}\bar{r}_z}{\bar{r}^3} - \frac{\delta_{\alpha z}\bar{r}_\beta}{\bar{r}^3} + \frac{\delta_{\beta z}\bar{r}_\alpha}{\bar{r}^3} - \frac{3\bar{r}_\alpha \bar{r}_\beta \bar{r}_z}{\bar{r}^5} \right). \tag{2.9}$$

Again, the finite particle size is accounted for by a multipole expansion of the Blake tensor, eq. (2.7), leading to the Rotne-Prager-Blake tensor

$$\begin{aligned} \boldsymbol{\mu}^{\mathrm{RPB}}(\mathbf{r}_i, \mathbf{r}_j) &= \left(1 + \frac{a^2}{6}\nabla^2_{\mathbf{r}_i} + \frac{a^2}{6}\nabla^2_{\mathbf{r}_j}\right) \boldsymbol{\mu}^{\mathrm{B}}(\mathbf{r}_i, \mathbf{r}_j) && (2.10) \\ &= \boldsymbol{\mu}^{\mathrm{RP}}(\mathbf{r}) - \boldsymbol{\mu}^{\mathrm{RP}}(\bar{\mathbf{r}}) + \boldsymbol{\Delta\mu}(\bar{\mathbf{r}}) && (2.11) \end{aligned}$$

Explicit entries for the contributions from the Stokes doublet and the Source doublet,

$$\boldsymbol{\Delta\mu}(\bar{\mathbf{r}}) = \left(1 + \frac{a^2}{6}\nabla^2_{\mathbf{r}_i} + \frac{a^2}{6}\nabla^2_{\mathbf{r}_j}\right) \left(\boldsymbol{\mu}^{\mathrm{D}}(\bar{\mathbf{r}}) - \boldsymbol{\mu}^{\mathrm{SD}}(\bar{\mathbf{r}})\right), \tag{2.12}$$

are given by [63]

$$\begin{aligned} \Delta\mu_{\alpha\alpha} &= \frac{3\mu_0}{2} \left(\frac{z_i z_j}{\bar{r}^3} \left(3\frac{\bar{r}_\alpha^2}{\bar{r}^2} - 1 \right) + \frac{a^2 \bar{r}_z^2}{\bar{r}^5} \left(1 - 5\frac{\bar{r}_\alpha^2}{\bar{r}^2} \right) \right) && (2.13) \\ \Delta\mu_{zz} &= -\frac{3\mu_0}{2} \left(\frac{z_i z_j}{\bar{r}^3} \left(3\frac{\bar{r}_z^2}{\bar{r}^2} - 1 \right) + \frac{a^2 \bar{r}_z^2}{\bar{r}^5} \left(3 - 5\frac{\bar{r}_z^2}{\bar{r}^2} \right) \right) && (2.14) \\ \Delta\mu_{\alpha\beta} &= \frac{3\mu_0}{2} \left(3\frac{z_i z_j \bar{r}_\alpha \bar{r}_\beta}{\bar{r}^5} - 5\frac{a^2 \bar{r}_\alpha \bar{r}_\beta \bar{r}_z^2}{\bar{r}^7} \right) && (2.15) \\ \Delta\mu_{\alpha z} &= -\frac{3\mu_0}{2} \left(\frac{z_j \bar{r}_\alpha}{\bar{r}^3} \left(3\frac{z_i \bar{r}_z}{\bar{r}^2} - 1 \right) + \frac{a^2 \bar{r}_\alpha \bar{r}_z}{\bar{r}^5} \left(2 - 5\frac{\bar{r}_z^2}{\bar{r}^2} \right) \right) && (2.16) \\ \Delta\mu_{z\alpha} &= \frac{3\mu_0}{2} \left(\frac{z_j \bar{r}_\alpha}{\bar{r}^3} \left(3\frac{z_i \bar{r}_z}{\bar{r}^2} + 1 \right) + 5\frac{a^2 \bar{r}_\alpha \bar{r}_z^3}{\bar{r}^7} \right), && (2.17) \end{aligned}$$

where only here $\alpha \neq \beta \neq z$.

The no-slip boundary at the surface also changes the self-mobilities of the particles. Since the fluid velocity vanishes on the plane $z = 0$ the mobility must decrease as a function of the distance z_i to the surface

$$\boldsymbol{\mu}_{\mathrm{self}}^{\mathrm{RPB}}(z_i)_{\alpha\beta} = \delta_{\alpha\beta}((\delta_{\alpha x} + \delta_{\alpha y})\mu_{\parallel}^{\mathrm{RPB}}(z_i) + \delta_{\alpha z}\mu_{\perp}^{\mathrm{RPB}}(z_i)). \tag{2.18}$$

The self-mobility parallel to the surface

$$\mu_{\parallel}^{\mathrm{RPB}}(z_i) = \mu_0 \left(1 - \frac{9a}{16z} + \frac{1}{8}\frac{a^3}{z_i^3}\right) + \mathcal{O}(a^4) \tag{2.19}$$

and the perpendicular component

$$\mu_{\parallel}^{\mathrm{RPB}}(z_i) = \mu_0 \left(1 - \frac{9a}{8z} + \frac{1}{2}\frac{a^3}{z_i^3}\right) + \mathcal{O}(a^4) \tag{2.20}$$

are obtained [63, 121] by taking the limit $\mathbf{r}_i \to \mathbf{r}_j$ of the Rotne-Prager-Blake tensor eq. (2.11). The full mobility matrix reads

$$\boldsymbol{\mu}_{ij} = \delta_{ij}\boldsymbol{\mu}_{\mathrm{self}}^{\mathrm{RPB}}(z_i) + (1 - \delta_{ij})\boldsymbol{\mu}^{\mathrm{RPB}}(\mathbf{r}_i, \mathbf{r}_j) \tag{2.21}$$

2.2.2 Brownian dynamics simulation

We consider an ensemble of N spherical particles with the radius a immersed in a viscous fluid undergoing Brownian motion. The overdamped Langevin equation describes the stochastic time evolution of the particle position for low Reynolds number

$$\frac{d\mathbf{r}_i(t)}{dt} = \boldsymbol{v}(\mathbf{r}_i) - \sum_j^N \boldsymbol{\mu}_{ij} \cdot \nabla_{\mathbf{r}_j} U(\mathbf{r}_1, \ldots, \mathbf{r}_N) + \sum_j^N \nabla_{\mathbf{r}_j}\boldsymbol{\mu}_{ij} + \boldsymbol{\xi}_i(t). \tag{2.22}$$

The first term on the right hand side represents the undisturbed solvent flow field that might be shear or elongational flow. The second term couples the forces to the velocity via the mobility tensor. It accounts for the direct forces on particle i itself as well as the hydrodynamic flow field created by forces acting on all other particle $j \neq i$. In general, the mobility can depend on the position of the particle, as it is the case close to no-slip boundaries. The third term in eq. (2.22) is introduced in order to compensate the flux caused by the position dependent random force [3]. In this way the Langevin equation is equivalent to the Smoluchowski equation describing the time evolution of the probability density of the particle position. Note that for the case of an unbound fluid, the spatial derivate of the Rotne-Prager-tensor, eq. (2.5), vanishes. In the presence of a plane surface with no-slip boundary condition, the mobility matrix eq. (2.21) has to be considered; the only non-vanishing derivative is the perpendicular self-mobility of the Rotne-Prager-Blake tensor, $\sum_j^N \nabla_{\mathbf{r}_j}\boldsymbol{\mu}_{ij} = \mathrm{kT}\left.\frac{d\mu_{\perp}^{\mathrm{RPB}}(z)}{dz}\right|_{z=z_i}$.

Thermal fluctuations are incorporated in the last term of eq. (2.22) via stochastic velocities that have vanishing mean, $\langle \boldsymbol{\xi}_i(t) \rangle = 0$, and satisfy the fluctuation dissipation theorem,

$$\left\langle \boldsymbol{\xi}_i(t) \boldsymbol{\xi}_j(t') \right\rangle = 2\mathrm{kT} \boldsymbol{\mu}_{ij} \delta(t - t'). \tag{2.23}$$

Thereby the correct equilibrium distribution is reproduced in the stationary state which is given by the Boltzmann distribution.

We perform Brownian dynamics simulations and incorporate hydrodynamic interactions via the Rotne-Prager-Blake mobility tensor, eq. (2.21), which accounts for the no-slip surface boundary condition and the finite particle size via a multipole expansion to second order in terms of the particle radius [63, 120]. This method is practical for small particle numbers and large system volumes, as we have in our study, and thus preferred over alternative Lattice-Boltzmann methods [122] or multi-particle collision dynamics [123]. Using a simple Euler scheme for numerical integration, a time discretized version of the Langevin equation (2.22) describing the position of particle i after a timestep Δt is given by

$$\mathbf{r}_i(t + \Delta t) = \mathbf{r}_i(t) + \left(\boldsymbol{\mu}_{ii} \dot{\gamma} z_i \hat{\mathbf{x}} - \sum_j \boldsymbol{\mu}_{ij} \cdot \nabla_{\mathbf{r}_j} U(t) + \sum_j \nabla_{\mathbf{r}_j} \boldsymbol{\mu}_{ij} \right) \Delta t + \boldsymbol{\xi}_i(\Delta t). \tag{2.24}$$

In the following, all quantities used are made dimensionless by rescaling lengths $r = \tilde{r}/a$ by the monomer radius a, energies $U = \tilde{U}/\mathrm{kT}$ by thermal energy and times $t = \tilde{t}/\tau$ by the characteristic monomer diffusion time $\tau = a^2/(\mu_0 \mathrm{kT})$, where μ_0 is the Stokes mobility. Note that from now on quantities with a physical unit are decoreded with a tilde. We introduce in eq. (2.24) a linear shear flow for the solvent flow field $\boldsymbol{v}(\mathbf{r}_i(t)) = \boldsymbol{\mu}_{ii} \dot{\gamma} z_i \hat{\mathbf{x}}$ with shear rate $\dot{\gamma} = \tilde{\dot{\gamma}} \tau$, where $\hat{\mathbf{x}}$ is the unit vector in x-direction and $\boldsymbol{\mu}_{ii} = \tilde{\boldsymbol{\mu}}_{ii}/\mu_0$ the self-mobility. Note that we do not consider elongational flow effects, which were shown to very efficiently promote chain unfolding [54, 124]. In the simulation, the stochastic contribution $\boldsymbol{\xi}_i(\Delta t) = \sqrt{2\Delta t} \sum_k \boldsymbol{L}_{ik} \boldsymbol{n}_i$ is calculated by means of a Cholesky decomposition of the mobility matrix eq. (2.21) with entries $\boldsymbol{\mu}_{ij} = \tilde{\boldsymbol{\mu}}_{ij}/\mu_0 = \sum_k \mathbf{L}_{ik} \mathbf{L}_{jk}^T$ using Gaussian random vectors $\boldsymbol{n}_i$ with vanishing mean and correlation $\langle \boldsymbol{n}_i(t) \boldsymbol{n}_j(t') \rangle = \delta_{ij} \delta(t - t') \mathbf{1}$.

The simulation time step is typically chosen as $\Delta t = 10^{-4}$ and for computational speed we update the mobility matrix $\boldsymbol{\mu}_{ij}$ only every tenth step, which does not alter the results.

2.2.3 Model

The polymer consists of $N = 50$ beads, which interact via Lennard-Jones potentials of depth $\varepsilon = \tilde{\varepsilon}/\mathrm{kT}$ and are connected in a linear chain by stiff harmonic bonds with a rescaled spring constant $\kappa = \tilde{\kappa} a^2/\mathrm{kT} = 200$,

$$U_{\mathrm{pol}} = \varepsilon \sum_{i<j} \left((2/r_{ij})^{12} - 2 (2/r_{ij})^6 \right) + \frac{\kappa}{2} \sum_i (r_{i,i+1} - 2)^2 . \tag{2.25}$$

The total potential energy $U = U_{\text{pol}} + U_{\text{hom/inh}} + U_{\text{rep}}$ includes in addition a surface term that accounts for adhesion, $U_{\text{hom/inh}}$, and a term U_{rep} that represents a purely repulsive wall.

The inhomogeneous surface (iii) is modeled by a square lattice of discrete binding sites with distance b, located at a height $z_W = 2$ above the no-slip boundary located at $z = 0$. The rescaled surface density of binding sites is thus $\rho_W = \tilde{\rho}_W a^2 = 1/b^2$. Summation over all pair interactions gives the surface potential as

$$U_{\text{inh}} = \sum_i \sum_k \varepsilon_W \left(\frac{\sigma_W^{12}}{(\sigma_W + r_{ik})^{12}} - \frac{2\sigma_W^6}{(\sigma_W + r_{ik})^6} \right), \tag{2.26}$$

where r_{ik} is the distance between monomer i and binding site k. We have shifted the potential by the range $\sigma_W = \tilde{\sigma}_W/a$ and therefore have a purely attractive potential with a depth of $\varepsilon_W = \tilde{\varepsilon}_W/\text{kT}$.

The homogeneous surface model (i) follows from eq. (2.26) in the limit of high binding site density $\rho_W > \sigma_W^{-2}$ by replacing the sum by an integral (Appendix A.1), the resulting homogeneous surface potential reads

$$U_{\text{hom}} = \sum_i \frac{\pi}{5} \varepsilon_W \rho_W \sigma_W^2 \left(\frac{(11|z_i - 2| + \sigma_W)\, \sigma_W^{10}}{11\,(\sigma_W + |z_i - 2|)^{11}} - \frac{(5|z_i - 2| + \sigma_W)\, \sigma_W^4}{(\sigma_W + |z_i - 2|)^5} \right). \tag{2.27}$$

To account for steric exclusion of the polymer from the surface and in particular to prevent crossing of the no-slip boundary located at $z = 0$, we use an additional repulsive potential

$$U_{\text{rep}} = \sum_i \begin{cases} 2\pi\sigma_R^2 \left(\frac{2}{5} \left(\frac{\sigma_R}{z_i} \right)^{10} - \left(\frac{\sigma_R}{z_i} \right)^4 + \frac{3}{5} \right) & z_i \le \sigma_R \\ 0 & z_i > \sigma_R \end{cases} \tag{2.28}$$

with a short range of $\sigma_R = 1.2$. Furthermore, we prevent escape of the polymer to infinity by a soft wall acting on the polymer center-of-mass located at a height $z = 15$.

Surface model (ii) employs a homogeneous surface potential and is characterized by a hydrodynamically stagnant boundary layer within which the monomer self-mobility is reduced. We thus replace the Rotne-Prager-Blake self-mobility profile $\boldsymbol{\mu}_{\text{self}}^{\text{RPB}}(z_i)$ by the heuristic expression

$$\mu_{\text{self}}(z_i) = (1 - \mu_s) \left[\tanh\left(10\,(z_i - 2.5)\right) + 1 \right]/2 + \mu_s, \tag{2.29}$$

which yields a rapid yet smooth transition from the bulk mobility $\mu_{\text{self}}(z_i \to \infty) = 1$ to a reduced surface mobility $\mu_s = \tilde{\mu}_s/\mu_0$ at around a distance $z = 2.5$. Equation 2.29 constitutes a simple heuristic model to investigate surface friction effects that might for example be due to discrete surface binding sites or hydrodynamic screening caused by surface corrugations or grafted polymers.

2.3 Results for homogeneous surface

2.3.1 Fixed shear rate, variable cohesive strength

The range of the homogeneous surface potential eq. (2.27) is set to $\sigma_W = 1.5$ and the density is fixed at $\rho_W = 0.25$. We first present the dynamic state diagram for varying cohesive strength ε and adhesive strength ε_W at a fixed shear rate $\dot{\gamma} = 1$ in fig. 2.1. All different dynamic states are illustrated by representative snapshots in fig. 2.1a. The black almost vertical line denotes the transition from the desorbed state for small adhesion ε_W (to the left) to different adsorbed states for large adhesion ε_W (to the right). Various heuristic definitions have been proposed for this transition, which for a finite-length polymer does not correspond to a phase transition in the strict thermodynamic sense. We here use for the adsorbed state the simple distance criterion $(z_{\mathrm{com}} - R_{gz}) < (z_W + \sigma_W)$, where $z_{\mathrm{com}} = N^{-1} \sum_i^N z_i$ is the polymer center-of-mass height, $R_{gz}^2 = N^{-1} \sum_i^N (z_i - z_{\mathrm{com}})^2$ is the z-component of the radius of gyration. Our criterion thus defines the polymer to be adsorbed when the polymer height z_{com} corrected by the radius R_{gz} is smaller than the sum of the potential range σ_W and the location of the potential origin z_W. In fig. 2.2a we plot the average $z_{\mathrm{com}} - z_W$ for different values of ε as a function of the adhesion ε_W, the transition according to our criterion is denoted by broken vertical lines. The time series of z_{com} for $\varepsilon = 1$ and $\varepsilon_W = 3.2$ in fig. 2.3a demonstrate that the polymer alternates between desorbed and adsorbed states, according to our distance criterion the adsorption occurs for $\varepsilon = 1$ around $\varepsilon_W = 3.8$.

In the absence of hydrodynamic boundaries, an isolated hard sphere in simple shear rotates with a frequency of $\omega = \dot{\gamma}/2$; we in fact verified (Appendix A.4) that our hydrodynamic simulation code reproduces this limiting result for large values of the cohesion ε. When a hard sphere approaches a surface with a hydrodynamic no-slip boundary condition, the rotational frequency is reduced due to lubrication effects but reaches a finite value upon contact [77]. For deformable objects such as polymers or vesicles, the rotation frequency is reduced additionally due to dissipative effects associated with periodic stretching and relaxation cycles [49, 125]. Note that on a homogeneous surface, we always find substantial slip of the globule on the surface since the monomer self-mobility decreases rather smoothly as the surface is approached (this is different on an inhomogeneous surface where additional friction effects are produced by lateral surface-monomer interactions, as we will discuss in Section 2.5). The rotation in the rolling globule state (RG) is illustrated in fig. 2.1b by contour lines of the rescaled angular velocity $\omega/\dot{\gamma} = L_y/(J_y\dot{\gamma})$, where L_y and J_y are the polymer angular momentum and moment of inertia with respect to the y-axis, respectively (Appendix A.4). We see that for large cohesion ε and small adhesion ε_W rotation is pronounced. In fig. 2.1b we also show a contour plot of the rolling parameter defined by the ratio $\omega R_{gz}/V$, where V denotes the center-of-mass velocity. For a compact object that rolls without slip over a surface the rolling parameter is of order unity One sees that as ε_W increases both $\omega/\dot{\gamma}$ and $\omega R_{gz}/V$ decrease in a very similar way, leading to the conclusion that rolling and

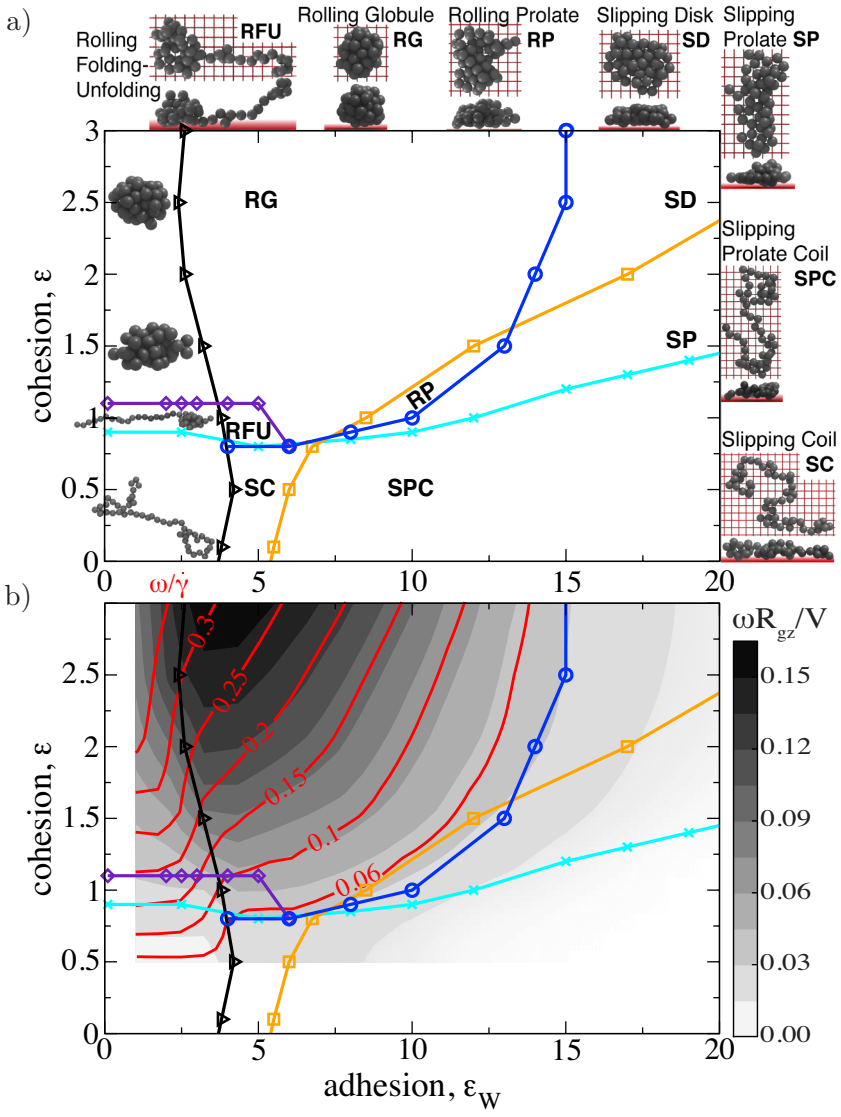

Figure 2.1: Dynamical state diagram for a polymer with varying cohesive strength ε and adhesive strength ε_W at fixed shear rate $\dot{\gamma} = 1$. The black line denotes the adsorption transition as determined by a distance criterion. The dark blue line marks the transition from rolling to slipping motion, determined by a value of the rescaled angular velocity of $\omega/\dot{\gamma} = 0.05$ and for high ε separates the rolling globule state (RG) from the slipping disk state (SD). In (b) the distribution of $\omega/\dot{\gamma}$ is illustrated by red contour lines, while the rolling parameter $\omega R_{gz}/V$ is given in shades of gray. The orange line denotes the transition into a prolate arrangement perpendicular to the flow direction and separates the slipping disk (SD) from the slipping prolate state (SP), the rolling globule (RG) from the rolling prolate (RP), and the slipping coil (SC) from the slipping prolate coil state (SPC). The collapse transition between the coil state at low ε and the globular state at high ε is denoted by the cyan line. The purple line is defined by a maximum in the chain extension fluctuations and separates the rolling globule (RG) from the rolling folding-unfolding state (RFU). Snapshots in (a) show representative conformations for each state.

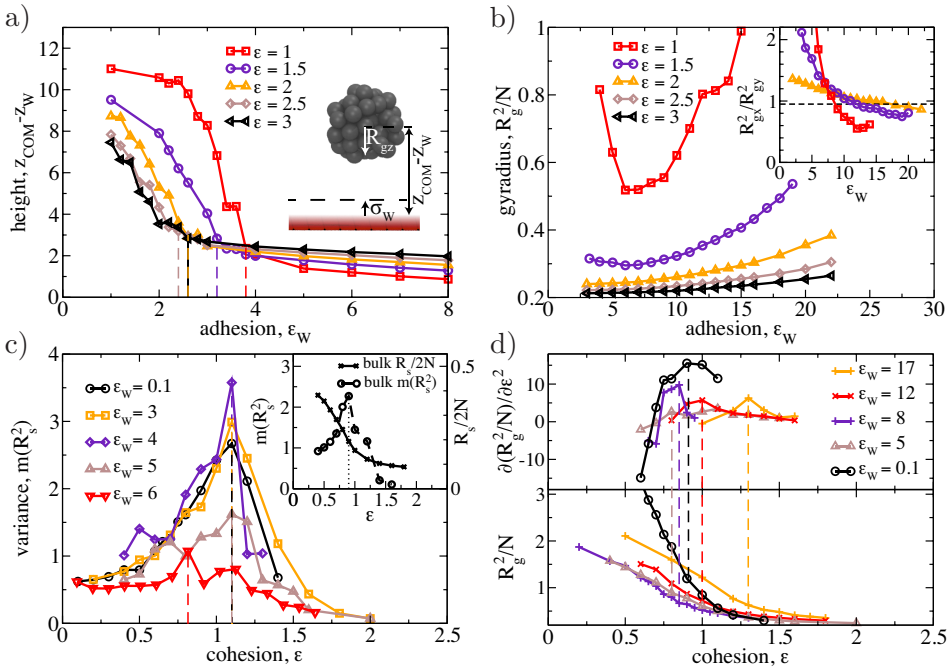

Figure 2.2: a) Average height of the polymer center-of-mass $z_{\rm com}$ relative to the surface location z_W for varying adhesive strength ε_W and different fixed values of the cohesive strength ε. The adsorption transition defined by $(z_{\rm com} - z_W) = (R_{gz} + \sigma_W)$ is indicated by vertical dashed lines, where R_{gz} is the z-component of the radius of gyration and σ_W is the surface interaction range, see snapshot. b) Squared radius of gyration R_g^2/N as a function of ε_W. The inset shows the ratio of the squared components R_{gx}^2 and R_{gy}^2 parallel and perpendicular to the flow direction. The horizontal dashed line indicates the prolate-isotropic transition defined by $R_{gx}^2/R_{gy}^2 = 0.95$. c) Squared radius of gyration R_g^2/N and its curvature $\partial^2(R_g^2/N)/\partial^2\varepsilon$ as a function of ε. The maxima of the curvature define the collapse-transition and are denoted by vertical dashed lines. d) Variance of the squared extension in flow direction $m(R_s^2)$ for varying ε. The peaks define the stretch-transition (dashed vertical lines). The same quantity for a polymer in bulk is shown in the inset.

rotation in the adsorbed globular state is strictly coupled. We define the transition from rolling to slipping for $\omega/\dot\gamma = 0.05$, which corresponds to ten percent of the bulk value and is denoted by a dark blue line.

At high cohesion ε the rolling globule state (RG) yields to the slipping disk state (SD) as the adhesion ε_W increases, where the polymer is still very compact but flattened out on the surface (see snapshot). The discoid shape in the SD state prevents rolling and rotation. As the cohesion ε is reduced at relatively high adhesion ε_W, the shear forces deform the polymer and give rise to a slipping prolate state (SP) at high ε_W and, in a very small window for intermediate values of ε_W, to a rolling prolate state (RP). We define the transition from the symmetric to prolate shapes using the radius of gyration components parallel and perpendicular to the shear flow. If the ratio R_{gx}^2/R_{gy}^2 is smaller

than 0.95 we denote the structure as prolate. In fig. 2.1 this structural transition is denoted by an orange line and illustrated in the inset of fig. 2.2b, where we plot R_{gx}^2/R_{gy}^2 as a function of ε_W for a few different values of ε.

In the lower left corner of the rolling region in fig. 2.1 we find a rolling folding-unfolding (RFU) state, which is characterized by cyclic stretching-refolding events combined with a rolling motion. The purple line is defined by the maximum of the variance of the squared extension R_s^2 in flow direction, as illustrated in fig. 2.2d, and is generally referred to as a shear-induced unfolding transition [58, 61]. The extension R_s is defined as the maximal distance in flow direction between any two beads from which the normalized variance follows as

$$m(R_s^2) = \frac{\langle R_s^4 \rangle - \langle R_s^2 \rangle^2}{\langle R_s^2 \rangle^2}. \tag{2.30}$$

The unfolding transition between the RG and RFU states continuously extends into the desorbed region, which is related to the fact that we limit the polymer separation from the surface by the finite height of the simulation box. Note that in the absence of a bounding wall, i.e. in bulk, this transition occurs at a somewhat lower cohesion of $\varepsilon = 0.9$ as illustrated in the inset of fig. 2.2d. This surface-induced unfolding enhancement has been demonstrated previously [62].

In general, we discriminate coil from globule conformations by the magnitude of the squared radius of gyration R_g^2, the collapse transition is denoted by the cyan line in fig. 2.1 and defined by the maximum curvature of R_g^2, as illustrated in fig. 2.2c. Note that we make a fine distinction between the collapse transition, associated with the radius of gyration, and the shear-induced unfolding transition, linked to the chain extension in flow direction. It turns out that an adsorbed coil is always slipping, meaning that no or only very little solid-body rotation occurs. This becomes most transparent from the red iso-rotational-frequency contour lines in fig. 2.1b. The transition between isotropic and prolate conformations (orange line) extends into the coil state and separates the slipping isotropic coil state SC from the slipping prolate coil state SPC, in agreement with previous observations [51, 66]. In fig. 2.2b we plot R_g^2 for different values of ε as a function of ε_W. In the rolling globular (RG) state, i.e. for high values of ε, R_g^2 increases monotonically due to the globule deformation caused by the strongly attractive surface. The case $\varepsilon = 1$ is different since we cross the rolling folding-unfolding (RFU) region, see the state diagram fig. 2.1. Here the radius of gyration first decreases with growing adhesion ε_W since the attractive wall suppresses the periodic folding-unfolding cycles, for larger ε_W we see that R_g^2 increases again because the globule flattens out on the surface.

2.3.2 Cyclic transformations

We now analyze the non-equilibrium polymer dynamics in shear flow in more detail and in particular discuss the occurrence of cyclic processes. In fig. 2.3a we plot time series

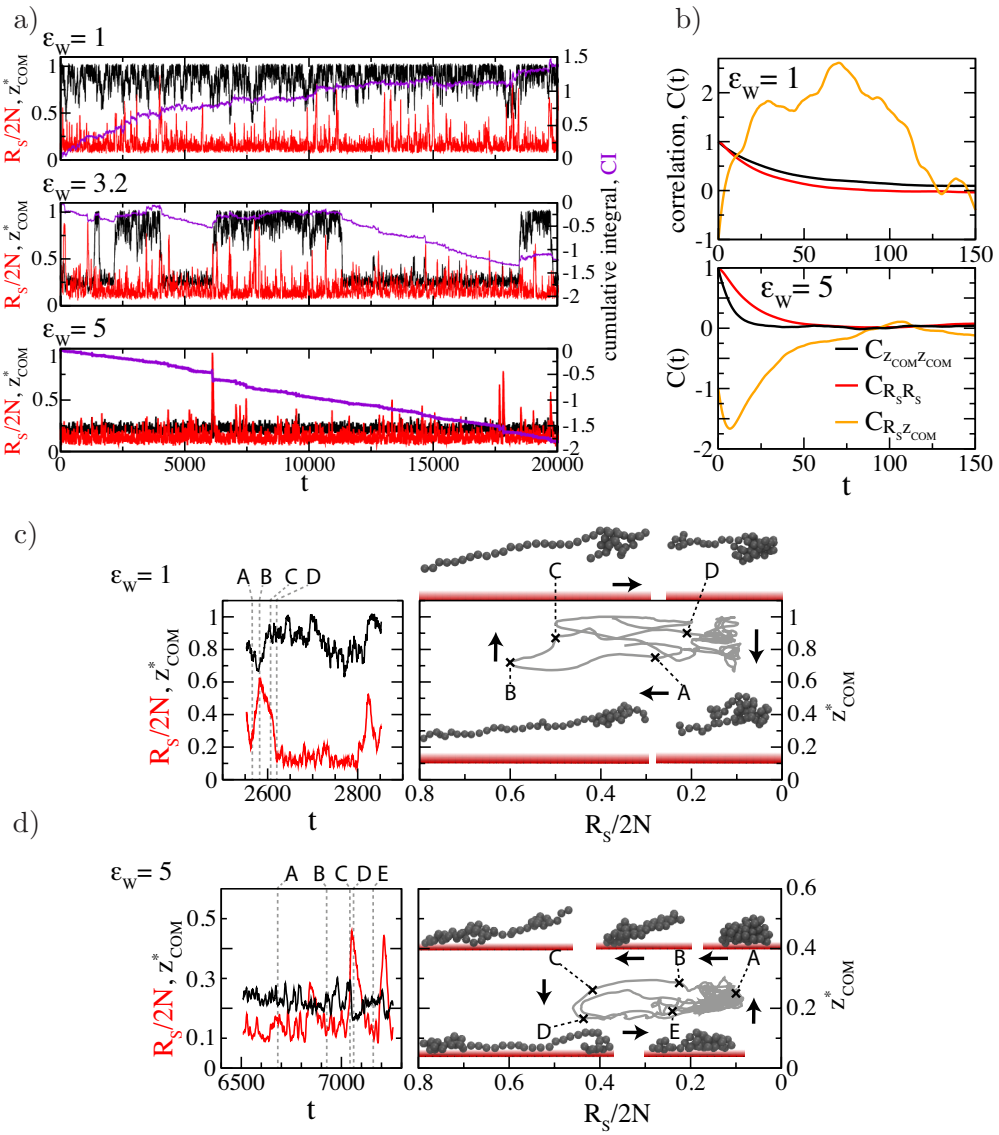

Figure 2.3: a) Time series of the rescaled extension $R_s/2N$ (red) and of the center-of-mass separation from the surface rescaled by the simulation box height $z^*_{\mathrm{com}} = z_{\mathrm{com}}/15$ (black) are compared for fixed cohesion $\varepsilon = 1$ and fixed shear rate $\dot{\gamma} = 1$ for different adhesive strength values. In the desorbed state for $\varepsilon_W = 1$ polymer stretching occurs, indicated by peaks in R_s, when the polymer is located close to the surface. The cumulative integral CI (purple) of R_s versus z^*_{com} increases over time. Close to the adsorption transition at $\varepsilon_W = 3.2$, the polymer is only transiently adsorbed on the surface and CI shows alternating behavior. For $\varepsilon_W = 5$ the polymer is firmly adsorbed, stretching events are rare and CI monotonically decreases over time. b) Autocorrelation and cross-correlation functions of extension and height are shown for $\varepsilon_W = 1$ and $\varepsilon_W = 5$. c) One typical cycle (gray line) of a desorbed polymer for $\varepsilon_W = 1$ is shown and illustrated with snapshots, corresponding to adjacent labels. The cycle is traversed clockwise, leading to a positive increase of the cumulative integral CI. d) When the polymer is adsorbed for $\varepsilon_W = 5$, the cycle is traversed counter-clockwise, hence CI decreases in time.

of the rescaled extension $R_s/2N$ (red) and the center-of-mass position $z^*_{\mathrm{com}} = z_{\mathrm{com}}/15$ (black) rescaled by the height of the simulation box; note that these rescaled variables are strictly bound by unity. In the same graph we also display the cumulative integral

$$\mathrm{CI}(t) = \int_0^t \frac{R_s(t')}{2N} dz^*_{\mathrm{com}}(t') \tag{2.31}$$

as a purple line. For the desorbed polymer with $\varepsilon_W = 1$, CI increases in time, for the adsorbed polymer with $\varepsilon_W = 5$, CI decreases, and for the intermediate situation $\varepsilon_W = 3.2$ we see an intermediate behavior where CI decreases over periods where the polymer is adsorbed (and z^*_{com} is small) and otherwise stays constant or slightly increases.

Intuitively speaking, CI measures the enclosed area of the trajectory of $R_s(t)/2N$ versus $z^*_{\mathrm{com}}(t)$ which is shown in fig. 2.3c,d for two different values of the adhesive strength ε_W. For the desorbed state with $\varepsilon_W = 1$ in fig. 2.3c, we see that an increasing CI means that the trajectory corresponds to predominantly clockwise cyclic transformations. The mechanism for this can be visualized by typical chain snapshots: When the polymer diffuses towards the surface in a rather compact state, i.e. small R_s, see snapshot (A), surface-induced stretching occurs because of the decreased rotational and translational polymer mobility at the surface, leading to state (B), as has been discussed before [62]. The stretched form gives rise to an increased hydrodynamic lift force away from the surface, and thus induces the transition to state (C). Away from the surface, the unfolding tendency is smaller, which leads to a refolding and thus to a transition from (C) to (D). In the adsorbed state for $\varepsilon_W = 5$ the cycle is traversed predominantly counter-clockwise, in fig. 2.3d we show a typical cycle. In (A) the adsorbed globule has a rather compact state. A partial unfolding is initiated (B-C) by a protrusion [58], leading to a polymer strand that is highly stretched by hydrodynamic drag forces and oriented parallel to the surface. Since the stretched chain shows reduced fluctuations in the perpendicular direction to the surface, it is more easily adsorbed leading to state (D) where the center-of-mass height is reduced compared to the globular state. This stretching-induced adsorption mechanism has been previously discussed in the absence of hydrodynamic interactions and is typically overwhelmed by hydrodynamic drag effects [68, 126], in the present situation it seems to be operative since the chain is inhomogeneous and consists of a stretched protrusion and a globular section that acts as an anchor. Once adsorbed, the shear forces are reduced and the polymer can refold into a globular state (E), this transformation is assisted by the rolling motion of the chain, and leads back to the starting configuration of a globule adsorbed at the surface, state (A). Close to the adsorption transition $\varepsilon_W = 3.2$ in fig. 2.3a, the polymer alternates between clockwise and counter-clockwise trajectories for the desorbed and the adsorbed state and thus the cumulative integral is closer to zero.

This picture can be substantiated by the correlation function of two variables $A(t)$ and $B(t)$ defined as

$$C_{AB}(\tau) = \left(\langle A(t)B(t+\tau)\rangle - \langle A\rangle \langle B\rangle\right) / \left(\sigma_A \sigma_B\right), \tag{2.32}$$

where $\sigma_{A,B}$ are the respective standard deviations. We show in fig. 2.3b auto and cross-correlations for R_s and z_{com} for the desorbed $\varepsilon_W = 1$ and the adsorbed $\varepsilon_W = 5$

states. While the autocorrelation functions $C_{R_sR_s}(\tau)$ and $C_{z_{\rm com}z_{\rm com}}(\tau)$ are positive and decay in a roughly exponential manner both in the adsorbed and desorbed states, the cross-correlation function $C_{R_sz_{\rm com}}(\tau)$ has a different sign in the two states and decays over a rescaled time of about 100, which is roughly the time span of the cycles shown in fig. 2.3c and d.

2.3.3 Fixed cohesive strength, variable shear rate

In fig. 2.4a we plot the dynamic state diagram on a homogeneous surface as a function of the adhesive strength ε_W and the shear rate $\dot\gamma$ for fixed cohesive strength $\varepsilon = 2$, in which case the polymer forms a well-defined globule for low shear flow. The desorption-adsorption transition, obtained from the mean separation of the polymer from the adsorbing surface as explained before, is marked by a black line. As a main observation we see that the higher the shear rate, the more adhesive strength is needed to adsorb the globule. A marked change in the slope of this transition is seen around $\varepsilon_W = 2.5$, i.e., where the adhesion is of comparable strength as the cohesion. For large adhesion, the critical shear rate scales roughly linear with the adhesive strength ε_W. This suggests that the hydrodynamic lift force that is responsible for the desorption at high shear scales linear in the shear rate $\dot\gamma$ and is caused by a stationary disk-like deformation of the globule shape. For small adhesion the critical shear rate rises much more steeply with adhesive strength $\dot\gamma \sim \varepsilon_W^6$; this regime is more intricate as the shear-induced lift force presumably depends via the adhesion-induced globule deformation also on the adhesive strength ε_W.

As before, we define the transition between rolling globule (RG) and slipping disk (SD) states by a critical value of the angular velocity of $\omega/\dot\gamma = 0.05$ denoted by the blue line. Increasing the adhesive strength ε_W flattens the globule and leads to the SD state. In the adhesion range $9 < \varepsilon_W < 16$ we see slip reentrance as the shear rate $\dot\gamma$ is increased: Only for intermediate values of $\dot\gamma$ does the shear induce rolling, for higher shear rates and close to the desorption transition the increased stretching in the flow direction inhibits rolling of the chain. The squared average extension R_s^2 in fig. 2.4b monotonically increases with shear rate, the stretch-transition defined by the peak of the variance $m(R_s^2)$, denoted by the purple line in fig. 2.4a, occurs for low adhesive strength at $\dot\gamma = 9$, in agreement with previous studies in bulk shear flow [58].

2.4 Results for homogeneous and hydrodynamically stagnant surface

Local bonds between polymer monomers and discrete surface binding sites induce strong friction effects that considerably slow down lateral motion close to the surface, as we will discuss in detail in Section 2.5. In this section, we elucidate the effects of high surface

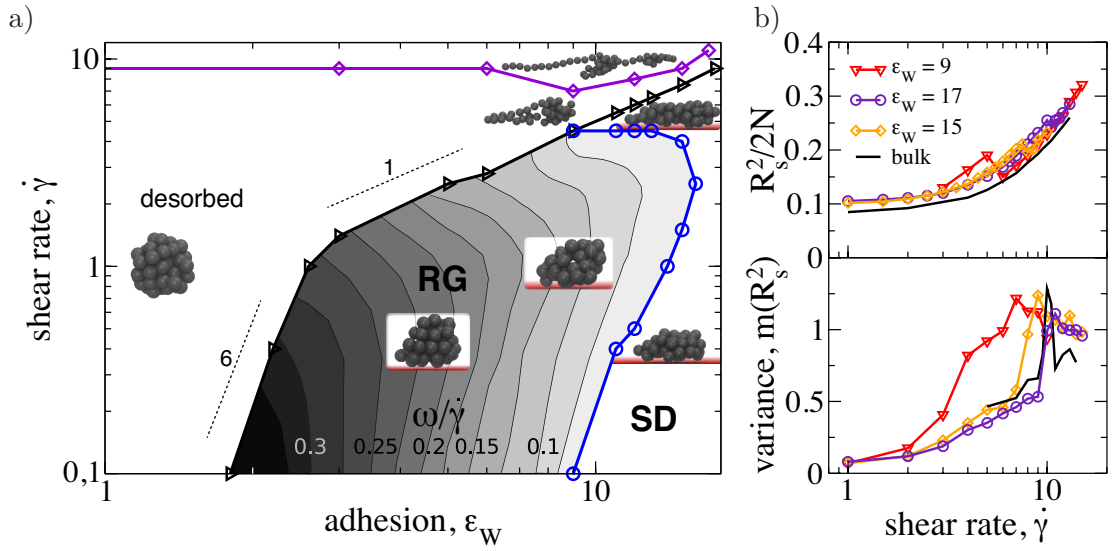

Figure 2.4: a) Dynamic state diagram for a globule with fixed cohesive strength $\varepsilon = 2$ at a homogeneous surface for varying shear rate $\dot{\gamma}$ and adhesive strength ε_W. The black line marks the desorption-adsorption transition. Slopes are indicated with dashed lines. The purple line denotes the stretch-transition at which the variance of the squared average extension $m(R_s^2)$ in (b) exhibits a peak. The transition from the rolling globule state (RG) to the slipping disk state (SD) is denoted by the blue line and defined by a value of the angular velocity of $\omega/\dot{\gamma} = 0.05$. Snapshots show representative polymer configurations.

friction in a coarse-grained model by imposing a reduced monomer mobility close to the laterally homogeneous surface, without actually resolving the discrete surface bindings sites. In the model we use in this section, the monomer self-mobility is reduced from a value of unity far away from the surface to a value of $\mu_S < 1$ within a finite distance range from the surface, as described by eq. 2.29, equivalent to a hydrodynamically stagnant surface layer. Alternatively, one can think of the reduced self-mobility as being due to a layer of grafted polymers.

In the following we concentrate on the effect of this reduced surface mobility on the globule adsorption transition for small shear rates. In the main part of fig. 2.5 we compare the adsorption transition for fixed cohesive strength $\varepsilon = 2$ for the case of homogeneous mobility $\mu_s = 1$ (solid lines) with the case of stagnant surface mobility $\mu_s = 0.01$ (dashed lines). The latter parameter value means that the monomer mobility is reduced by a factor of 100 close to the surface. For each surface mobility scenario we show results for free-draining (FD, gray lines) simulations and for simulations including hydrodynamic interactions (HI, black lines). The HI result for $\mu_s = 1$ thus agrees with the adsorption transition already shown in fig. 2.4a. Note that under equilibrium condition, i.e. in the limit $\dot{\gamma} = 0$, all four different models coincide within the numerical uncertainty.

Upon increasing the shear rate, we observe pronounced differences. In the presence of hydrodynamic interactions (black lines), an increase in shear rate induces desorption,

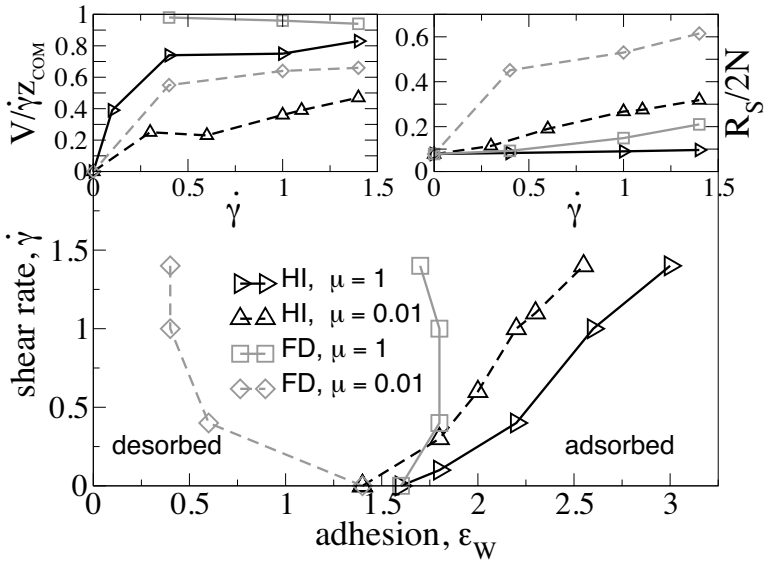

Figure 2.5: Results for a homogeneous surface with stagnant boundary layer. The dynamic state diagram shows the adsorption transition for a globule with fixed cohesive strength $\varepsilon = 2$ on a surface with potential range $\sigma_W = 1.5$. Black symbols include hydrodynamic interactions (HI); gray symbols are results from free-draining (FD) simulations. For solid lines the monomers mobility is homogeneous ($\mu_s = 1$), dashed lines show results for a stagnant surface layer within which the monomer mobility is reduced to one percent of the bulk value ($\mu_s = 0.01$). The insets show the rescaled velocity $V/\dot{\gamma} z_{\rm com}$ and the extension $R_s/2N$ in flow direction as a function of the shear rate for all four scenarios, measured along the respective adsorption transitions displayed in the main figure.

which can be rationalized by the presence of hydrodynamic lift forces [84, 112]. Going from a homogeneous mobility, $\mu_s = 1$, to a stagnant mobility, $\mu_s = 0.01$, only mildly changes the critical shear rate. We conclude that a surface friction that is increased by a factor of 100 enhances the adsorption tendency only very weakly.

In the free-draining case (FD) and for $\mu_S = 1$ (gray solid line), the adhesive strength needed for adsorption does not vary much with the shear rate, the adsorption transition is almost vertical. This reflects the absence of lift forces that would counteract adhesive forces. For the FD case with a reduced surface mobility $\mu_s = 0.01$ (gray broken line), we observe pronounced shear-induced adsorption of the globule; i.e., the adsorption transition shifts towards lower ε_W. In the insets we show results for the average extension in flow direction $R_s/2N$ and for the chain velocity rescaled by the unperturbed fluid velocity at the center-of-mass position $V/\dot{\gamma} z_{\rm com}$, measured along the adsorption transition line. One sees that the rescaled velocity is unity only in the free-draining case (FD) and for $\mu_S = 1$ (gray solid line), both surface friction and hydrodynamic interactions reduce the chain velocity. The velocity reduction leads to a pronounced chain elongation,

which promotes adsorption due to the reduced chain fluctuations [126]. In the FD case this gives rise to shear-induced adsorption, in the HI case this effect is overwhelmed by hydrodynamic lift forces and therefore shear-induced adsorption is not observed.

2.5 Results for inhomogeneous surface with discrete binding sites

2.5.1 Fixed shear rate, variable corrugation

Next we investigate how a more realistic surface binding model changes the adsorption behavior. We consider an inhomogeneous surface consisting of discrete binding sites, represented by Lennard-Jones centers, arranged on a square lattice with lattice constant $b = \tilde{b}/a = 2$ and located on a plane at position $z_W = 2$. In order to change the degree of corrugation, we vary the interaction range $\sigma_W < b$ defined in eq. (2.26) while keeping the density of binding sites constant. For lower surface binding site density, the critical adhesive strength for adsorption increases but otherwise the character of the adsorption transition does not change (data not shown). The important parameter in this section is the ratio of the interaction range and the lattice constant, σ_W/b, which controls the effective mobility of a monomer on the surface.

In fig. 2.6 we show the boundary between the adsorbed and the desorbed state for a globule with fixed cohesive strength of $\varepsilon = 2$ and for a fixed shear rate $\dot{\gamma} = 1$ as a function of the surface site interaction range σ_W and the adhesive strength ε_W. We compare free-draining simulations (FD, gray solid line) with hydrodynamic simulations (HI, black solid line) and also show equilibrium results in the absence of shear ($\dot{\gamma} = 0$, gray broken line). All three curves show that the critical adhesive strength increases in order to compensate for a shorter interaction range. When we compare the two FD curves, we see that a finite shear flow ($\dot{\gamma} = 1$, solid gray line) slightly weakens the adsorption and shifts the transition towards higher values of ε_W. As can be seen in the insets of fig. 2.6, the rescaled velocity $V/\dot{\gamma} z_{\mathrm{com}}$, measured along the adsorption transition line, decreases with decreasing interaction range σ_W as a result of enhanced surface friction, while the extension in flow direction $R_s/2N$, also measured along the transition line, increases strongly due to internal shear effects in the globule. This means that the inhomogeneous surface enhances unfolding of the FD polymer in shear flow but suppresses adsorption; in other words, the stretching of the chain, which by itself weakens entropic repulsion from the surface and therefore promotes adsorption [126], is overwhelmed by the weakened energetic attraction to the surface since the monomers are constantly pulled away from the surface binding sites [68, 75].

In the presence of hydrodynamic interactions (solid black line in fig. 2.6) hydrodynamic lift forces additionally weaken the adsorption propensity. Due to the decreased monomer self-mobility at the surface, the globule velocity $V/\dot{\gamma} z_{\mathrm{com}}$ (black line in inset fig. 2.6) is further reduced when compared with the FD case (gray line). Hydrodynamic screening

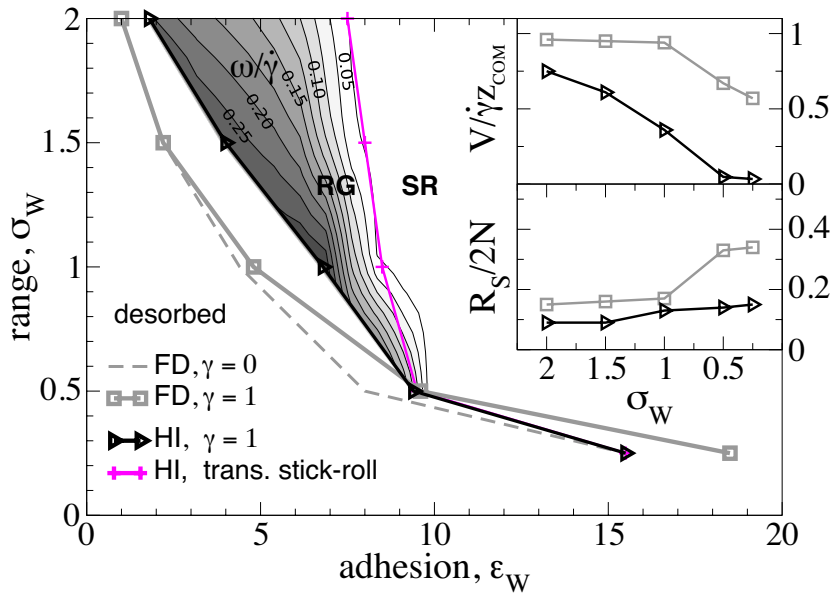

Figure 2.6: Dynamic state diagram for a globule with fixed cohesive strength $\varepsilon = 2$ at an inhomogeneous surface as a function of the adhesive strength ε_W and the interaction range σ_W of the binding sites. The solid black and gray lines denote the adsorption transition at fixed shear rate $\dot{\gamma} = 1$ in the presence (black) and absence (gray) of hydrodynamic interactions. For comparison, the dashed gray line denotes the equilibrium adsorption transition without shear, $\dot{\gamma} = 0$. The transition from the rolling globule state (RG) to the stick-roll state (SR) is denoted by the magenta line and defined by a maximum in the variance of the squared translational velocity $m(V^2)$, see fig. 2.7b. The underlying contour plot shows the angular velocity $\omega/\dot{\gamma}$. The transition to the stick-roll state approximately coincides with the previous criterion for the roll-slip transition $\omega/\dot{\gamma} = 0.05$. The insets show the rescaled velocity $V/\dot{\gamma}z_{\mathrm{com}}$ and the extension $R_s/2N$ as a function of σ_W measured along the respective adsorption transition lines.

effects that are connected to the flow stagnation inside the globule reduce the chain elongation $R_s/2N$ when compared with FD simulations (black and gray lines in lower inset fig. 2.6). The contour plot of the rescaled angular velocity $\omega/\dot{\gamma}$ in fig. 2.6 illustrates that the globule rolling motion is essentially arrested for short interaction ranges $\sigma_W \leq 0.5$. As a result, short ranges lead to an adsorption transition at an adhesive strength comparable to the equilibrium case. As opposed to the case of a homogeneous surface, where we observe a transition to a slipping state, for the inhomogeneous surface we observe a transition to stick-roll motion, indicated by the magenta line in fig. 2.6, which is defined by a peak in the variance of the squared globule velocity $m(V^2)$ in fig. 2.7b. Note that this criterion almost exactly coincides with our previous definition of the transition from rolling to slipping, $\omega/\dot{\gamma} = 0.05$.

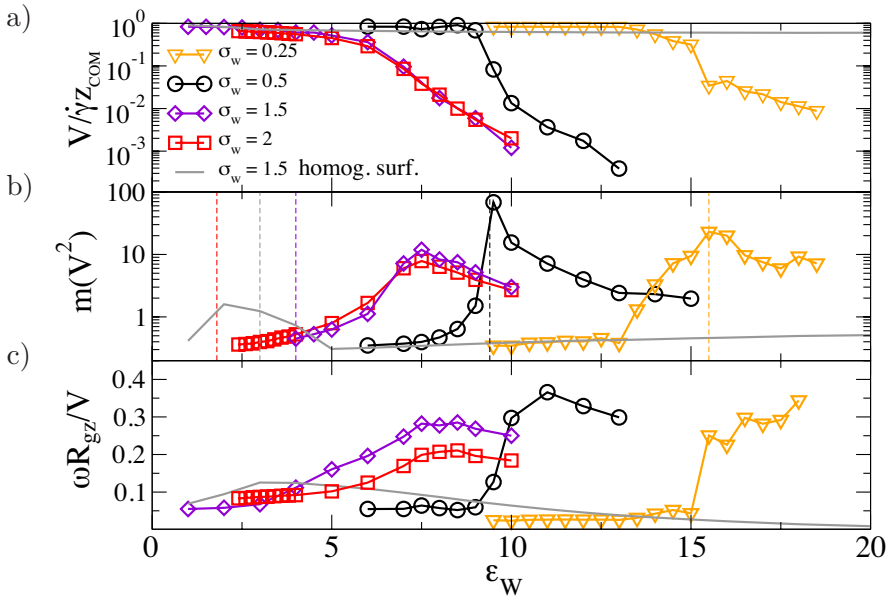

Figure 2.7: Results for the inhomogeneous surface for a few different values of the binding site interaction range σ_W for fixed $\epsilon = 2$ and $\dot{\gamma} = 1$. For comparison, we include results for the homogeneous surface (gray lines). a) The rescaled translational velocity $V/\dot{\gamma}z_{\mathrm{com}}$ decreases over several orders of magnitude with increasing ϵ_W. b) The variance of the squared average velocity $m(V^2)$ shows a peak which defines the transition to the stick-roll state. Dashed vertical lines mark the globule adsorption transition. c) Although both angular and translational velocities are very small in the stick-roll state, the ratio $\omega R_{gz}/V$ is of the order of unity and thus indicative of intermittent rolling motion.

2.5.2 The stick-roll state

In fig. 2.7 we plot the average rescaled velocity $V/\dot{\gamma}z_{\mathrm{com}}$, the variance $m(V^2)$, defined similarly to eq. (2.30), as well as the ratio of the rescaled angular and translational velocities $\omega R_{gz}/V$ for a few fixed values of the interaction range σ_W as a function of the surface adhesion strength ε_W. While $V/\dot{\gamma}z_{\mathrm{com}}$ in fig. 2.7a decreases over several orders of magnitude upon increasing ε_W, the variance $m(V^2)$ in fig. 2.7b shows a well-defined peak which defines the transition to the stick-roll state (SR). For short interaction ranges $\sigma_W \leq 0.5$ this transition coincides with the adsorption transition, denoted in fig. 2.7b by dashed vertical lines, which means that for a highly corrugated surface potential an adsorbed globule is always in the stick-roll state. In fig. 2.7 we also include results for the homogeneous surface for $\sigma_W = 1.5$ (gray line). For this case the average velocity in fig. 2.7a approaches a constant value of about $V/\dot{\gamma}z_{\mathrm{com}} = 0.6$ and the variance $m(V^2)$ in fig. 2.7b is rather small, only displaying a weak peak at the adsorption transition. For the inhomogeneous surface the ratio $\omega R_{gz}/V$ in fig. 2.7c displays a maximum for large adhesion ε_W meaning that angular and translational velocities are synchronized. For the

homogeneous surface, on the other hand, we observe slipping at large ε_W meaning that the angular velocity is much lower than the translational velocity.

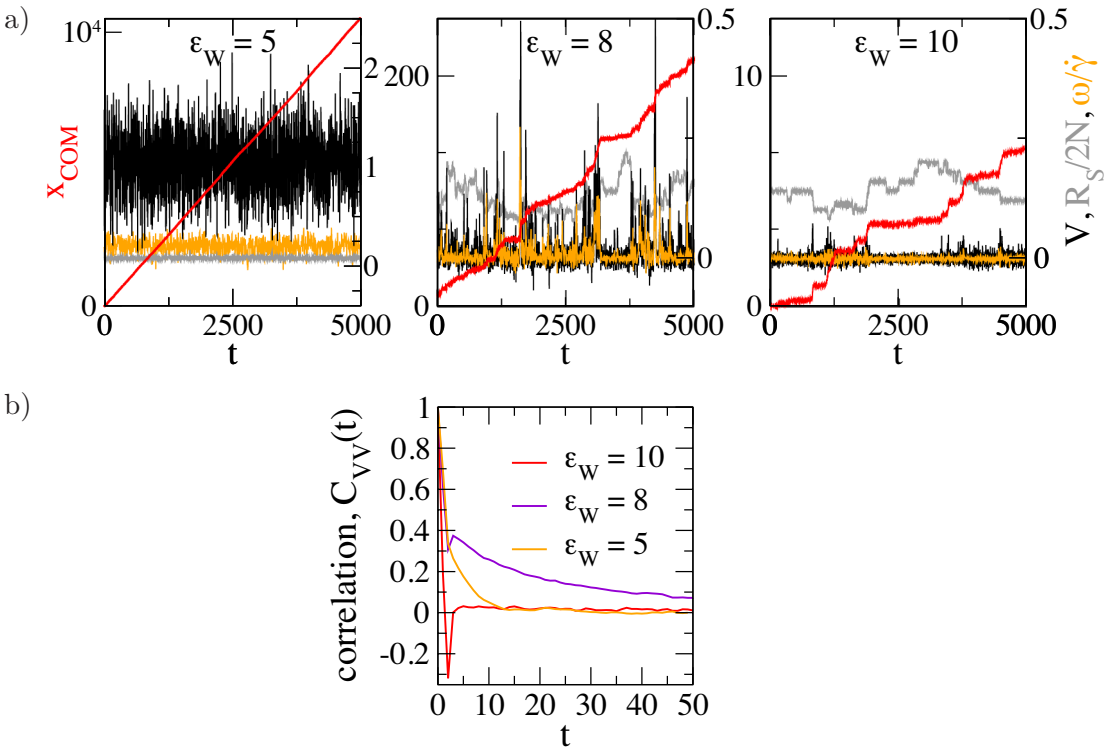

Figure 2.8: a) Time series at an inhomogeneous surface with binding site potential range $\sigma_W = 1.5$ for fixed $\epsilon = 2$ and $\dot{\gamma} = 1$. For the different values $\varepsilon_W = 5, 8, 10$ we show the chain displacement in flow direction x_{com} (red), the translational velocity V (black), the angular velocity $\omega/\dot{\gamma}$ (orange) and the chain extension $R_s/2N$ (gray). While for $\varepsilon_W = 5$ the globule rolls continuously like on a homogeneous surface, for $\varepsilon_W = 8$ one sees pronounced steps in the displacement and intermittent peaks in the velocity. For $\varepsilon_W = 10$, the polymer is arrested over extended periods of time. b) Velocity-velocity autocorrelation functions.

The transition from rolling to stick-roll motion is further illustrated by time series in fig. 2.8a for fixed $\sigma_W = 1.5$ and for three different values of the adhesive strength ε_W that all correspond to adsorbed globule states. Only weak friction effects are observed for $\varepsilon_W = 5$, where the globule continuously moves over the surface with modest relative fluctuations of the velocity V (black line) around its mean and the displacement x_{com} (red line) continuously increases with time, similar to the homogeneous surface. Deformations of the globule are weak; the extension $R_s/2N$ (gray line) is small and almost constant. For $\varepsilon_W = 8$ the maximal variance $m(V^2)$ is reached (compare fig. 2.7b). Accordingly, the velocity V in fig. 2.8a shows pronounced peaks and the globule is temporarily stuck on the surface, indicated by plateaus in x_{com} (red). The close correlations between peaks in the velocity and the angular velocity $\omega/\dot{\gamma}$ lead to the conclusion that the polymer moves by instantaneous rolling rather than slipping events, hence the name stick-roll

state. The plateaus in the extension $R_s/2N$ (gray line) suggest that the rolling events are accompanied by unwinding and refolding of the polymer. Increasing the adhesion even further to $\varepsilon_W = 10$ extends the periods over which the globule is stuck on the surface.

In fig. 2.8b we show autocorrelation functions of the translational velocity $C_{VV}(t)$, defined by eq. (2.32). For a globule in the rolling globule (RG) state for $\varepsilon_W = 5$, the velocity autocorrelation decays quickly. For a polymer in the stick-roll (SR) state for $\varepsilon_W = 10$, $C_{VV}(t)$ decays even faster and exhibits an anti-correlated regime, indicative of alternating switching between periods of motion and periods of arrest on the surface. The longest correlation time is observed for intermediate adhesion $\varepsilon_W = 8$, reflecting that this is the location of a transition from rolling to stick-roll behavior.

2.5.3 Variable shear rate, fixed corrugation

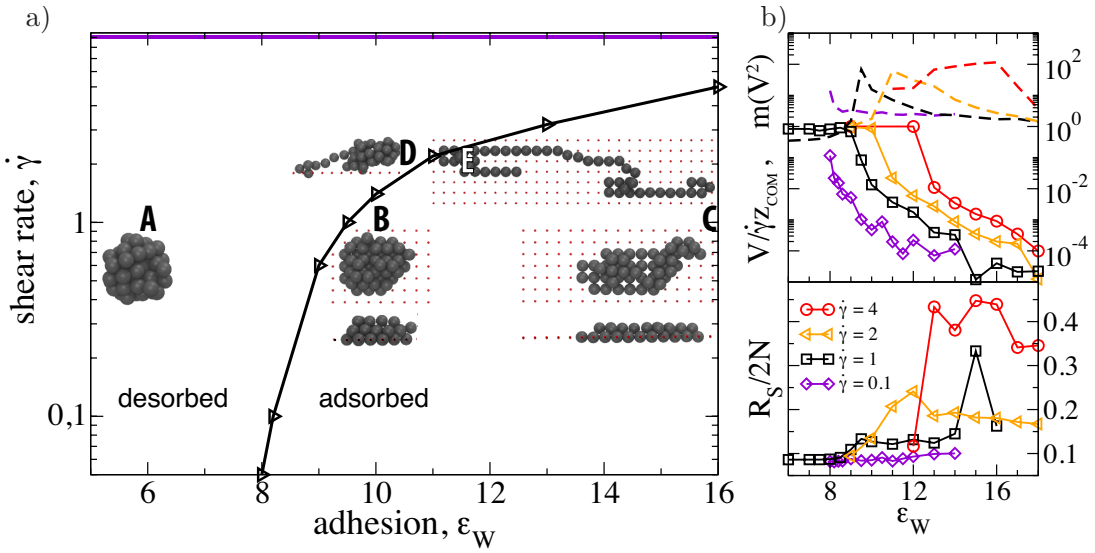

Figure 2.9: a) Dynamic state diagram for a globule with fixed cohesive strength $\varepsilon = 2$ at an inhomogeneous surface with fixed binding site potential range $\sigma_W = 0.5$ as a function of shear rate $\dot\gamma$ and adhesive strength ε_W. The black line marks the desorption-adsorption transition. The stretch transition occurs in the desorbed state and is denoted by the purple line. Snapshots (top and side views) show representative polymer configurations for $\dot\gamma = 1$ (A-C) and for $\dot\gamma = 2$ (D,E), where red dots represent surface binding sites. b) The drastic decrease of the rescaled translational velocity $V/\dot\gamma z_{\rm com}$ (solid lines) in the adsorbed state and the large variance $m(V^2)$ (dashed lines) indicate stick-roll motion. Due to deformation and unfolding at high shear rates, the average extension R_s increases.

We next study the adsorption behavior for fixed range of the surface binding sites $\sigma_W = 0.5$ and variable shear rate $\dot\gamma$; as before we fix the cohesive strength at $\varepsilon = 2$. In fig. 2.9a we show the state diagram including the adsorption transition (black line). The diagram is similar as for the homogeneous surface in fig. 2.4, the higher the shear rate,

the stronger the critical adhesive strength; i.e., shear promotes desorption. Included are typical globule snapshots at parameters denoted by the adjacent labels. The globule, which exhibits a spherical shape in the desorbed state, see snapshot (A), adsorbs for $\dot{\gamma} = 1$ at an adhesive strength $\varepsilon_W = 9.5$ and exhibits a disk-like conformation, see (B). The peak of $m(V^2)$ for $\dot{\gamma} = 1$ in fig. 2.9b occurs roughly at $\varepsilon_W = 9.5$ and shows that the adsorbed state corresponds to the stick-roll state. The average velocity $V/\dot{\gamma} z_{\mathrm{com}}$ in the adsorbed state is reduced by orders of magnitude compared to the homogeneous surface. The average extension $R_s/2N$ for $\dot{\gamma} = 1$ only slightly increases with increasing adhesive strength ε_W, as seen in the snapshot (C) and also in fig. 2.9b. At higher shear rate $\dot{\gamma} = 2$ stronger deformations are obtained, see snapshot (E). The snapshot (D) shows a stretched state where only few beads are in contact with the surface; in fact, snapshot (D) is taken just before the polymer desorbs.

2.6 Summary and conclusion

In the first part we investigate the adsorption behavior of a globule at a homogeneous surface for varying cohesive and adhesive strengths and shear rates. The dynamic state diagram features different rolling and slipping states: the rolling globule state, the rolling prolate state, and the rolling folding-unfolding state. Slipping globules are observed for large adhesion and slipping coil conformation are found for low cohesion. Shear does not promote or enhance adsorption. For non-zero shear, we identify two cyclic processes in terms of the chain elongation and the separation from the surface.

In the second part surface friction effects are accounted for by a hydrodynamically stagnant surface layer, within which the mobility is reduced. This results in a local velocity reduction of the chain and thus to increased elongation in flow direction. While this leads to a shear-induced adsorption in the freely draining situation, in the presence of hydrodynamic interactions the stagnant surface layer does not change the adsorption behavior drastically. We next consider an inhomogeneous surface consisting of discrete binding sites having a variable interaction range. The resulting surface friction leads to a drastic velocity reduction when including full hydrodynamic interactions. Although this reduces the hydrodynamic lift force, the effective surface adhesion strength is reduced so that adsorption is disfavored when compared to the limit of no shear. This is similar to the analysis of a simple model of a monomer dragged along a corrugated potential [68].

One result of our work is that for a simple interaction model based on a static Hamiltonian consisting of pair potentials between monomers and the surface, the globule adsorption is not enhanced by the presence of shear, leading to the tentative conclusion that in order to observe such a behavior, a more complex binding mechanism including saturating or catch bonds [9] is needed. This in turn suggests to construct more complex potential-based binding models for the interaction of collapsed proteins with surfaces or with colloidal particles in shear, in order to model biological important situations such as the adsorption

of the von Willebrand factor on vessel walls in shear [31] and the flow-driven polymer-colloid composite formation [8]. Hence, in future work the von Willebrand domain structure could be resolved by a more detailed coarse-grained heteropolymer model. Another interesting question is how catch bond behavior, which in previous simulation work has been implemented in Langevin simulations by a heuristic two-state reaction bond model [76], can be modeled in a purely potential-based Langevin simulation.

Chapter 3

Shear-enhanced adsorption of a homopolymeric globule mediated by surface catch bonds

3.1 Introduction

Some biological bonds exhibit prolonged lifetimes in the presence of tensile forces, a counter-intuitive phenomenon referred to as catch bond behavior [89, 90]. Experimental evidence for catch bond behavior comes from studies on various receptor-ligand complexes [9, 86, 87, 91, 98] and motivated atomistic [99, 103] as well as mesoscopic [127] simulation studies with the goal to characterize and explain the underlying mechanisms. As a matter of fact, also force-insensitive bonds have been reported [98], which can be viewed as intermediate between catch bonds and the more common slip bonds.

How individual biological bonds respond to forces has profound implications for the surface-adhesion of biomacromolecules under flow conditions. The present study is motivated by the blood protein von Willebrand Factor (VWF), which plays a key role in hemostasis [27] by unfolding and activation at elevated shear rates and subsequent binding to the vessel wall [27, 31, 110]. Catch bond behavior has been found in the binding of VWF A1 domain to platelets' GPIbα [86, 87], and also the collagen mediated binding of VWF to blood vessel walls was suggested to exhibit a non-trivial force dependence [31].

Recently, we have shown that for simple coarse-grained polymer models based on a time-independent Hamiltonian entirely consisting of energy-conserving pair potentials between monomers and the surface, adsorption is not enhanced in the presence of shear flow [128], i.e., hydrodynamic shear always favors the desorbed state of a single globular or coiled polymer [84, 113]. This stands in contrast to experimental findings on VWF adhesion under high flow conditions [31], and thus suggests that in order to obtain shear-induced adsorption behavior, slip-resistant catch bonds might be a necessary ingredient. That catch bonds are in fact sufficient to induce adsorption of polymeric globules on surfaces by shear has been demonstrated in pioneering work by Sing and Alexander-Katz [7, 76], an observation that forms the starting point for the present investigations.

Here, we study the adsorption of globular polymers by stochastic two-state surface-monomer bonds, which is a model that for particular parameter values was previously

shown to lead to shear-induced adsorption [76]. Similar models with simple two-state kinetics have proven useful in a number of studies since it is relatively straightforward to include the force-dependent bond stability in a heuristic manner so that either slip or catch bond behavior is obtained [7, 8, 76, 88, 109]

We present adsorption state diagrams as a function of shear rate, the surface-monomer bond dissociation and association rates and an effective catch bond parameter that describes the continuous change from slip to catch bond behavior. The adsorption transition displays shear-induced adsorption only for rather low dissociation and association rate and only for bonds that show neither pronounced slip nor catch bond behavior.

In the last part, we compare the stochastic two-state surface-monomer bond model with a binding scenario based on conservative surface-monomer potentials, similar to that used in our previous study [128]. We find that in order to see shear-induced adsorption phenomena, surface-monomer potentials should presumably have an extremely short spatial range, which makes simulations impractical for large system sizes.

3.2 Simulation method

Brownian hydrodynamics simulations are performed using the discretized Langevin equation

$$\mathbf{r}_i(t+\Delta t) - \mathbf{r}_i(t) = \left(\boldsymbol{\mu}_{ii}\dot{\gamma} z_i \hat{\mathbf{x}} - \sum_{j=1}^{N} \boldsymbol{\mu}_{ij} \cdot \nabla_{\mathbf{r}_j} U(t) + \sum_j \nabla_{\mathbf{r}_j} \boldsymbol{\mu}_{ij} \right) \Delta t + \boldsymbol{\xi}_i(\Delta t), \quad (3.1)$$

which describes the displacement of bead i during a time step Δt. Note that all quantities are made dimensionless by rescaling lengths by the monomer radius a according to $r = \tilde{r}/a$, energies $U = \tilde{U}/\mathrm{kT}$ by the thermal energy and times $t = \tilde{t}/\tau$ by the characteristic monomer diffusion time $\tau = a^2/\mu_0\,\mathrm{kT} = 6\pi\eta a^3/\mathrm{kT}$, with Stokes mobility μ_0 and viscosity η. The first term in eq. (3.1) represents a linear shear flow with rate $\dot{\gamma} = \tilde{\dot{\gamma}}\tau$, where $\hat{\mathbf{x}}$ is the unit vector in x-direction. The second term accounts for the direct force acting on particle i itself as well as the hydrodynamic flow-field created by forces acting on all other particles $j \neq i$. Hydrodynamic interactions at a surface with no-slip boundary condition are taken into account via the mobility matrix approximated by the Rotne-Prager-Blake tensor [63, 118, 120] given by

$$\boldsymbol{\mu}_{ij} = \tilde{\boldsymbol{\mu}}_{ij}/\mu_0 = \boldsymbol{\mu}^{\mathrm{RPB}}_{\mathrm{self}}(z_i)\delta_{ij} + (1-\delta_{ij})\,\boldsymbol{\mu}^{\mathrm{RPB}}(\mathbf{r}_i, \mathbf{r}_j). \quad (3.2)$$

The explicit expressions for the self-mobilities $\boldsymbol{\mu}^{\mathrm{RPB}}_{\mathrm{self}}(z_i)$ and the off-diagonal elements $\boldsymbol{\mu}^{\mathrm{RPB}}(\mathbf{r}_i, \mathbf{r}_j)$ have been given previously [63]. The third term in eq. (3.1) compensates for the spurious flux due to inhomogeneities in the self-mobility [3]. The stochastic contribution $\boldsymbol{\xi}_i$ is given by Gaussian random vectors with correlations according to the fluctuation-dissipation theorem $\left\langle \boldsymbol{\xi}_i \boldsymbol{\xi}_j \right\rangle = 2\boldsymbol{\mu}_{ij}\Delta t$ and vanishing mean. The simulations

typically run for 10^9 time steps of length $\Delta t = 10^{-4}$. For computational speed we update the mobility matrix $\boldsymbol{\mu}_{ij}$ only every 100 time steps, which does not alter the results.

The homopolymer model consists of $N = 50$ beads, which interact via Lennard-Jones potentials of depth $\varepsilon = \tilde{\varepsilon}/\mathrm{kT} = 2$ and are connected in a linear chain by harmonic bonds with a rescaled spring constant $\kappa = \tilde{\kappa}a^2/\mathrm{kT} = 200$. The value chosen for ε corresponds to a strongly collapsed globule, which, however, is still far from a crystallization transition that for $N = 50$ occurs at about $\varepsilon = 4$ [129]. The intra-polymer potential is given by

$$U_{\mathrm{pol}} = \varepsilon \sum_{i<j} \left(\left(\frac{2}{r_{ij}} \right)^{12} - 2 \left(\frac{2}{r_{ij}} \right)^{6} \right) + \frac{\kappa}{2} \sum_{i} \left(r_{i,i+1} - 2 \right)^2 . \tag{3.3}$$

The total potential energy $U = U_{\mathrm{pol}} + U_{\mathrm{rep}}$ includes in addition a surface term U_{rep} that accounts for steric exclusion of the polymer from the surface and in particular prevents crossing of the no-slip boundary located at $z = 0$. We use

$$U_{\mathrm{rep}} = \sum_{i} \begin{cases} 2\pi\sigma_R^2 \left(\frac{2}{5} \left(\frac{\sigma_R}{z_i} \right)^{10} - \left(\frac{\sigma_R}{z_i} \right)^{4} + \frac{3}{5} \right) & z_i \leq \sigma_R \\ 0 & z_i > \sigma_R \end{cases} \tag{3.4}$$

with a short range of $\sigma_R = 1.2$. The maximal height above the surface is restricted by a soft wall acting on the polymer center-of-mass located at a height $z = 15$.

Surface adhesion is modeled via surface-monomer bonds that are governed by stochastic two-state kinetics. A monomer can reversibly bind to the surface when it is within the surface reaction range $z_r = 2$ above the no-slip boundary, regardless of its lateral position. The binding probability is determined by the adsorption rate. When the monomer is bound its mobility is set to zero, i.e., the position is frozen despite of hydrodynamic and direct forces due to other beads. The virtual force acting on an immobilized monomer is not included in the off-diagonal mobility terms in eq. (3.1), which means that an immobilized monomer is transparent to the flow or, in other words, that it perfectly fits into surface defects without modifying the surface flow boundary condition. Adsorption and desorption rates can be interpreted in terms of energy barrier heights E_a and E_d, respectively, in a fictitious energy landscape. The equilibrium behavior is governed by the energy difference $\Delta E = E_d - E_a$. With a pre-factor ν, the so-called attempt frequency, the adsorption rate becomes

$$k_{\mathrm{a}} = \nu e^{-E_a}, \tag{3.5}$$

while the desorption rate is given by

$$k_{\mathrm{d}} = \nu e^{-(E_d - xf)}, \tag{3.6}$$

where the catch bond parameter x sets the sensitivity of the desorption rate to the force f acting on the bound particle i, defined by $f = |\dot{\gamma} z_i \hat{\mathbf{x}} - \nabla_{\mathbf{r}_i} U|$. In the calculation of f we omit stochastic forces, which have vanishing mean, as well as hydrodynamic interactions, considering immobilized monomers to be transparent to the flow field created by other

monomers, as discussed earlier. Attempts for bond formation for each monomer within the surface reaction range, $z \leq z_r = 2$, and dissociation for each existing surface bond are performed with a frequency $\nu = \tilde{\nu}\tau = 100$. Thus, in the simulation, bonds are updated every 100 time steps ($\Delta t = 10^{-4}$) and the bond force f is averaged during this time interval. Note that the update of the mobility matrix $\boldsymbol{\mu}_{ij}$ occurs with the same frequency. As opposed to a similar study [76] we do not represent surface bonds by harmonic springs which are suddenly switched on, as this can lead to abrupt changes of tensile spring forces for newly formed bonds and thereby affect the balance between dissociation and association rates.

3.3 Results

3.3.1 Equilibrium adsorption

First we consider the adsorption behavior of a collapsed polymer in equilibrium without shear flow. As shown in fig. 3.1a, the average height of the center-of-mass $z_{\mathrm{com}} = N^{-1}\sum_i^N z_i$ relative to the surface decreases with rising adsorption energy ΔE while the rescaled average number of bonds N_b/N in fig. 3.1b increases . The adsorption transition, indicated by the dotted horizontal line, is defined by the distance criterion $z_{\mathrm{com}} = 7$, which is chosen so that z_{com} exhibits maximal slope at the adsorption transition, as illustrated in fig 3.1a. The average number of bonds at the adsorption transition is of the order of $N_b/N \approx 0.05$, meaning that roughly two to three surface-monomer bonds are present at the transition. Upon changing from slip bond, $x > 0$, to catch bond behavior, $x \leq 0$, the equilibrium adsorption transition shifts towards smaller values of ΔE, meaning that catch bond behavior enhances the adsorption. This follows from the fact that the ratio of the adsorption and desorption rates defined in eqs. (3.5),(3.6) is given by $k_a/k_d = e^{\Delta E - xf}$ where the force f acting on the surface bond is a positive definite quantity. As shown in fig. 3.1c, the average height z_{com} for different values of x fall on a single curve when plotted as a function of $\Delta E - xf_r$, where f_r is the force acting on the bond at the moment of rupture. In fig. 3.1d we confirm that the simulation results do not depend on the initial conditions, i.e. there is no difference in the equilibrium globule height for simulations initialized with a desorbed, unbound globule and simulations initialized with an adsorbed globule where a single, randomly chosen bead is bound to the surface. For the results shown in fig. 3.1, the force-independent adsorption energy barrier is kept constant at a value $E_a = 9$.

3.3.2 Varying catch bond parameter at fixed adsorption and desorption rates

An important question concerns the effect of the catch bond parameter x on the non-equilibrium adsorption behavior in shear flow. For positive values of x, the surface bonds

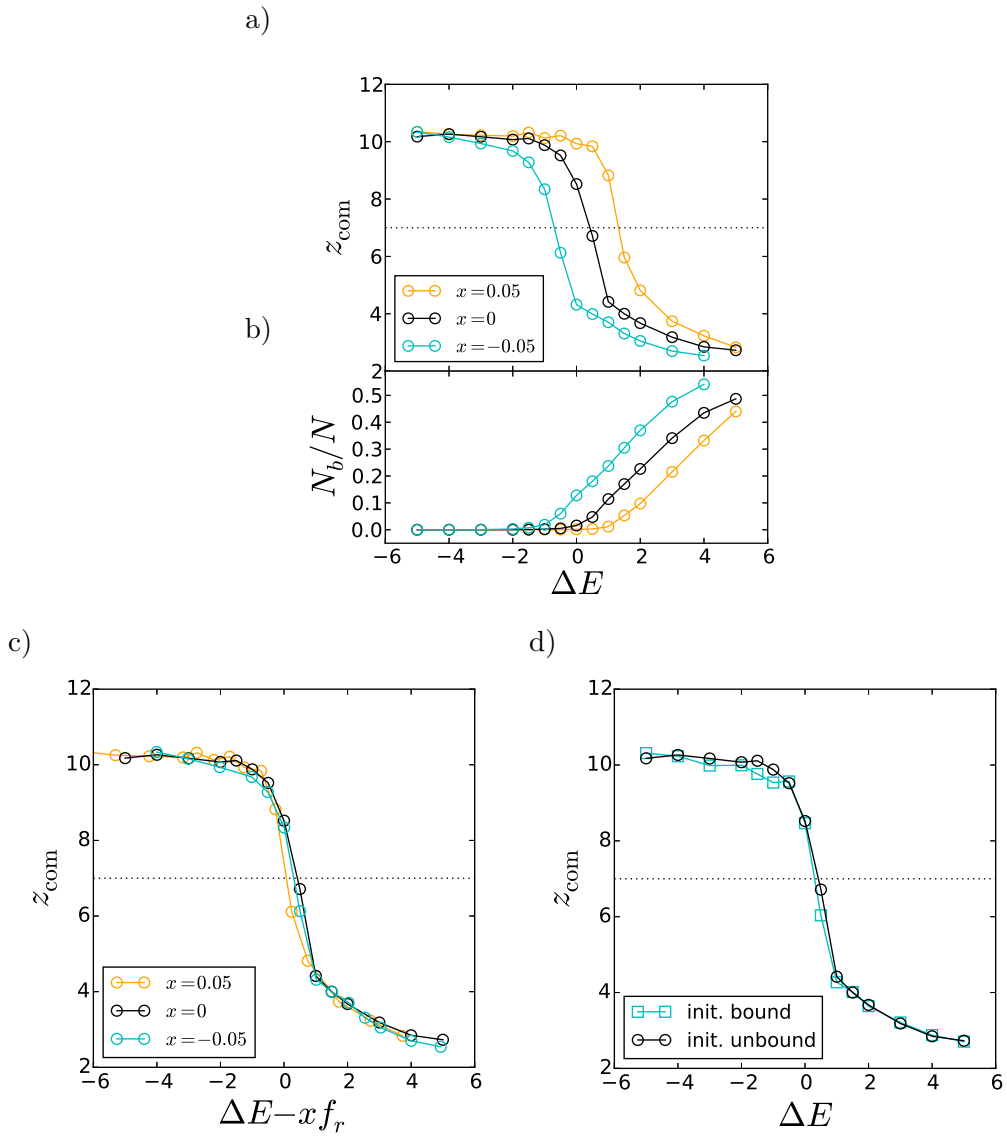

Figure 3.1: Adsorption of a collapsed polymer with cohesive strength $\varepsilon = 2$ and number of monomers $N = 50$ in the absence of shear flow. The adsorption energy barrier is fixed at $E_a = 9$. A horizontal black dotted line indicates the adsorption transition threshold defined as $z_{\mathrm{com}} = 7$. a) The average height of the polymer center-of-mass z_{com} and b) the rescaled average number of bonds N_b/N are plotted as a function of the adsorption energy ΔE. Upon changing from slip bond behavior, $x = 0.05$ (orange), to catch bonds, $x = -0.05$ (cyan), the equilibrium adsorption transition shifts towards smaller ΔE. c) When the adsorption energy is shifted by the average force acting on the surface bonds at the moment of rupture, $\Delta E - x f_r$, the data for z_{com} fall on a single curve regardless of the value of x. d) The equilibrium adsorption behavior is independent of the initial configuration, as demonstrated for $x = 0$; simulations are either initialized in the desorbed state (black) or in a state where the globule is bound to the surface via a randomly chosen bead (cyan).

exhibit the usual slip behavior and are weakened when a force acts on the bond. Changing the catch bond parameter towards negative values leads to bonds that become stronger under force, which effectively might enhance adsorption in shear flow. Indeed, it has been shown that shear induces adsorption for low desorption rates k_d and for vanishing catch bond parameter $x = 0$ [76]. In the following we determine the range of parameters for which adsorption is enhanced by shear.

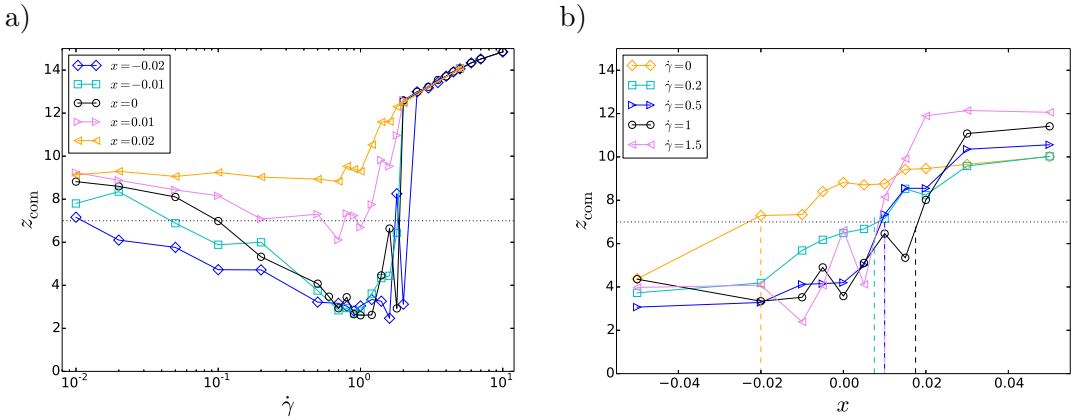

Figure 3.2: a) Average height of the polymer center-of-mass z_com as a function of shear rate $\dot\gamma$ for different fixed values of the catch bond parameter x. Surface bonds are characterized by high adsorption and desorption energy barriers $E_a = E_d = 9$. Whereas $x < 0$ corresponds to catch bonds, positive x corresponds to slip bond behavior. The dotted horizontal line indicates the adsorption transition defined by the distance criterion $z_\mathrm{com} = 7$. b) Average height z_com as a function of x for different shear rates and fixed $E_a = E_d = 9$. The adsorption transition is indicated by vertical dashed lines.

In order to determine the adsorption transition we plot the average height of the polymer center-of-mass z_com in fig. 3.2a as a function of shear rate $\dot\gamma$ for a few fixed values of the catch bond parameter x and in fig. 3.2b as a function of x for a few different fixed values of $\dot\gamma$. Low rates of bond formation and dissociation are obtained by choosing high values for the adsorption and desorption energy barriers, $E_a = E_d = 9$. The choice of $\Delta E = E_d - E_a = 0$ ensures proximity to the adsorption transition, as can be seen in fig. 3.1a.

Indeed, pronounced shear-induced adsorption is observed for $x = 0$ in fig. 3.2a, in agreement with literature results [76]; at low shear rates $\dot\gamma < 0.1$ the globule is in the desorbed state, defined by the distance criterion $z_\mathrm{com} > 7$ and indicated by the horizontal dotted line. Further increasing the shear rate leads to adsorption until the desorbing lift force overwhelms the surface adhesion around $\dot\gamma = 1.9$. Whereas slip bonds with $x = 0.02$ always lead to desorption (orange symbols), small negative values of x, i.e. catch bond behavior, favors adsorption at low shear rates but with increasing shear the globule also desorbs. As can be seen in fig. 3.2b, increasing the catch bond parameter x coming from negative values, where the polymer is adsorbed, leads to a desorption transition. This

shear-dependent desorption transition, induced by changing the bonds from catch to slip behavior, is indicated by vertical dashed lines.

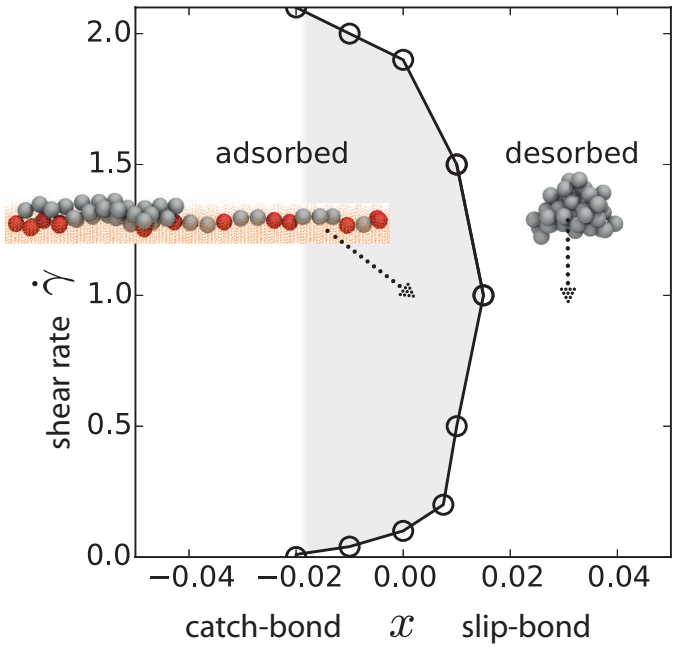

Figure 3.3: Adsorption state diagram as a function of shear rate $\dot{\gamma}$ and catch bond parameter x for a collapsed polymer with cohesive strength $\varepsilon = 2$. Stochastic surface bonds are characterized by adsorption and desorption energy barriers $E_a = E_d = 9$. Only within the small shaded region $-0.02 < x < 0.02$, shear-induced adsorption is observed in a finite window of intermediate shear rates. Snapshots illustrate an adsorbed configuration obtained for $\dot{\gamma} = 1$, $x = 0$, where beads that are bound to the surface are colored in red, and a desorbed globule obtained for $\dot{\gamma} = 1$, $x = 0.03$ in the desorbed part of the state diagram.

As a result, we obtain the adsorption state diagram in fig. 3.3, showing the adsorption transition of a collapsed globule as a function of rescaled shear rate $\dot{\gamma}$ and the catch bond parameter x. Although the hydrodynamic interactions included in the simulations lead to hydrodynamic lift forces that work against adsorption [84, 113], in a small parameter range of $-0.02 < x < 0.02$ we observe shear-induced adsorption. The state diagram in fig. 3.3 displays reentrant behavior, i.e., adsorption is only observed within a finite small window of intermediate shear rates. Surprisingly, the existence of shear-induced adsorption is very sensitive to the value of the catch bond parameter x. We note that whether the polymer is desorbed at high shear rates depends on the initial conditions of the simulation, as discussed below.

To obtain a feeling for the strong influence of the catch bond parameter on the desorption rate, we present in fig. 3.4 data for the average rupture force f_r, defined as the force acting on a bond at the moment of dissociation, for the same parameter values already shown in fig. 3.2a. According to the adsorption state diagram fig. 3.3, shear-induced adsorption occurs in the range $-0.02 < x < 0.02$. In the range of shear rates where the

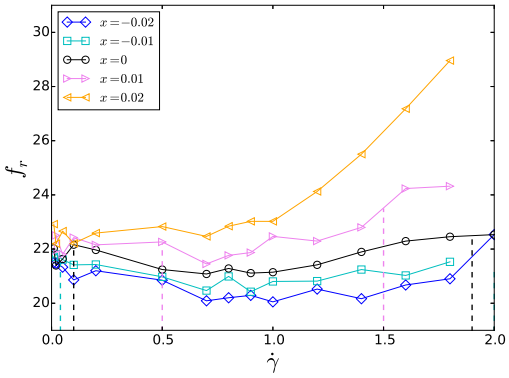

Figure 3.4: Average rupture force f_r as a function of shear rate $\dot{\gamma}$ for the same parameters as in fig. 3.2a. Vertical dashed lines indicate the adsorption transition.

globule is adsorbed, the rupture force in fig. 3.4 is approximately $f_r = 22 \pm 1$. According to the definition of the desorption rate in eq. (3.6), the force changes the desorption rate by a factor e^{xf_r}, which using $f_r = 22$ translates into $0.64 < e^{xf_r} < 1.55$ for a range of $-0.02 < x < 0.02$. We conclude that although the catch bond parameter x is very small in the range where shear-induced adsorption is observed, due to the large values of the rupture forces f_r the effect on the dissociation rates is sizable, explaining the surprising sensitivity of the resulting adsorption behavior on x.

3.3.3 Varying adsorption and desorption rates at fixed catch bond parameter

The shear-dependent adsorption behavior depends on both the adsorption energy barrier E_a and the desorption energy barrier E_d. In fig. 3.5a we present the globule center-of-mass height z_{com} as a function of shear rate for fixed catch bond parameter $x = 0$ and fixed adsorption energy barrier height $E_a = 9$ for a few different values of the adsorption energy $\Delta E = E_d - E_a$. The data exhibit clear shear-induced adsorption for $\Delta E = 0$ (black data points) whereas a positive value $\Delta E = 0.5$ leads to adsorption for low shear rates and a negative value $\Delta E = -0.5$ promotes desorption for all values of $\dot{\gamma}$. The effect of varying ΔE at fixed $x = 0$ and $E_a = 9$ is summarized in the adsorption state diagram fig. 3.6a. We see that shear-induced adsorption is only observed within a very narrow range of adsorption energies $-0.3 < \Delta E < 0.4$.

Next we determine the globule adsorption behavior for varying adsorption energy barrier height E_a at fixed catch bond parameter $x = 0$. For this we fix the adsorption energy at $\Delta E = E_d - E_a = 0$, meaning that we vary both adsorption and desorption barrier heights so that the equilibrium adsorption behavior stays invariant. In fig. 3.5b we show the average polymer height as a function of E_a for a few fixed shear rates $\dot{\gamma}$ and for $\Delta E = 0$, we observe adsorption only for intermediate values of E_a. These results are summarized

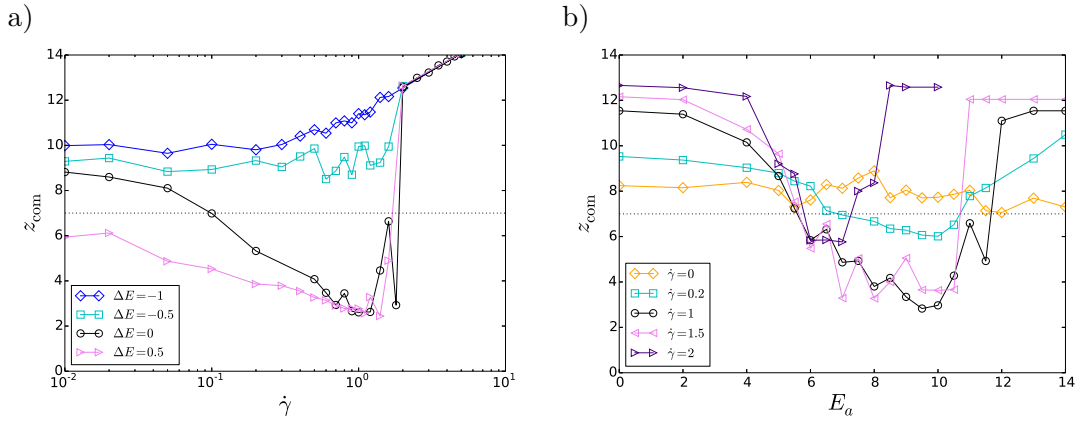

Figure 3.5: a) Average height of the polymer center-of-mass z_{com} as a function of shear rate $\dot{\gamma}$ for a few different values of the adsorption energy $\Delta E = E_d - E_a$ with fixed $E_a = 9$ and $x = 0$. Whereas negative values of ΔE always lead to desorption, for $\Delta E > 0$ the polymer is adsorbed at low shear flow and with increasing shear rate it crosses the desorption transition defined by $z_{\mathrm{com}} = 7$, indicated by the dotted horizontal line. Shear-induced adsorption is observed for $\Delta E = 0$. b) Average height z_{com} as a function of the adsorption energy barrier height E_a for fixed $\Delta E = 0$, $x = 0$ and a few different shear rates.

in the adsorption state diagram in fig. 3.6b as a function of $\dot{\gamma}$ and E_a. For a whole range of adsorption energy barrier heights $5 < E_a < 12$ shear-enhanced adsorption is observed for an interval of intermediate shear rates of about $0.1 < \dot{\gamma} < 2$. As seen in fig. 3.5b, without shear the polymer is desorbed for all values of E_a. The adsorption transition is denoted in fig. 3.6 as black lines. The region shaded in gray indicates where the globule adsorption state depends on the initial conditions of the simulation; at large shear rate and high adsorption energy barrier an initially bound polymer does not desorb during the time of simulation while an initially unbound polymer will stay unbound.

3.3.4 Initial condition and reversibility

The effect of initial conditions and the reversibility of shear-induced adsorption effects are illustrated in fig. 3.7. The average height of the polymer above the surface is shown as a function of the adsorption energy barrier height E_a for fixed $\dot{\gamma} = 1$, $x = 0$, $\Delta E = 0$ in fig. 3.7a, and as a function of shear rate for fixed $E_a = 9$, $x = 0$, $\Delta E = 0$ in fig. 3.7b. We compare two different initialization protocols, for the black data points we start each simulation with a desorbed, unbound globule configuration (which is our general protocol used for most simulations), whereas for the cyan data points we start each simulation with a globule that is bound to the surface via a single, randomly chosen bead. Whereas in fig. 3.7a the adsorption behavior is independent of the initial condition for $E_a < 12$, we see that for larger adsorption energy barriers the behavior is determined by the initial conditions. Likewise, for $\dot{\gamma} < 2$ in fig. 3.7b both simulation protocols lead to identical

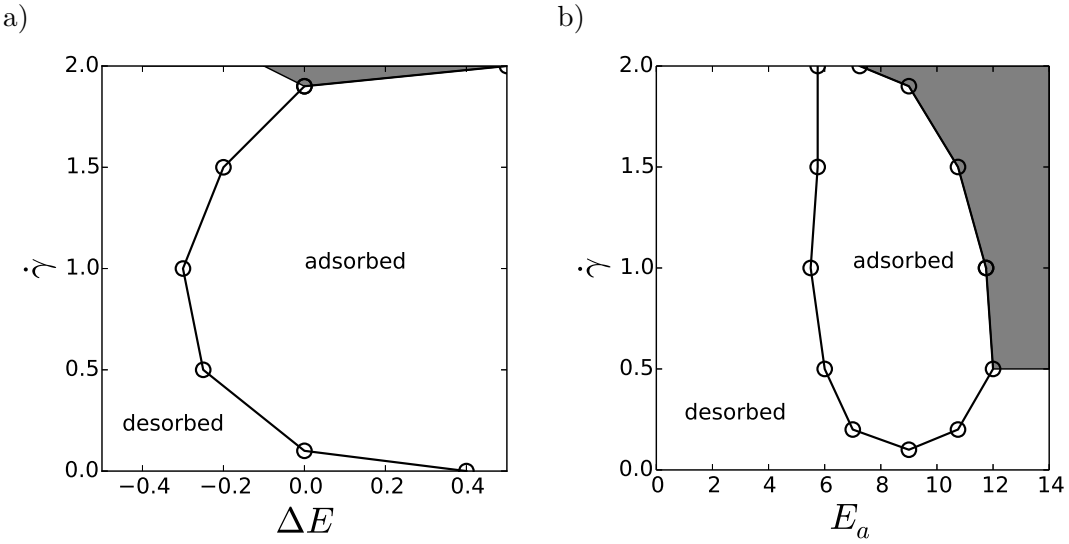

Figure 3.6: a) Adsorption state diagram as a function of shear rate $\dot{\gamma}$ and adsorption energy ΔE at constant adsorption energy barrier height $E_a = 9$ and catch bond parameter $x = 0$. b) Adsorption state diagram as a function of shear rate $\dot{\gamma}$ and adsorption energy barrier height E_a for fixed $\Delta E = 0$ and $x = 0$. In the range $5 < E_a < 12$, shear-induced adsorption is observed for intermediate shear rates. The region shaded in gray, at large E_a and large $\dot{\gamma}$, roughly indicates where the adsorption state depends on the initial conditions. Here, during the course of simulations an initially desorbed globule does not adsorb while an initially adsorbed globule remains adsorbed.

behavior while for larger shear rate an initially adsorbed globule stays adsorbed and an initially desorbed globule stays desorbed during the course of the simulations which consist of up to 10^9 simulation steps. We conclude that a large kinetic barrier separates the adsorbed and desorbed states at high shear rate and for high adsorption energy barriers. In the adsorption state diagrams in fig. 3.6 the region shaded in gray indicates where the adsorption state depends on the initial conditions of the simulation, these are the regions where the system shows irreversible or non-ergodic behavior over the course of the simulations.

The trend towards irreversibility is visualized more explicitly in fig. 3.7c, where we show time series of the instantaneous height $z_{\mathrm{com}}(t)$ and number of surface bonds $N_b(t)/N$ for a few different fixed values of the shear rate. The surface-monomer bond parameters are fixed at $\Delta E = 0$, $E_a = 9$, and $x = 0$ so that the globule exhibits adsorption for shear rates larger than about $\dot{\gamma} = 0.1$, as can be gathered from the adsorption state diagrams in fig. 3.6. Indeed, for a shear rate $\dot{\gamma} = 0.1$ (orange line in fig. 3.7c), which corresponds to the adsorption transition, the globule spends roughly equal amounts of time in the desorbed and in the adsorbed states and frequently switches between the two states. As can be seen in the lower panel of fig. 3.7c, the adsorbed state is maintained by a rather low average number of surface-monomer bonds of about $N_b/N \approx 0.1$. Due to strong

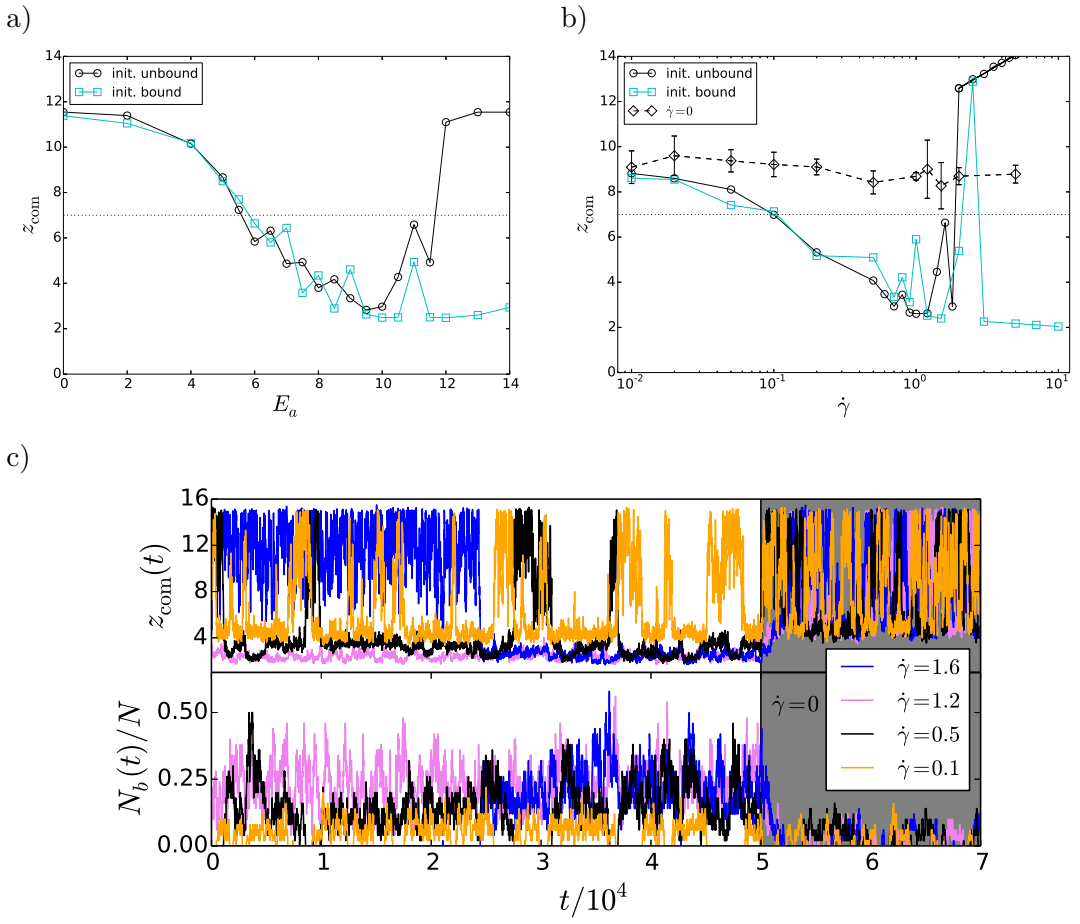

Figure 3.7: Effect of different initial conditions and reversibility of the shear-induced adsorption state for fixed parameters $x = 0$, $\Delta E = 0$. a) Average height $z_{\rm com}$ as a function of the adsorption barrier E_a at fixed $\dot\gamma = 1$. Simulations that start with a desorbed globule (black data points) exhibit shear-induced adsorption for $5 < E_a < 12$. When the globule is initially adsorbed to the surface (cyan data points) and E_a is large, desorption is not observed during the simulation time. b) Similarly, at fixed $E_a = 9$ and varying shear rate $\dot\gamma$, as opposed to simulations starting with a desorbed globule (black solid line), the initially adsorbed globule (cyan) does not desorb at large shear rates. However, the globule reversibly desorbs when the shear flow is suddenly switched off, as indicated by the black dashed line. c) Time series of the instantaneous globule height $z_{\rm com}(t)$ and the number of surface-monomer bonds $N_b(t)/N$ for fixed $E_a = 9$ and different values of the shear rate $\dot\gamma$ as a function of the rescaled simulation time. The initial condition of the simulations is an unbound globule; the globule is adsorbed for all shown shear rates. Within the area shaded in gray, the shear flow is suddenly switched off, $\dot\gamma = 0$, leading to immediate desorption with a low average number of bonds, indicating reversibility with respect to turning off the shear.

hydrodynamic lift forces caused by the shear flow, unbound polymers are most of the time quite far from the surface and outside the adsorption range $z_r = 2$, preventing surface-monomer bond formation. Accordingly, for $\dot{\gamma} = 1.6$ (blue line in fig. 3.7c), the time span to reach the surface when starting from an unbound state is quite large. As can be seen for the data for $\dot{\gamma} = 1.6$, once the globule is adsorbed, more surface-monomer bonds form over time. This cooperative adsorption enhancement in combination with the low dissociation rates, determined by the high desorption energy barrier $E_d = 9$, makes the desorption of the globule a rare event, which explains why the simulations exhibit irreversible behavior for high shear rates.

On the other hand, the shear-induced adsorbed state shows reversibility with respect to switching off the shear flow. This is demonstrated in fig. 3.7c, where within the shaded area the flow is turned off and the shear rate set to $\dot{\gamma} = 0$. We see that shortly after switching off the shear rate, all trajectories exhibit almost immediate desorption characterized by a low average number of bonds. In fact, this type of reversible behavior is observed for all values of the shear rate, as demonstrated in fig. 3.7b, where we plot the average globule height after turning off the shear flow (dashed black line).

3.4 Mapping between stochastic two-state models and conservative potential models

As opposed to the stochastic two-state model for surface-monomer binding used in the present investigation, which exhibits shear-induced globule adsorption for small values of the catch bond parameter x, no shear-enhanced adsorption was found in our previous study that employed a description of surface-monomer binding in terms of conservative pair potentials between surface binding sites and monomers [128]. In this section we investigate whether it is possible to find parameters of a conservative surface-monomer potential that might reproduce the shear-induced adsorption behavior seen in the stochastic two-state surface-monomer binding model. To this end, we devise two different ways of extracting the effective parameters ΔE, E_a and x from a conservative potential-based model for surface-monomer interactions.

3.4.1 Dissociation rate in a one-dimensional corrugated potential

First we consider the one-dimensional motion of a single particle, which represents a monomer, that is pulled by an external force f_{ext} and subject to a corrugated, periodic potential created by a discrete set of Lennard-Jones centers

$$U_{\text{inh}}(y) = \sum_k \varepsilon_W \left(\frac{\sigma_W^{12}}{(\sigma_W + |y - kb|)^{12}} - \frac{2\sigma_W^6}{(\sigma_W + |y - kb|)^6} \right). \tag{3.7}$$

This mimics the potential landscape obtained when decorating a surface with discrete binding sites with distance b, interaction range σ_W and adhesive strength ε_W. Figure 3.8a displays the resulting potential including the effect of the external pulling force,

$$U(y) = U_{\mathrm{inh}}(y) - y f_{\mathrm{ext}} \tag{3.8}$$

for $b = 2$ and two different values of σ_W and ε_W. We study the one-dimensional particle motion using a Brownian Dynamics (BD) simulation scheme. Typical particle trajectories are shown in the inset of fig. 3.8c for $b = 2$, $\sigma_W = 0.5$, $\varepsilon_W = 10$ and two different values of the external force.

We define the desorption rate k_{d} by the inverse average bond lifetime, i.e. the time the particle remains within one potential minimum until it crosses the energy barrier and moves to the next binding site. For simplicity we define a bond to be present when the distance between particle and a binding site is smaller than $b/2$, i.e., the particle is considered always to be bound to the closest surface binding site.

Results from one-dimensional BD simulations in the corrugated potential eq. (3.8) are shown in fig. 3.8c as open symbols, where we plot the desorption rate k_{d} as a function of the external force f_{ext} for the two different potential parameters shown in fig. 3.8a. We remark that the parameter set $\sigma_W = 0.5$ and $\varepsilon_W = 10$ (black squares) yields a globule adsorbed in the stick-roll state at a two-dimensional inhomogeneous surface [128]. Simulation results are in good agreement with the exact calculation of the escape rate $k_{\mathrm{mfpt}} = 1/\tau_{\mathrm{mfpt}}$ (black line), defined as the inverse mean first passage time of a particle escaping from the minimum of the tilted, corrugated potential eq. (3.8). The theoretical result for the mean first passage time [130] to hit either of the two absorbing boundaries at $y = \pm b/2$, starting in the minimum at y_{min} is given by (Appendix A.2)

$$\tau_{\mathrm{mfpt}} = \frac{\int_{-b/2}^{b/2} e^{U(y)} \int_{-b/2}^{y} e^{-U(y')} dy' dy}{\int_{-b/2}^{b/2} e^{U(y)} dy} \int_{-b/2}^{y_{\mathrm{min}}} e^{U(y)} dy - \int_{-b/2}^{y_{\mathrm{min}}} e^{U(y)} \int_{-b/2}^{y} e^{-U(y')} dy' dy. \tag{3.9}$$

For the reduced interaction range $\sigma_W = 0.05$ (simulation results are plotted as gray circles in fig. 3.8c), we increase the adhesive strength to $\varepsilon_W = 11.8$ so that the zero-force desorption rate is the same as for $\sigma_W = 0.05$ with $\varepsilon_W = 10$. Here the simulation time step has to be decreased, from $\Delta t = 10^{-4}$ to 10^{-7}, in order to obtain converged results. We see that simulations and the analytical results (gray line) agree very nicely.

In order to extract rate parameters from the model defined by the potential eq. (3.8), we fit the escape rates according to the desorption rate eq. (3.6) for forces in the range $f_{\mathrm{ext}} < 20$ and using $\nu = 100$. We obtain an effective desorption barrier height $E_d = 10.44$ and a catch bond parameter $x = 0.4$ for the potential parameters $\sigma_W = 0.5$ and $\varepsilon_W = 10$, the fit is illustrated by the dashed cyan line in fig. 3.8c. For the more highly corrugated potential, $\sigma_W = 0.05$ and $\varepsilon_W = 11.8$, we obtain a smaller catch bond parameter $x = 0.2$ but comparable barrier height $E_d = 10.42$; the fit is illustrated by the orange dashed line

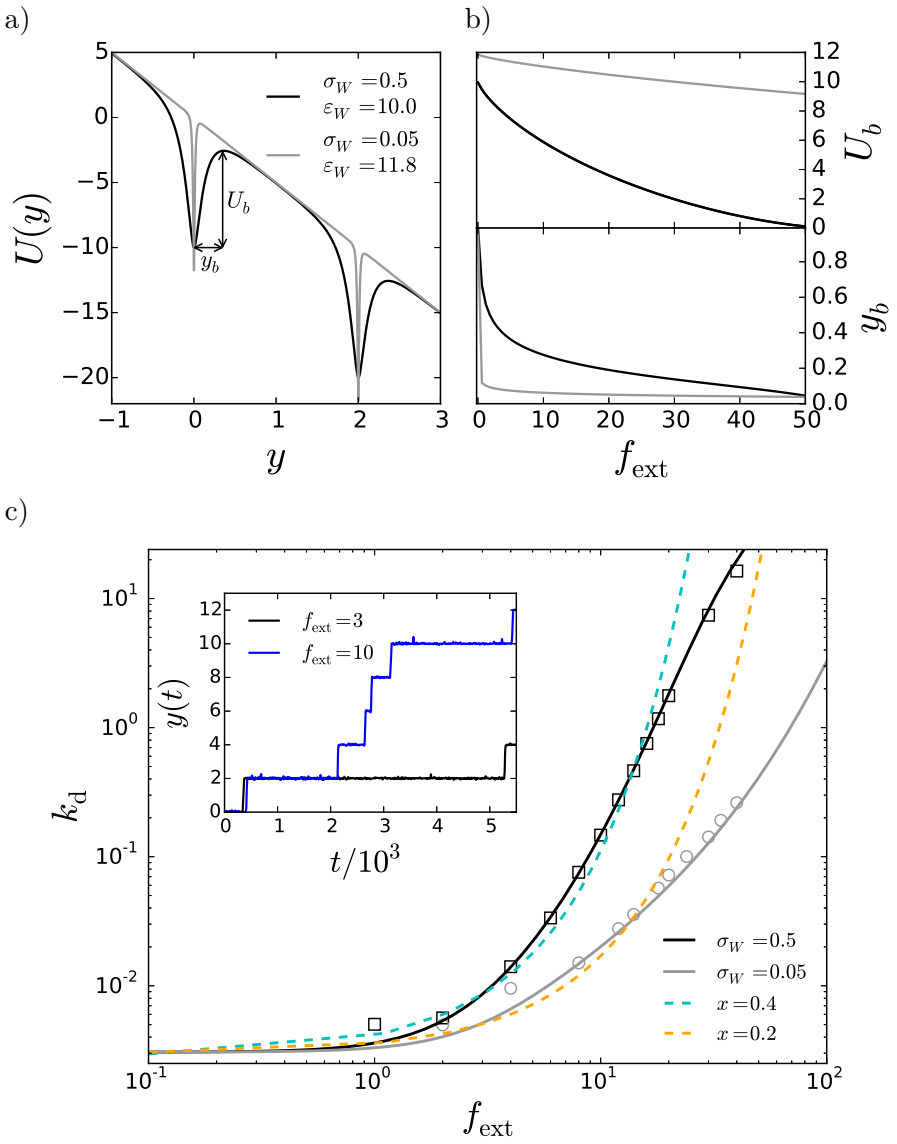

Figure 3.8: a) The one-dimensional potential $U(y)$, eq. (3.8), resulting from the sum over discrete surface binding sites, shown for two different interaction ranges $\sigma_W = 0.5$ (black) and $\sigma_W = 0.05$ (gray) with $\varepsilon_W = 10, 11.8$, respectively, and for pulling force $f_{\rm ext} = 5$. b) With increasing force $f_{\rm ext}$ both the height of the potential energy barrier U_b and its distance to the minimum y_b decrease. c) Desorption rate $k_{\rm d}$ as a function of $f_{\rm ext}$. Results from one-dimensional BD simulations (symbols) are in good agreement with the analytic calculations $k_{\rm mfpt}$ (solid lines) based on the mean first passage time of a particle escaping from the potential minimum, eq. (3.9). Exponential fits (colored dashed lines) according to eq. (3.6) in the range $f_{\rm ext} < 20$ and assuming $\nu = 100$ yield desorption energy barriers $E_d = 10.44, 10.42$ and catch bond parameters $x = 0.4, 0.2$ for $\sigma_W = 0.5$ and $\sigma_W = 0.05$, respectively. The inset shows BD simulation trajectories for two different values of $f_{\rm ext}$ and for $\sigma_W = 0.5$.

in fig. 3.8c. Note that the fits according to the simple exponential force dependence of the desorption rate in eq. (3.6) do not describe the actual data in fig. 3.8c very well. This can be rationalized by the fact that the actual potential energy barrier height U_b and its distance to the minimum y_b, which are both graphically defined in fig. 3.8a, depend sensitively on the applied force f_{ext} and in fact both decrease drastically with increasing f_{ext}, as demonstrated in fig. 3.8b for both potentials plotted in fig. 3.8a. The non-linear decrease of U_b and the force-dependent shift of the barrier height position y_b might explain the deviation of the desorption rate from a simple exponential for large forces, which is clearly seen in fig. 3.8c. In fact, from our fit according to eq. (3.6) we find apparent barrier heights E_d that are comparable to the adhesive strength ε_W in the original potential. By contrast, the fit values for the effective catch bond parameter, which come out as $x = 0.4$ and $x = 0.2$ for the potential interaction ranges $\sigma_W = 0.5$ and $\sigma_W = 0.05$, respectively, are not well correlated with the ranges of the original potentials. In particular, for the potential with the smaller range $\sigma_W = 0.05$, the catch bond parameter is much larger. The reason for this might be that the fit value for the catch bond parameter corresponds effectively to an average over a whole range of the actual barrier position y_b, which is plotted in fig. 3.8b, in the relevant force range $0 < f_{\text{ext}} < 20$. In any case, we see that it might be difficult to reach the necessary small values of the catch bond parameter of the order of $x < 0.02$ needed to observe shear-induced adsorption behavior (see fig. 3.3).

So far we obtained effective values for the catch bond parameter x and the desorption energy barrier E_d. Our simulation results indicate that also the adsorption energy barrier height E_a is a parameter that has to be finely tuned in order to observe shear-induced adsorption (see fig. 3.6b). Since escape rates do not include information about the adsorption energy barrier E_a, a second approach based on the monomer mobility is used next in order to estimate E_a.

3.4.2 Mobility in a one-dimensional corrugated potential

In fig. 3.9 we plot the mobility $\mu = \tilde{\mu}/\mu_0 = V/f_{\text{ext}}$, defined as the ratio of particle velocity V and external force, of a particle in the one-dimensional corrugated potential eq. (3.8) as a function of the external force f_{ext}. Results from one-dimensional BD simulations, identical to the one used in sec. 3.4.1, indicated by open symbols, are in perfect agreement with the corresponding solution of the Fokker-Planck equation [68, 131] (Appendix A.3), indicated by solid lines and given by

$$\mu = \frac{b(1-e^{-bf_{\text{ext}}})}{f_{\text{ext}}} \left(\int_0^b e^{-U(y)} dy \int_0^b e^{U(y')} dy' \right. \\ \left. -(1-e^{-bf_{\text{ext}}}) \int_0^b \int_0^y e^{-U(y)+U(y')} dy' dy \right)^{-1} . \quad (3.10)$$

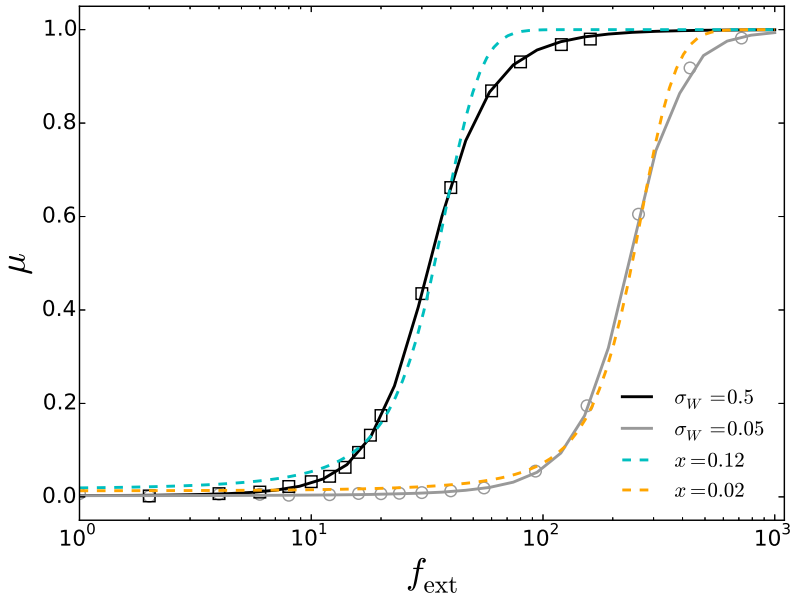

Figure 3.9: Average particle mobility $\mu = V/f_{\text{ext}}$ in the one-dimensional corrugated potential, eq. (3.8), as a function of pulling force f_{ext}. The average velocity V is obtained from one-dimensional BD simulations for $\sigma_W = 0.5$ and $\varepsilon = 10$ (black squares) as well as $\sigma_W = 0.05$ and $\varepsilon = 11.8$ (gray circles). Solid lines represent the solution of the corresponding Fokker-Planck equation, eq. (3.10). Colored dashed lines denote the fits according to a kinetic two-state model, eq. (3.11), with $\Delta E = 4, 4.3$ and $x = 0.12, 0.02$ for $\sigma_W = 0.5, 0.05$, respectively.

To extract desorption and adsorption rates from the data shown in fig. 3.9, we envision the particle motion as a sequence of adsorbed and desorbed states. We assume that the typical adsorption time is t_a, during which the particle is immobile, and that the typical desorption time is t_d, during which the particle moves over a distance d. The rescaled mobility follows as the ratio of the average velocity, $V = d/(t_d + t_a)$, and the velocity in the desorbed state, $V_{\text{d}} = d/t_d$. Furthermore, the desorption time is related to the adsorption rate via $t_d = 1/k_{\text{a}}$ and the adsorption time to the desorption rate via $t_a = 1/k_{\text{d}}$. We obtain for the mobility

$$\mu = \frac{V}{V_{\text{d}}} = \frac{t_d}{t_a + t_d} = \frac{1}{1 + k_{\text{a}}/k_{\text{d}}} = \frac{1}{1 + e^{(\Delta E - xf)}} \tag{3.11}$$

where in the last step we have used eqs. (3.5) and (3.6). Equation (3.11) thus allows to extract the catch bond parameter x and the adsorption energy ΔE from the potential-based model by fit of the mobility. We obtain the fit values $\Delta E = 4$ and $x = 0.12$ for the potential parameters $\sigma_W = 0.5$ and $\varepsilon_W = 10$, and $\Delta E = 4.3$ and $x = 0.02$ for $\sigma_W = 0.05$ and $\varepsilon_W = 11.8$, the corresponding fit functions are shown in fig. 3.9 by dashed lines.

We see that we obtain quite different fit values for the catch bond parameter x based on the desorption rate in sec. 3.4.1 or based on the mobility in the present section. For the

potential parameters $\sigma_W = 0.05$ and $\varepsilon_W = 11.8$ we obtain $x = 0.2$ from the desorption rate and $x = 0.02$ from the mobility. This shows that even a simple surface-monomer potential landscape as in eq. (3.7) cannot be easily and unambiguously cast into a stochastic two-state model. This might be due to the fact that the desorption rate can be fitted to the two-state model reasonably only for small forces $f_{\text{ext}} < 20$, as seen in fig. 3.8c, because the desorption barrier in a realistic potential landscape does not depend in a linear fashion on the applied force, as is assumed in our desorption rate expression eq. (3.6). In contrast, the mobility is fitted well by the two-state model in a much broader range of f_{ext}, as seen in fig. 3.9, here the non-linear force dependence of the desorption barrier height seems to be less important. Alternatively, the reason for the ambiguous fitting results for x could be that also the adsorption barrier exhibits a force dependence, which is neglected in our simple adsorption rate expression in eq. (3.5).

Extracting the desorption barrier height from the desorption rate we obtain for $\sigma_W = 0.05$ and $\varepsilon_W = 11.8$ the value $E_d = 10.42$. This value is comparable to the range where we see shear-induced adsorption in fig. 3.6b. From a fit to the particle mobility we obtain for $\sigma_W = 0.05$ and $\varepsilon_W = 11.8$ the estimate $\Delta E = 4.3$. This value is substantially larger than what is required for shear-induced adsorption, as seen in fig. 3.6a. The effective catch bond parameter we extract for $\sigma_W = 0.05$ and $\varepsilon_W = 11.8$ is either $x = 0.2$ or $x = 0.02$, depending on whether we use the desorption rate or the mobility for the fit. Disregarding the fact that it is not quite clear what the effective catch bond parameter actually is, it seems that even more highly corrugated potential landscapes for the surface-monomer binding would be needed in order to actually reach the effective catch bond parameter range $-0.02 < x < 0.02$ needed for shear-induced adsorption, as seen in fig. 3.3.

In summary, if shear-induced globule adsorption is to be observed using a corrugated surface-monomer potential based on monomer-surface site pair potentials, the potential parameters should be chosen such as to mimic effective rate parameters in the range $E_d = 9$, $\Delta E = 0$ and $-0.02 < x < 0.02$. We argue that it should be possible to reach small effective catch bond parameters x by choosing a very small surface interaction range σ_W, though this will make simulations quite inefficient because of the necessary small time steps. In order to achieve the necessary low ΔE value an additional adsorption barrier might have to be introduced in the potential-based model, such that the effective adsorption barrier E_a becomes similar to E_d and thereby $\Delta E = E_d - E_a$ approaches zero.

3.5 Summary and conclusion

In the present study we investigate the adsorption of a polymeric globule in shear onto a surface with surface-monomer bonds that obey stochastic two-state kinetics. We carefully determine the range of the surface-monomer bond parameters, i.e. the adsorption and desorption energy barriers E_a and E_d as well as the catch bond parameter x, for which shear-induced globule adsorption is obtained. As our main result, we find that in order

to observe shear-induced adsorption, the catch bond parameter x must be finely tuned in a narrow range of $-0.02 < x < 0.02$, while the adsorption and desorption energy barriers must be quite high and set in a range of $5 < E_a, E_d < 12$. Interestingly, the energy barrier difference $\Delta E = E_d - E_a$, which corresponds to the adsorption energy, must be finely tuned in a narrow range of $-0.3 < \Delta E < 0.4$. In other words, the globule must be close to the equilibrium adsorption transition. This corresponds to very stringent conditions on the system parameters and means that biological systems must be finely adjusted in order for flow effects to enhance adsorption of globular structures on surfaces.

The physical picture [7] is that the polymer approaches the surface in a globular conformation in which desorbing lift forces are minimal. Since only few monomers are in the reaction range of the surface, the rather large adsorption energy barrier prevents globule adsorption at low shear. However, when a bond is formed and the shear flow is high enough, the chain is stretched and more bonds can form, given the bond lifetime of the initially formed bond is larger than the globule unfolding time. Our results show that even slip bonds, characterized by a catch bond parameter of the order of $x = 0.01$, can give rise to shear-enhanced globule adsorption.

We show that the shear-induced adsorbed state is reversible with respect to switching off the shear flow, meaning that an adsorbed globule for suitably chosen parameters rapidly desorbs when the shear rate is suddenly set to zero. Similar reversibility has been seen previously in simulations of shear-induced polymer-colloid aggregate formation [132]. At the same time, large shear rates and large desorption energy barriers give rise to severe sampling problems which result in irreversibility effects in the simulations.

In the last part, we attempt a mapping of the kinetic two-state model parameters onto a potential-based binding model. The goal here is to understand the specificities of a surface-monomer pair potential that would be needed in order to lead to shear-induced adsorption of a globule. In a somewhat broader context, the question here is how catch bond behavior results from macromolecules that interact via conservative pair potentials. We perform the mapping using two scenarios, in the first scenario we calculate particle desorption rates, in the second scenario we calculate mobilities of a particle that is dragged over a one-dimensional highly corrugated potential landscape. Catch bond parameters in the range of $x = 0.02 - 0.4$ are obtained, while the adsorption energy difference ΔE turns out to be substantially larger than what is required for shear-enhanced adsorption. This suggests that it might be necessary to add an adsorption barrier into the surface monomer interaction potential. We conclude that it is not straightforward to design a model based on conservative surface-monomer pair potentials that would lead to shear-induced adsorption behavior. On the other hand, the short-comings of our mapping also show that the description of surface-monomer interactions using a kinetic two-state model with only three parameters is incomplete and an additional parameter reflecting the force-dependence of the adsorption rate might be needed.

The interesting question remains of how catch bond behavior can be reproduced by models based on pair potentials. Clearly, the force dependence of the stability of a

potential-based bond depends on the potential shape in a non-trivial fashion, and it is altogether not clear what a minimal model to obtain effective catch bond behavior is. It might be possible to induce catch bond character of a bond by introducing saturation and shielding effects, which would involve the interplay of several binding sites.

Chapter 4

Internal tension in a collapsed polymer under shear flow and the connection to enzymatic cleavage of von Willebrand factor

4.1 Introduction

The study of the dynamics of polymers in solution has become an important aspect for understanding non-equilibrium processes in biopolymeric systems. In the context of blood coagulation, considerable research has been focused on the multimeric glycoprotein von Willebrand factor (VWF). The binding of VWF to exposed collagen at sites of vascular injuries and the simultaneous VWF-mediated adhesion of platelets are central steps in primary hemostasis [11, 27, 133]. In this context, the presence of shear or elongational flow constitutes a crucial ingredient as it activates the functional conformation of VWF multimers by inducing a transition from globular to unfolded conformations [54, 58, 61] and thus facilitates adhesion to the extracellular matrix [31, 134]. Previous simulation studies elucidated the dynamics and the VWF adsorption behavior [31, 128] and revealed that VWF must exhibit finely adjusted, long-lived bonds in order to resist hydrodynamic forces and to allow for shear-induced adhesion [76, 135].

The existence of shear, apart from inducing conformational changes of the VWF multimers, can presumably also influence VWF's function by changing the tertiary structure of individual monomers. In particular, it has been argued that tensile forces lead to the unfolding of individual domains [19, 136] and consequent exposure of binding and cleavage sites that in equilibrium conditions or at low shear rates are not accessible, e.g. due to shielding effects of VWF domains [137, 138].

Another shear-induced biological process in which VWF takes part is the reversible platelet aggregation under high shear rate [8, 132, 139, 140] that has pathophysiological relevance. In fact, malfunction in the VWF degradation and the resulting high amount of abnormally long VWF multimers can lead to life-threatening thrombotic diseases [23, 141]. The shear-dependent VWF degradation thus presents an active area of research [16]. The required regulatory mechanism is associated with the specific metalloprotease ADAMTS13, which

is responsible for VWF length regulation and thereby controls the hemostatic activity [11, 142]. Note that the length distribution of VWF in plasma has been determined recently using fluorescence correlation spectroscopy (FCS) [20]. The cleavage site at which ADAMTS13 acts is deeply buried within the VWF A2 domain in the native state [143]. There is general consensus that VWF degradation requires shear or force-induced A2 domain opening and exposure of the cleavage site for ADAMTS13 [18, 19, 144, 145]. The force-induced activation of single A2 domains was recently studied using laser tweezers [136]. In that study, cleavage of unfolded A2 domains was observed and the dependence of the catalytic rate on the enzyme concentration was determined. Details about the underlying molecular mechanism were provided by means of molecular dynamics simulations [19].

In the present study we address the interplay between shear-flow-induced VWF unfolding and the internal tensile force distribution along the polymer contour, the opening of the mechanosensitive VWF A2 domain and the activity of the cleavage enzyme ADAMTS13. We use a coarse-grained VWF polymer model and employ Brownian hydrodynamics simulations. In the first part, we show that the shear-induced unfolding transition of a collapsed globule, where elongated configurations are periodically observed for short time intervals, can be connected to an inhomogeneous profile of the average tension between monomers along the polymer chain. The unfolding has previously been explained by a nucleation model based on the existence of thermally activated polymeric protrusions [58]. Here, we present a direct proof of the existence of such protrusions and corroborate the protrusion-induced instability mechanism leading to unfolding of collapsed polymers in shear flow. We study the tension profile as a function of shear rate, chain length, and cohesive strength. The average maximal force (the peak force) along the chain contour is identified as the typical force acting on a protrusion. We determine scaling relations for the dependence of the peak force and the average protrusion length on the size of the globule and its cohesive strength. Using these scaling predictions, we develop a quasi-equilibrium theory to describe the average length of protrusions.

In the second part we show how the shear-induced tension profile along the polymer is connected to the physiological process of shear-dependent proteolysis of VWF by its specific cleavage enzyme ADAMTS13. We formulate a simple stochastic two-state model for the VWF A2 domain opening and calculate the force-dependent probability for the domain to be accessible to cleavage by ADAMTS13 from the tension distribution along our coarse-grained polymer model of VWF. The result can be connected to the shear-dependent cleavage rate of full-length VWF mediated by ADAMTS13 that has been recently measured experimentally by Lippok et al. [146]. In that study, fluorescence correlation spectroscopy (FCS) was employed in combination with a microfluidic shear cell to quantify the effect of shear on the kinetics of VWF cleavage in aqueous buffer and in blood plasma by measuring the time-dependent increase in VWF multimer concentration. Our theoretical modeling allows to deduce characteristic parameters of single cleavage sites like the effective force scales of the stochastic opening and closing processes. We compare our results with laser tweezer experiments [136] on single A2 domains and argue

that the domain opening in shear flow might not be equivalent to the domain unfolding probed by external stretching forces.

4.2 Simulation method

Brownian hydrodynamics simulations are performed using the discretized Langevin equation

$$\mathbf{r}_i(t+\Delta t) - \mathbf{r}_i(t) = \left(\boldsymbol{\mu}_{ii}\dot{\gamma} z_i \hat{\mathbf{x}} - \sum_{j=1}^{N} \boldsymbol{\mu}_{ij} \cdot \nabla_{\mathbf{r}_j} U(t) \right) \Delta t + \boldsymbol{\xi}_i(\Delta t), \tag{4.1}$$

which describes the displacement of bead i at position $\mathbf{r}_i$ after the time step Δt. Note that all quantities used are made dimensionless by rescaling lengths $r = \tilde{r}/a$ by the bead radius a, energies $U = \tilde{U}/\mathrm{kT}$ by thermal energy and times $t = \tilde{t}/\tau$ by the characteristic monomer diffusion time $\tau = a^2/\mu_0 \mathrm{kT} = 6\pi\eta a^3/\mathrm{kT}$, where η is the viscosity. The first term in eq. (4.1) represents a linear shear flow with rate $\dot{\gamma} = \tilde{\dot{\gamma}}\tau$, where $\hat{\mathbf{x}}$ is the unit vector in x-direction. The second term accounts for the direct force acting on particle i itself as well as the hydrodynamic flow-field created by forces acting on all other particles $j \neq i$. Hydrodynamic interactions are taken into account via the mobility matrix approximated by the Rotne-Prager-Yamakawa tensor [118, 119]

$$\boldsymbol{\mu}_{ij} = \tilde{\boldsymbol{\mu}}_{ij}/\mu_0 = \begin{cases} \frac{3}{4r_{ij}} \left(\left(1 + \frac{2}{3r_{ij}^2} \right) \mathbf{1} + \left(1 - \frac{2}{r_{ij}^2} \right) \frac{\mathbf{r}_{ij}\mathbf{r}_{ij}}{r_{ij}^2} \right) & r_{ij} \geq 2 \\ \left(1 - \frac{9r_{ij}}{32} \right) \mathbf{1} + \frac{3r_{ij}}{32} \frac{\mathbf{r}_{ij}\mathbf{r}_{ij}}{r_{ij}^2} & r_{ij} < 2 \end{cases}, \tag{4.2}$$

where $\mathbf{r}_{ij} = \mathbf{r}_i - \mathbf{r}_j$ and $r_{ij} = |\mathbf{r}_{ij}|$; selfmobilities are given by $\boldsymbol{\mu}_{ii} = \tilde{\boldsymbol{\mu}}_{ii}/\mu_0 = \mathbf{1}$. For free draining simulations the off-diagonal elements of the mobility matrix eq. (4.2) are set to zero. The stochastic contribution $\boldsymbol{\xi}_i$ is given by Gaussian random vectors with correlations according to the fluctuation-dissipation theorem $\left\langle \boldsymbol{\xi}_i \boldsymbol{\xi}_j \right\rangle = 2\boldsymbol{\mu}_{ij}\Delta t$ and vanishing mean. The simulation typically runs for 10^8 time steps of length $\Delta t = 5 \times 10^{-4}$.

The homopolymer model consists of N beads, which interact via Lennard-Jones potentials of depth $\varepsilon = \tilde{\varepsilon}/\mathrm{kT}$ and are connected in a linear chain by stiff bonds with a rescaled spring constant $\kappa = \tilde{\kappa}a^2/\mathrm{kT} = 200$; the total potential reads

$$U = \varepsilon \sum_{i<j} \left((2/r_{ij})^{12} - 2\,(2/r_{ij})^{6} \right) + \frac{\kappa}{2} \sum_i \left(r_{i,i+1} - 2 \right)^2 . \tag{4.3}$$

In order to obtain a measure for the absolute value of the tensile force $f_i \equiv \langle f_i \rangle = \kappa(\langle r_{i,i+1} \rangle - 2)$ along the bond between beads i and $i+1$, the average distance $\langle r_{i,i+1} \rangle$ is recorded during the course of simulation using block averages of a time interval $t = 0.05$.

4.3 Results for tensile force profiles

We consider a collapsed polymer of length $N = 50$ having fixed cohesive strength $\varepsilon = 2$, unless stated otherwise. The influence of an applied shear flow on the size of the globule is shown in fig. 4.1a. The squared radius of gyration $R_g^2 = N^{-1} \sum_i (\mathbf{r}_i - \mathbf{r}_{\mathrm{com}})^2$, with $\mathbf{r}_{\mathrm{com}} = N^{-1} \sum_i \mathbf{r}_i$, monotonically increases as a function of shear rate $\dot{\gamma}$, where we subtract $(R_g^0)^2 = R_g^2(\dot{\gamma} = 0) = 11.3$, the globule radius of gyration measured at vanishing shear $\dot{\gamma} = 0$. The black line indicates a scaling relation $R_g^2 - (R_g^0)^2 \sim \dot{\gamma}^2$ for not too large shear rates $\dot{\gamma} < 40$.

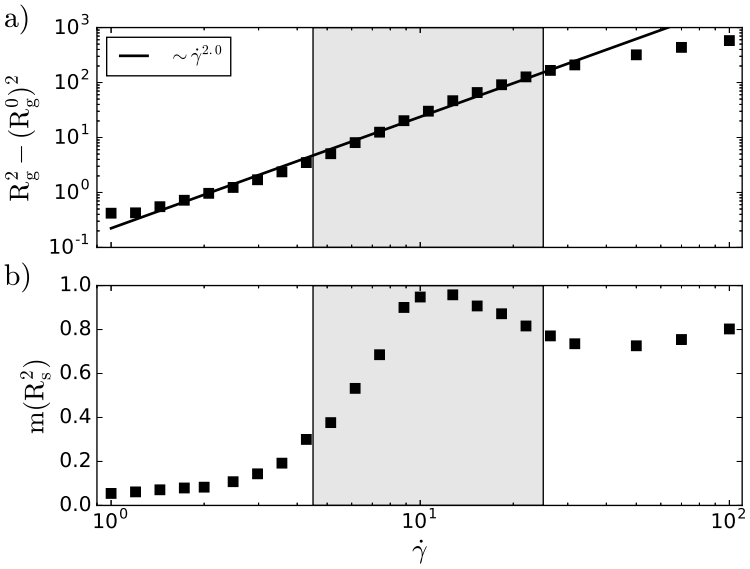

Figure 4.1: a) Squared radius of gyration R_g^2 as a function of shear rate $\dot{\gamma}$ for cohesive strength $\varepsilon = 2$ and $N = 50$; hydrodynamic interactions are included. The equilibrium value $(R_g^0)^2 = 11.3$ is subtracted. The solid line represents a power law with exponent 2. b) The rescaled variance of the squared extension $m(R_S^2)$ displays a maximum at about $\dot{\gamma}^* = 10$ corresponding to the critical shear rate of globule unfolding. The area shaded in gray indicates where the force profiles in fig. 4.2a exhibit a double-peak structure.

The conformational change of a polymeric globule in shear flow has been investigated in previous studies [58, 61] reporting a quite sharp unfolding transition at a critical shear rate $\dot{\gamma}^*$ at which large size fluctuations are observed. In those studies, the shear-induced unfolding transition is defined by the maximum of the rescaled variance of the squared extension $m(R_S^2)$, displayed in fig. 4.1b. The extension R_S is defined as the maximal distance in flow direction between any two beads from which the rescaled variance follows as $m(R_S^2) = \left(\langle R_S^4 \rangle - \langle R_S^2 \rangle^2\right) / \langle R_S^2 \rangle^2$. We obtain for $N = 50$ and $\varepsilon = 2$ the critical shear rate $\dot{\gamma}^* = 10$, in agreement with previous results [61] where it has been shown that the critical shear rate depends on the chain length N. Note that the squared radius of

gyration exhibits similar fluctuations and its variance could also be used to define the unfolding transition.

We next investigate the tension profile along the contour of a collapsed polymer subject to shear flow and present results for the tensile force f_i as a function of bead position i in fig. 4.2a for a few different shear rates. The polymer remains strongly collapsed for low shear rates $\dot{\gamma} < 5$, as can be gathered from the small radius of gyration, fig. 4.1a, and the small extensional fluctuations, fig. 4.1b. In such a globular conformation, as illustrated by the top snapshot in fig. 4.2e, tensile forces only stem from thermal fluctuations and are rather small and maximal at the termini. With increasing shear rate the maximal tensile force shifts away from the chain termini and a double-peak structure appears in the tensile force profile, a transition taking place around $\dot{\gamma} = 5$. We define the transition to be at the shear rate where the maxima move away from the chain termini. Notice that this is below the critical shear rate of unfolding, $\dot{\gamma}^* = 10$, defined by the maximum variance of the extension, fig. 4.1b. The double-peak structure is also observed for shear rates well above the unfolding transition, until the force profile changes around $\dot{\gamma} = 30$ to a profile with a flat maximum in the middle and with strongly decreasing tension towards the termini. Fluctuations around the average forces f_i are substantial, as indicated by the standard deviation defined by $\sigma_i^2 \equiv \sigma^2(f_i) = \langle f_i^2 \rangle - \langle f_i \rangle^2$ and shown for $N = 50$ and different shear rates in fig. 4.2b. Corresponding broad normalized probability distributions $P(f_{25})$ for the middle bead $i = 25$ are shown in fig. 4.2c. Force profiles for different chain lengths are presented in fig. 4.2d for a fixed shear rate $\dot{\gamma} = 10$. We observe the double-peak structure only for long chains, $N \geq 20$. The tension for short chains at high shear are maximal in the middle and resemble inverted parabolas.

We attribute the peaks in the tensile force profiles close to the termini of the polymer to polymeric protrusions of length l_p, one of which is illustrated by the middle snapshot in fig. 4.2e. The reason for the existence of a force peak is that the hydrodynamic drag force acting on a protrusion is larger compared to monomers within the globule, which is due to hydrodynamic shielding effects. In addition, the occurrence of the double-peak structure in the force profiles is closely related to the shear-induced unfolding transition that has been rationalized by a nucleation theory based on the presence of thermally excited polymeric protrusions [61]. The area shaded in gray in fig. 4.1 indicates the range $4 < \dot{\gamma} < 30$ where the double-peak structure in the tensile force profile appears. In the same range the variance of the squared extension $m(R_S^2)$ displays a maximum, fig. 4.1b, which is used to define the unfolding transition. In fact, the unfolding transition leads to cyclic elongation, illustrated by the bottom snapshot in fig. 4.2e, tumbling, and refolding, causing a large variance of the average extension. As the double-peak structure is only observed for long chains, $N \geq 20$, as seen in fig. 4.2d, we conclude that chains have to be long enough so that a globule can form and the protrusion mechanism for unfolding becomes operational.

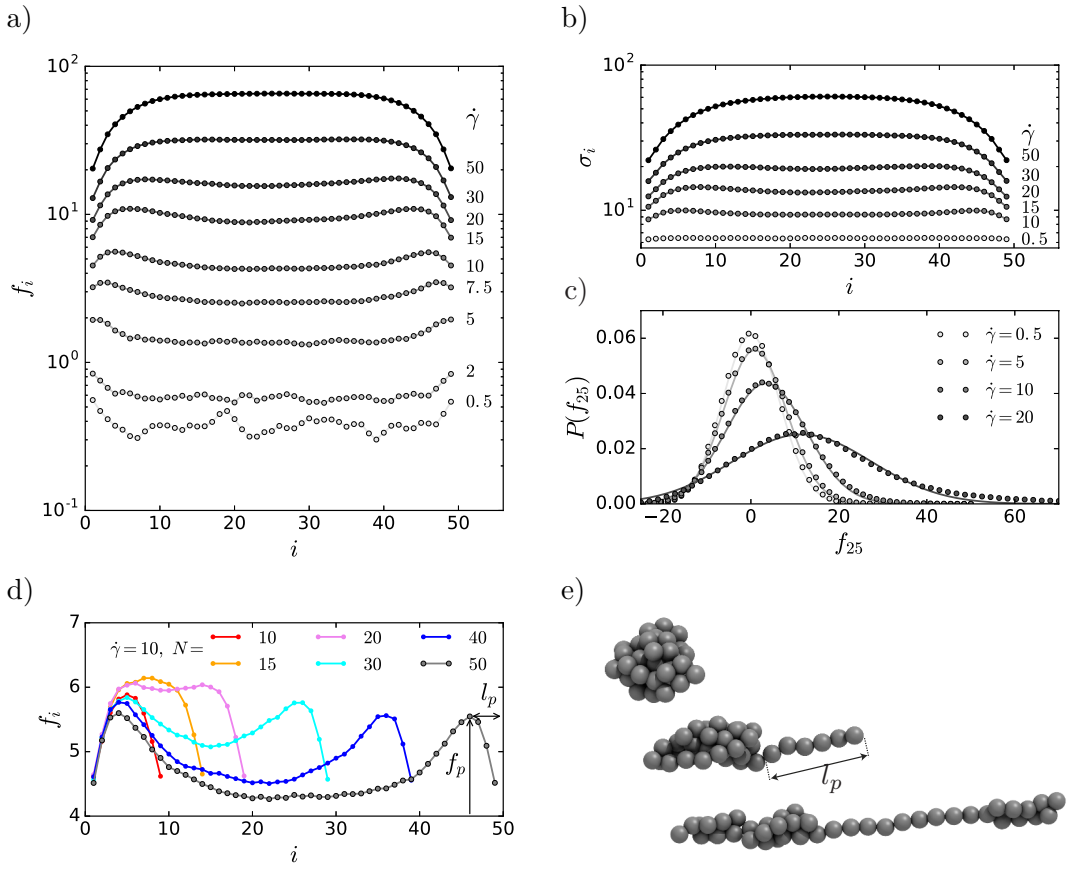

Figure 4.2: a) Average tensile force f_i as a function of bead position i along a collapsed polymer with cohesive strength $\varepsilon = 2$ and $N = 50$. For increasing shear rate $\dot\gamma$ the overall tension increases and the profile changes at about $\dot\gamma = 5$ from exhibiting maximal tensile forces at the termini to a double-peak structure, which disappears for larger $\dot\gamma \geq 30$. b) The standard deviation $\sigma(f_i)$ as a function of i shown for different $\dot\gamma$ indicates large fluctuations. c) This is reflected in the broad normalized probability distribution $P(f_{25})$ of the middle bead $i = 25$ (symbols) that can be well fitted with a Gaussian (lines). d) Tension profiles for different chain length N for fixed shear rate $\dot\gamma = 10$. Black arrows illustrate the definition of the average protrusion length l_p and the peak force f_p for $N = 50$. e) Snapshots of a collapsed globule, a globule having a protrusion of length l_p, and an elongated configuration (from top to bottom), all taken from simulations for $\varepsilon = 2$, $N = 50$ and $\dot\gamma = 10$.

4.3.1 Analysis

In order to analyze the double-peak structure of the tensile force profiles figs. 4.2a,d in more detail, we define two characteristic quantities. First, the peak tensile force f_p, defined as the maximal average tension along the chain, which is associated with the average hydrodynamic drag force acting on protrusions. Second, the average protrusion length l_p, defined as the monomer distance of the force peak from the adjacent chain end. The definition of the peak force f_p and the protrusion length l_p are illustrated by arrows in fig. 4.2d for the right peak of the force profile for $N = 50$. The length of a protrusion is also illustrated by the middle snapshot in fig. 4.2e. Since the tension profiles are symmetric with respect to the center of the polymer chain we consider the mean of the two peaks in order to determine f_p and l_p.

4.3.1.1 Protrusion length and peak force at fixed cohesion and globule size

In fig. 4.3 we present the average protrusion length l_p and the average peak tensile force f_p as a function of shear rate. As before, we consider a globule with cohesion $\varepsilon = 2$ and $N = 50$ monomers. Hydrodynamic interactions (HI) are either taken into account (filled symbols) or are neglected (FD, open symbols). In the FD case, no double-peak structure is observed and with increasing shear rate the position l_p of the peak force abruptly changes from the polymer termini to the middle. Note that this jump occurs around the critical shear rate of unfolding, which is at $\dot{\gamma}^* = 1$ for the FD case [61]. For the HI case, the area shaded in gray in fig. 4.3 indicates the range $4 < \dot{\gamma} < 30$ where the double-peak structure appears. The protrusion length, fig. 4.3a, increases monotonically with shear rate according to the heuristic scaling law $l_p \sim \dot{\gamma}^{1.2}$ until the profile exhibits a single central peak at large shear rates. We observe protrusion lengths in the range $1 < l_p < 10$. Note that due to our discrete bead-spring model, we cannot determine arbitrarily short protrusions. When there is no protrusion and the maximal force is located at the chain termini, the smallest value is defined to be $l_p = 1$. The data in fig. 4.3 is fitted only within the shaded area where double peaks are observed. The maximal forces, shown in fig. 4.3b, follow the scaling $f_p \sim \dot{\gamma}^{1.6}$ for large shear rates. For comparison we also plot the mean tension along the chain, $f_{\text{mean}} = N^{-1} \sum_i f_i$ for varying shear rate, which shows a similar behavior as the peak force, $f_{\text{mean}} \sim \dot{\gamma}^{1.8}$. Note that the tensile force of a dimer increases linearly with shear rate as shown in the Appendix A.5.

4.3.1.2 Dependence on globule size and cohesive strength

The hydrodynamic drag force acting on a protrusion could depend besides the protrusion length l_p also on the globule radius $R \sim N^{1/3}$. In fact, the double-peak structure strongly depends on the chain length N, as indicated by the force profiles in fig. 4.2d. Another influential parameter is the cohesive strength ε of the globule, which determines the restoring force on the protrusions. In the following we investigate the effect of different

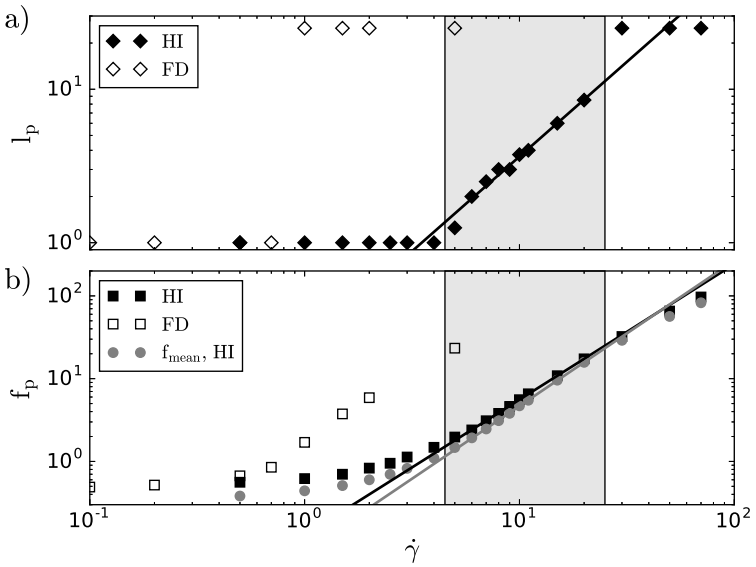

Figure 4.3: A globular polymer with $N = 50$ and $\varepsilon = 2$ exhibits a double-peak structure only in the presence of hydrodynamic interactions (HI, filled symbols), the corresponding range of the shear rates $\dot{\gamma}$ is shaded in gray. a) The mean protrusion length l_p as a function of $\dot{\gamma}$. In the free draining case (FD, open symbols) there is an abrupt jump around $\dot{\gamma} = 1$ from the chain end to $l_p = 25$ above which the maximal force is located in the middle of the chain. In the HI case the protrusion length increases according to $l_p \sim \dot{\gamma}^{1.2}$ (line) until there is only a single middle peak at large shear rates. b) The peak force f_p, defined as the maximum average tension along the polymer contour, scales as a function of shear rate like $f_p \sim \dot{\gamma}^{1.6}$, obtained by a fit of the data (black line) within the shaded area. Also the mean tension along the chain f_{mean} (gray discs) is shown for the HI case which exhibits a similar scaling $f_{\mathrm{mean}} \sim \dot{\gamma}^{1.8}$ (gray line).

globule sizes and varying cohesive strength. We focus on the HI case, since no double-peak structure is observed in free draining simulations.

Results for the peak forces f_p and the mean forces f_{mean} as a function of N are plotted in fig.4.4a for fixed cohesive strength $\varepsilon = 2$ and shear rate $\dot{\gamma} = 10$. The peak force only weakly depends on the globule size; it decreases almost linearly with increasing chain length. The mean tensile force along the chain decreases more strongly with increasing N and can be described by a power law $f_{\mathrm{mean}} \sim N^{-1/3} \sim R^{-1}$, shown by the solid gray line. The average protrusion length l_p, shown in fig.4.4b, also decreases as the inverse of the radius $l_p \sim N^{-1/3} \sim R^{-1}$, shown by the solid black line.

The dependence on the cohesive strength ε is shown in fig. 4.4c,d. A double-peak structure in the tension profile is only observed for values $0.7 < \varepsilon < 3$. The lower boundary is determined by the collapse transition that occurs for $N = 50$ at $\varepsilon_{\mathrm{col}} \approx 0.66$ [61], hence for lower values $\varepsilon < \varepsilon_{\mathrm{col}}$ the polymer is in a coiled state where maximal forces occur in the chain middle. A higher cohesive strength $\varepsilon \approx 3$ leads to a compact, almost frozen

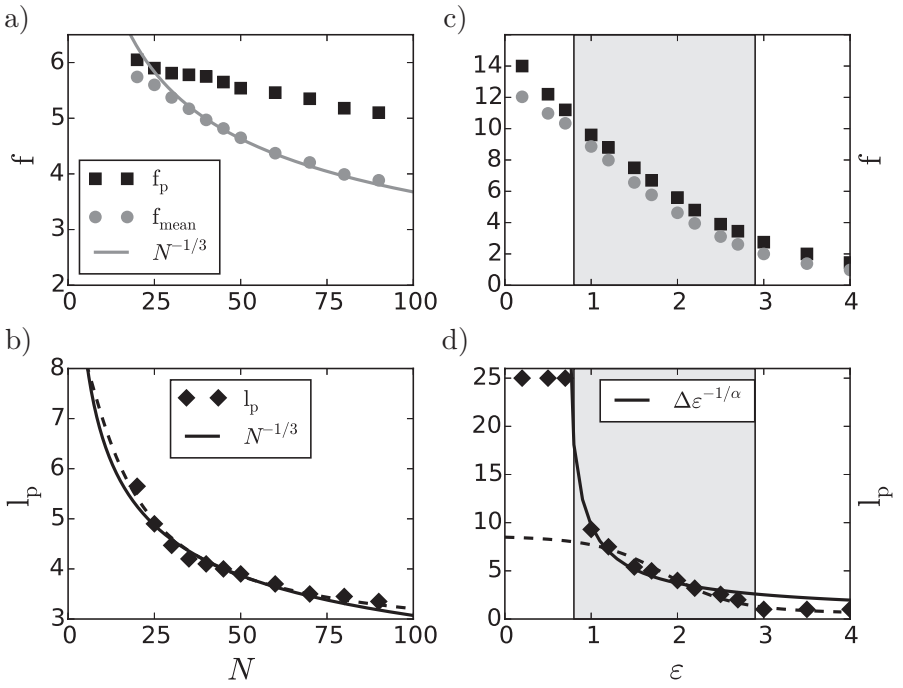

Figure 4.4: a) Peak forces f_p, mean tension f_{mean}, and b) protrusion length l_p as a function of globule size N for fixed cohesive strength $\varepsilon = 2$ and shear rate $\dot{\gamma} = 10$. Solid lines indicate a scaling with the inverse radius of gyration $f, l_p \sim N^{-1/3} \sim R^{-1}$. The peak force in a) decreases rather linearly with increasing globule size. The protrusion length in b) can be described in terms of a quasi-equilibrium theory by eq. (4.8) with fit parameters $\zeta_{\mathrm{hyd}} = 2.2 \times 10^{-4}, \zeta_{\mathrm{coh}} = 0.33$ (dashed line). c,d) Results for fixed globule size $N = 50$ and shear rate $\dot{\gamma} = 10$ at varying cohesive strength ε. A double-peak structure is only observed for $0.7 < \varepsilon < 3$ (shaded region) between the collapse transition at low cohesion and the freezing transition at high cohesion where no protrusions are observable. The tension decreases approximately linearly with increasing ε. The dashed line in d) is the theoretical result eq. (4.8) with $\zeta_{\mathrm{hyd}} = 3.7 \times 10^{-4}, \zeta_{\mathrm{coh}} = 0.37$. Fitting the function eq. (4.10) yields the exponent $\alpha = 1.4$ (solid line).

globule which does not allow for protrusions. Both the peak force as well as the mean force decrease approximately linearly with increasing cohesive strength, as can be seen in fig. 4.4c. The protrusion length shown in fig. 4.4d can be fitted within the shaded area by a power law $l_p \sim \Delta\varepsilon^{-1/\alpha}$, shown by a solid line, where we introduce the energy difference $\Delta\varepsilon = \varepsilon - \varepsilon_{\mathrm{col}}$ and obtain the exponent $\alpha = 1.4$. Note that this scaling behavior can be obtained by a quasi-equilibrium model and using the assumption that the average protrusion length is independent of the shear rate, as discussed in the next section. This approach yields an estimate for the exponent α that characterizes the restoring cohesive force on a protrusion defined via eq. (4.6).

4.3.1.3 Quasi-equilibrium theory

A previous study [61] established the scaling behavior for the hydrodynamic drag force and the restoring cohesive force on a protrusion in order to estimate the critical shear rate at which shear-induced globule unfolding sets in. It was argued that when the two opposing forces balance, there is an instability and the globule can fully elongate since no energy barrier prevents the protrusion to be dragged out from the globule. For a collapsed globule the unfolding time is presumably much larger than the inverse shear rate, i.e. the period of globule rotation. As a consequence, most protrusions are short-lived and are wrapped around the globule by the constant rotation rather than leading to full elongation of the polymer. Therefore a nucleation model is well suited to make scaling predictions for the transition from the collapsed to an unfolded state which is much slower compared to the fast shear-induced refolding. This might be the reason why protrusion are absent in the FD case, where little hydrodynamic resistance against shear-induced deformations leads to fast unfolding at relatively low shear rates.

In contrast to these nucleation-type arguments, here we make use of the scaling behavior of drag force and cohesive force and apply a quasi-equilibrium theory in order to estimate average values for the protrusion length l_p and the tensile force f_p. Our quasi-equilibrium theory does not describe the rare events of full unfolding around the critical shear rate but yields information about the average protrusions which can be compared to our tensile force profiles.

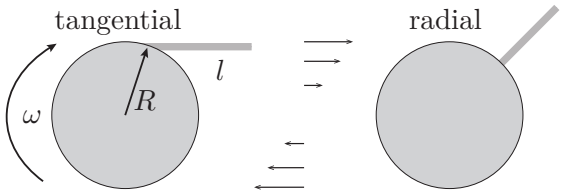

Figure 4.5: Schematic illustration of a tangential and a radial protrusion of length l. The spherical globule with radius R is rotating in shear flow with angular velocity ω.

As schematically depicted in fig. 4.5, we consider a polymer segment of length l protruding from a collapsed spherical globule with radius R, which is rotating in shear flow with angular velocity $\omega = \dot{\gamma}/2$. In principle we would have to take into account all possible configurations of protrusions, however, we focus on the cases where the largest drag force occurs. Two typical cases are shown fig. 4.5: for a tangential protrusion the drag force is maximal at the top of the globule (left), while the force on a radial protrusion is maximal at an angular position of $\pi/4$ with respect to the flow direction [61].

In the presence of hydrodynamic interactions, the drag force results from an integral along the protrusion contour, $f_{\mathrm{hyd}} = \int_0^l (\mathbf{v} - \mathbf{v}_0)\, d\mathbf{l}$, for this we use the analytical flow

profile around a sphere in linear shear [147],

$$v_\beta = \dot{\gamma} z \delta_{\beta x} + \frac{\dot{\gamma} R}{2} \left(\frac{5\left(1-(r/R)^2\right)\beta x z}{R^3 (r/R)^7} - \frac{\delta_{\beta z} x + \delta_{\beta x} z}{R (r/R)^5} \right) \tag{4.4}$$

with $\beta \in \{x, y, z\}$. We define the reference velocity $\mathbf{v}_0$ at the surface of the globule from where the protrusion emerges. Expansion for short length $l < R$ of the velocity profile eq. (4.4) leads to a radial velocity $v \sim \dot{\gamma} l^2 / R$ [61] and hence to

$$f_{\mathrm{hyd}} \sim \dot{\gamma} l^3 / R. \tag{4.5}$$

Using the tangential configuration of the protrusion only changes the prefactor but leaves the scaling behavior unchanged.

The restoring cohesive force is assumed to scale as

$$f_{\mathrm{coh}} \sim -\Delta\varepsilon \, l^{\alpha-1}, \tag{4.6}$$

where $\Delta\varepsilon = \varepsilon - \varepsilon_{col}$, i.e. the cohesive strength relative to the cohesion at the collapse transition. The linear behavior of the force with respect to the cohesive strength is reflected in our simulation data, as shown in fig. 4.4c. The parameter value $\alpha = 1$ describes protrusions much longer than the globule-solvent interfacial width and which experience a constant cohesive force that does not depend on the length l. For short protrusions the harmonic approximation is expected, $\alpha = 2$ [61].

In order to calculate the average protrusion length l_p, we construct the energy expression for a protrusion

$$U_{\mathrm{tot}} = U_{\mathrm{hyd}} + U_{\mathrm{coh}} = -\zeta_{\mathrm{hyd}} \, \dot{\gamma} l^4 / R + \zeta_{\mathrm{coh}} \, \Delta\epsilon l^\alpha, \tag{4.7}$$

where the potential of mean force associated with the cohesion is determined by $\partial U_{\mathrm{coh}} / \partial l = -f_{\mathrm{coh}}$ and the contribution that pulls the protrusion out of the globule is given by $\partial U_{\mathrm{hyd}} / \partial l = -f_{\mathrm{hyd}}$. The prefactors ζ_{hyd} and ζ_{coh} are used to fit the data. We next assume that the protrusion configuration relaxes relatively quickly and can be described by an equilibrium Boltzmann distribution. Numerical evaluation of the Boltzmann average yields the average protrusion length

$$l_p = \frac{\int_0^{l_{\max}} e^{-U_{\mathrm{tot}}(l)} \, l \, dl}{\int_0^{l_{\max}} e^{-U_{\mathrm{tot}}(l)} dl}, \tag{4.8}$$

where the integration boundary $l_{\max}$, the maximal protrusion length, is a further parameter that is used to fit the simulation data. Similarly, an estimate for the average peak force is given by

$$f_p = \frac{\int_0^{l_{\max}} e^{-U_{\mathrm{tot}}(l)} \left| \frac{\partial U_{\mathrm{tot}}}{\partial l} \right| dl}{\int_0^{l_{\max}} e^{-U_{\mathrm{tot}}(l)} dl}. \tag{4.9}$$

In the limit of vanishing shear rate or large globules, or under the assumption that the average protrusion length is independent of the shear rate, we can neglect the first term

in eq. (4.7) and calculate the average protrusion length via eq. (4.8) for $l_{\max} \to \infty$, which yields

$$l_p \sim \Delta\varepsilon^{-1/\alpha}. \tag{4.10}$$

The dashed lines in fig. 4.4b and fig. 4.4d represent the equilibrium result eq. (4.8) for the protrusion length as function of chain length N and as a function of the cohesive strength ε, respectively. We use the known parameter values $R = R_g^0 = \sqrt{11.3}$ for $N = 50$, $\Delta\varepsilon = \varepsilon - \varepsilon_{\mathrm{col}} = 1.34$ for $\varepsilon = 2$, and assume long protrusion $\alpha = 1$, $l_{\max} = 9$, which is an estimate deduced from fig. 4.3a. Note that we neglect the dependence of the collapse transition on the chain length and use a constant $\varepsilon_{\mathrm{col}}$. Satisfactory agreement is obtained between the theoretical result and the simulation data by adjusting the fit parameters $\zeta_{\mathrm{hyd}} = 2.2 \times 10^{-4}$ and $\zeta_{\mathrm{coh}} = 0.33$ for fig. 4.4b and $\zeta_{\mathrm{hyd}} = 3.7 \times 10^{-4}$ and $\zeta_{\mathrm{coh}} = 0.37$ for fig. 4.4d. The differences in the fitting factors might be due to the simplifying assumption that the maximal protrusion length $l_{\max}$ as well as $\varepsilon_{\mathrm{col}}$ are kept constant.

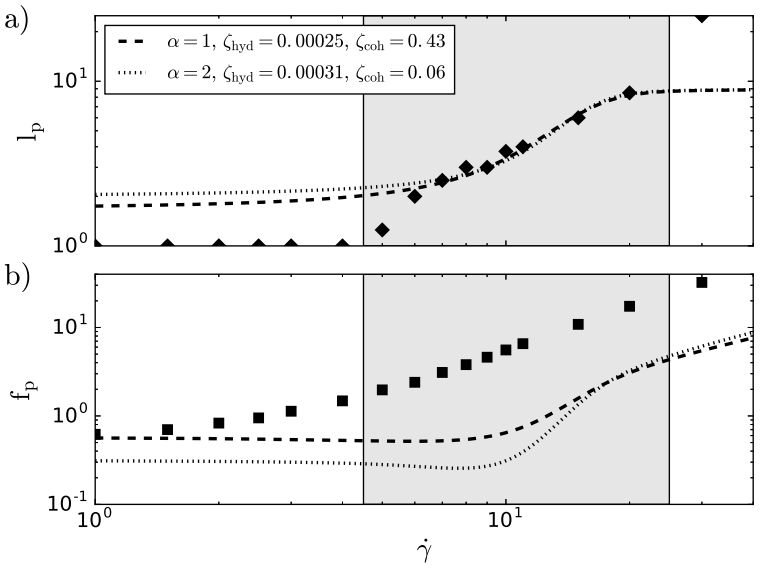

Figure 4.6: a) Average protrusion length l_p and b) peak force f_p as a function of shear rate for simulations with HI, $N = 50$ and $\varepsilon = 2$. Lines in a) represent theoretical results eq. (4.8) with exponent $\alpha = 1$ (dashed line), $\alpha = 2$ (dotted line) and fitting parameters ζ_{hyd} and ζ_{coh}. Lines in b) correspond to eq. (4.9) using the same parameters as in a). The shaded area indicates where double-peaks in the tension profile are observed.

We also compare the prediction of the quasi-equilibrium theory for the average protrusion length l_p , eq. (4.8), as a function of shear rate in fig. 4.6a for the same data as shown in fig. 4.3a. The result for $\alpha = 1$ is shown as a dashed curve and for $\alpha = 2$ as a dotted line. It can be seen that the simple theory does not describe the simulation data very accurately in the transition region. In fig. 4.6b we compare the peak force measured in simulations with the theoretical prediction, eq. (4.9), using the same fit parameter ζ_{hyd}

and ζ_{coh} as obtained from fig. 4.6a. Since the analytical prediction largely underestimates the simulation data we conclude that the simple combination of Boltzmann averaged length l_p and peak force f_p does not yield a consistent description of average protrusions. A somewhat better result is obtained for a small value $\alpha = 1$, which is in contradiction to the result of ref. [61] where the scaling behavior of the critical shear rate suggests $\alpha = 2$ for the HI case and hence short protrusions. We conclude that the quasi-equilibrium theory would have to be extended in order to consistently capture all properties of shear-induced protrusions.

An interesting question concerns the actual value of the exponent α characterizing the cohesive force on a protrusion defined in eq. (4.6). The scaling relation eq. (4.10) shown for fixed shear rate and globule size in fig. 4.4d as a solid line was not only introduced as a phenomenological power law, but it is also obtained when calculating the average protrusion length eq. (4.8) and neglecting the first term of eq. (4.7). Despite this simplistic assumption (note that both shear rate, shown in fig. 4.3a, and globule size, shown in fig. 4.4b, influence the average protrusion length) we can estimate the parameter $\alpha = 1.4$. This corresponds to an intermediate value between long protrusions and constant cohesive force, $\alpha = 1$, and short protrusions, $\alpha = 2$.

In conclusion, the quasi-equilibrium theory contains sufficient fit parameters in order to roughly match simulations results for the average protrusion length. This might be surprising as the time scale governing the transition between collapsed and unfolded state is large compared to the shortest relevant time scale in the system, which is the period of globule rotation, and thus rare events of full polymer elongations are presumably not accurately described by our quasi-equilibrium model. In line with this, the Boltzmann averaging of both l_p and f_p with the same fit parameters does not yield a consistent description of the average protrusion force measured in the simulation. In order to improve the accuracy we used the full velocity profile, eq. (4.4), for the calculation of the energy term U_{hyd} associated with the hydrodynamic drag on the protrusion instead of the approximation for short protrusions in eq. (4.5), but found no qualitative difference, only the prefactor ζ_{hyd} changes (data not shown). A further possible improvement of the theory might be to average over all possible protrusion configurations or to consider a maximal length l_{max} depending on globule size, cohesive strength, and shear rate.

4.4 Connection between tension profile and VWF proteolysis

The tension profiles that we investigated in the previous section can help to explain the shear-induced activation of collapsed biopolymers from a fundamental polymer physics point of view. In particular, in this section we make the connection between the shear-induced tension along a polymer chain and the shear-dependent proteolytic degradation of the multimeric blood protein von Willebrand factor (VWF) by its specific cleavage enzyme ADAMTS13. The ADAMTS13-mediated cleavage of full-length VWF in shear has been measured recently [146] using fluorescence correlation spectroscopy (FCS) in

combination with a microfluidic shear cell. The effect of shear on the kinetics of VWF cleavage in aqueous buffer and in blood plasma was quantified by measuring the time-resolved increase in molar VWF multimer concentration. One of the main results of that study was a strong sigmoidal increase of ADAMTS13 activity in plasma as a function of shear rate.

As has been shown previously, external forces induce an opening of the VWF A2 domain which thereby becomes accessible for cleavage by ADAMTS13 [18, 19]. In order to describe the opening process of the A2 domain required for cleavage by ADAMTS13, we employ a simple two-state model where a single subunit is either closed or open. The kinetics is described by the force-dependent opening and closing rates that determine the probability for the cleavage site to be in the open state, which in turn can be related to the shear-dependent cleavage rate measured in the experiment [146]. This allows to deduce parameters characterizing the process of stochastic domain opening and closing such as an effective force scale and the free energy difference from experimental shear-dependent measurements.

4.4.1 Morrison kinetics without shear flow

In the absence of shear flow, previous experiments measured the ADAMTS13-mediated cleavage of VWF under denaturing buffer conditions [146]. In order to observe cleavage activity without shear flow, the denaturant is essential to render cleavage sites accessible. The results are shown in fig. 4.7, where the cleavage rate increases with VWF multimer concentration C_V depending on the enzyme concentration C_A. In the context of enzyme kinetics, the cleavage rate can be described by the Morrison equation [148],

$$k_{\mathrm{CR}} = \frac{dC_V}{dt} = \frac{\tilde{k}_{\mathrm{cat}}}{2}\left(K_M + C_A + \bar{N}_{\mathrm{open}}C_V - \sqrt{\left(K_M + C_A + \bar{N}_{\mathrm{open}}C_V\right)^2 - 4C_A\,\bar{N}_{\mathrm{open}}C_V}\right), \quad (4.11)$$

with the catalytic rate constant $\tilde{k}_{\mathrm{cat}}$ and the Michaelis-Menten constant K_M. The central assumption is that the cleavage rate depends on the mean number of accessible monomers per VWF multimer, $\bar{N}_{\mathrm{open}}$, via the effective substrate concentration $\bar{N}_{\mathrm{open}}C_V$. Equation (4.11) is a generalized Michaelis-Menten equation without the free ligand approximation, i.e., it is valid for K_M values smaller than C_A and does not assume the free substrate concentration to be equal to the total substrate concentration, an approximation that might not be valid when accessible cleavage sites are sparse. Solid lines in fig. 4.7 represent global fits of the experimental data to eq. (4.11) with parameters $\tilde{k}_{\mathrm{cat}} = 0.001\,\mathrm{s}^{-1}$, $K_M = 2.3\,\mathrm{nM}$, and the number of accessible monomers $\bar{N}_{\mathrm{open}} = 0.04$. This means that the denaturing buffer only opens about four percent of the cleavage sites per multimer. Our results suggest domain opening to be the cleavage rate limiting factor

rather than the ADAMTS13 concentration, since the K_M is below the physiological $C_A = 5.3\,\mathrm{nM}$.

The Michaelis-Menten constant of $K_M = 962\,\mathrm{nM}$ determined previously [146] results from the alternative assumption that all cleavage sites are accessible under denaturing conditions, i.e. $\bar{N}_{\mathrm{open}} = N_m$, where the average number of monomers is obtained by the experimentally determined VWF length distribution [20]

$$N_m = \frac{2\sum_{N=1}^{\infty} N\, n^{N-1}}{\sum_N n^{N-1}} = 5.6, \tag{4.12}$$

with the parameter $n = 0.64$. Here, we present the alternative approach of introducing the mean number of accessible monomers $\bar{N}_{\mathrm{open}}$ as a fit parameter, which allows the consistent description of shear-dependent experiments, as explained in sec. 4.4.3. The simultaneous fit of the two different enzyme concentrations in fig. 4.7 with the same $\tilde{k}_{\mathrm{cat}} = 0.001\,\mathrm{s}^{-1}$ is an advantage compared to the method used previously [146], where the catalytic rate constant depends on C_A. More experimental data for different enzyme concentrations would be needed in order to consolidate the present fitting approach.

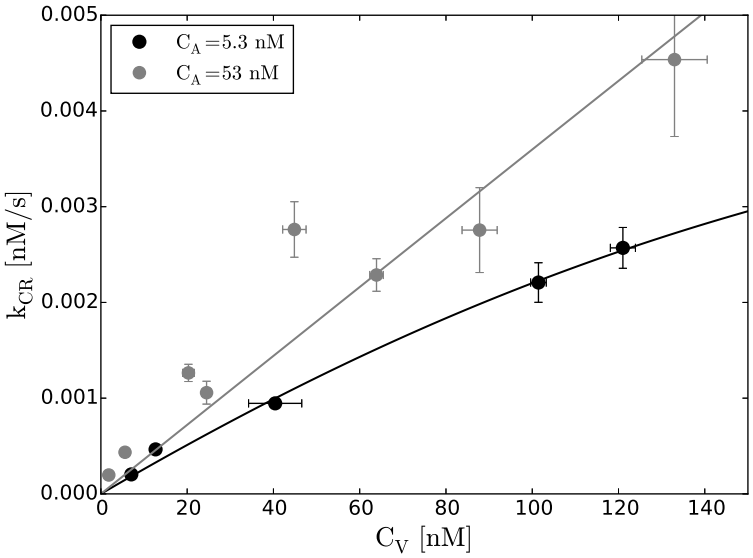

Figure 4.7: Experimental data from [146] for the cleavage rate in denaturing buffer as a function of multimer concentration C_V for two different ADAMTS13 concentrations $C_A = 5.3\,\mathrm{nM}$ (black) and $C_A = 53\,\mathrm{nM}$ (grey). Lines illustrate Morrison kinetics eq. (4.11) with fit parameters $\tilde{k}_{\mathrm{cat}} = 0.001\,\mathrm{s}^{-1}$, $K_M = 2.3\,\mathrm{nM}$, and $\bar{N}_{\mathrm{open}} = 0.04$.

4.4.2 Model for stochastic cleavage site opening under tensile forces

In our homopolymer model, a spherical bead of radius a represents the VWF's repeating unit, i.e. a dimer. Since rescaled shear rates $\dot{\gamma} = \tilde{\dot{\gamma}}\tau$ are used with timescale $\tau = 6\pi\eta a^3/\mathrm{kT}$,

simulation results can be interpreted in terms of arbitrary values of radius and viscosity. In order to compare the dimensionless simulation values to physical units, we use the viscosity $\eta = 1.2 \times 10^{-3}\,\mathrm{Pa\,s}$, and temperature $T = 310\,\mathrm{K}$. The remaining parameters are the bead radius a and the cohesive strength ε, which strongly influence the critical shear rate at which shear-induced unfolding of the polymeric globule sets in [61]. We choose the cohesive parameter $\varepsilon = 2$ so that in the absence of shear flow the polymer is collapsed but still far from the freezing transition at around $\varepsilon_{\mathrm{freeze}} = 4$ [129]. The dimensionless critical shear rate that we determine for a globule with $N = 50$ is about $\dot{\gamma}^* = 10$ (fig. 4.1b), which translates to the experimental value $\tilde{\dot{\gamma}}^*_{\mathrm{exp}} \approx 5000\,\mathrm{s}^{-1}$ [31] when using the bead radius $a = 73\mathrm{nm}$. This compares well with literature values of the VWF monomer size ranging from 60 nm to 82 nm [17, 28, 29]. Note that the critical shear rate also depends on the bead number [61], however, here for simplicity we consider a system with $N = 50$ beads.

From simulations we obtain the average tension f_i between adjacent beads (figs. 4.2a,d) and calculate the probability for a cleavage site to be open, given by

$$P_i = \frac{1}{1 + e^{\Delta F} e^{-f_i/f_e}}. \tag{4.13}$$

This expression can be derived by considering the reversible reaction of the cleavage site from being in the closed state to the open state, which we assume to be separated by a transition state energy barrier. The corresponding rate equation for the time-dependent probability to be in the open state P_i is given by

$$dP_i/dt = k_o\,(1 - P_i) - k_c P_i. \tag{4.14}$$

Whereas the opening rate $k_o = k_o^0 \exp(f_i/f_o)$ increases exponentially with tension according to the characteristic opening force scale f_o, the closing rate $k_c = k_c^0 \exp(-f_i/f_c)$ is assumed to decrease with tension according to the closing force scale f_c (which in general is different from f_o). Opening and closing rates in the absence of force are defined by k_o^0 and k_c^0. In a stationary state, the time derivative of P_i vanishes and we obtain eq. (4.13), where the effective force scale is defined by

$$f_e = 1/\left(1/f_o + 1/f_c\right) \tag{4.15}$$

and the unstressed equilibrium constant $k_o^0/k_c^0 = \exp(\Delta F)$ defines the free energy difference ΔF between open and closed state. Compared to the length $x_o = \mathrm{kT}/f_o$, which is the distance along the reaction coordinate from the closed state to the transition state, the distance $x_c = \mathrm{kT}/f_c$ between transition state and fully open state, e.g. the unfolded A2 domain stretched to its contour length, is presumably much larger and thus $f_c \ll f_o$. Consequently, from eq. (4.15) we conclude that the force scale of the closing transition dominates the effective force scale $f_e \approx f_c \ll f_o$.

Considering the entire polymer, we define the mean number of accessible cleavages sites

$$N_{\mathrm{open}}(N) = 2 \sum_i^N P_i \tag{4.16}$$

where the prefactor accounts for the fact that every dimer exhibits two cleavage sites. The cleavage process consists of three steps: the opening of the cleavage site, diffusion of the enzyme to this active site, and the actual catalytic cleavage. Our underlying assumption is that the domain opening and not diffusion or the chemical reaction is the rate limiting mechanism for the cleavage process. We thus assume that when there is an open cleavage site, the probability being described by eq. (4.13), the diffusion rate as well as the reaction rate are large enough such that VWF is readily cleaved.

In order to obtain the size averaged number of open cleavage sites, the weighted arithmetic mean is calculated

$$\bar{N}_{\mathrm{open}} = \frac{\sum_N^{N_{\max}} n^{N-1} N_{\mathrm{open}}(N)}{\sum_N^{N_{\max}} n^{N-1}} \tag{4.17}$$

according to an exponential VWF size distribution with the parameter $n = 0.64$, which was determined by fluorescence correlation spectroscopy of VWF in blood plasma [20]. Because simulation results are used to calculate $N_{\mathrm{open}}(N)$, the upper boundary in the sums of eq. (4.17) is set to a maximal chain length $N_{\max} = 10$. Taking into account longer chains does not alter the result due to the negligible weights for large N in eq. (4.17).

4.4.3 Mapping simulation results and experiments of shear-induced VWF cleavage

Cleavage rates of VWF in blood plasma [146] as a function of shear rate, shown in fig. 4.8a as black symbols, exhibit a steep increase corroborating the concept of shear-induced opening of the A2 cleavage domain. The experimental data can be described by a phenomenological sigmoidal function

$$k_{\mathrm{CR}} = k_{\max} \frac{1}{1 + e^{-(\tilde{\dot{\gamma}} - \tilde{\dot{\gamma}}_c)/\Delta\tilde{\dot{\gamma}}}}, \tag{4.18}$$

illustrated as a black line in fig 4.8a, with fitting parameters $\Delta\tilde{\dot{\gamma}} = 1271\,\mathrm{s}^{-1}$ and $\tilde{\dot{\gamma}}_c = 5522\,\mathrm{s}^{-1}$, the latter being interpreted as the half maximum shear rate. The enzyme activity dependent prefactor $k_{\max} = 0.0035\,\mathrm{nM/s}$ denotes the maximal enzymatic rate in the case of fully accessible cleavage sites. Notice that high cleavage activity is closely related to the shear-induced VWF unfolding transition since the half maximum shear rate $\tilde{\dot{\gamma}}_c$ agrees with the critical shear rate of unfolding, $\tilde{\dot{\gamma}}^*_{\mathrm{exp}} \approx 5000\,\mathrm{s}^{-1}$ [31], where the polymer size fluctuations are maximal.

The connection to simulation results is established using the Morrison eq. (4.11) in combination with the shear-dependent mean number of open monomers, eq. (4.17) with eqs. (4.13) and (4.16). The tensile force profiles f_i are taken from our simulations in the previous sec. 4.3 and we use the Michaelis-Menten constant $K_M = 2.3\,\mathrm{nM}$ determined in sec. 4.4.1 under denaturing buffer conditions since we expect that value not to be very different in blood plasma. The ADAMTS13 concentration in the blood plasma was $C_A = 1.3\,\mathrm{nM}$ and the VWF concentration $C_V = 13\,\mathrm{nM}$ [146]. As a result of a least

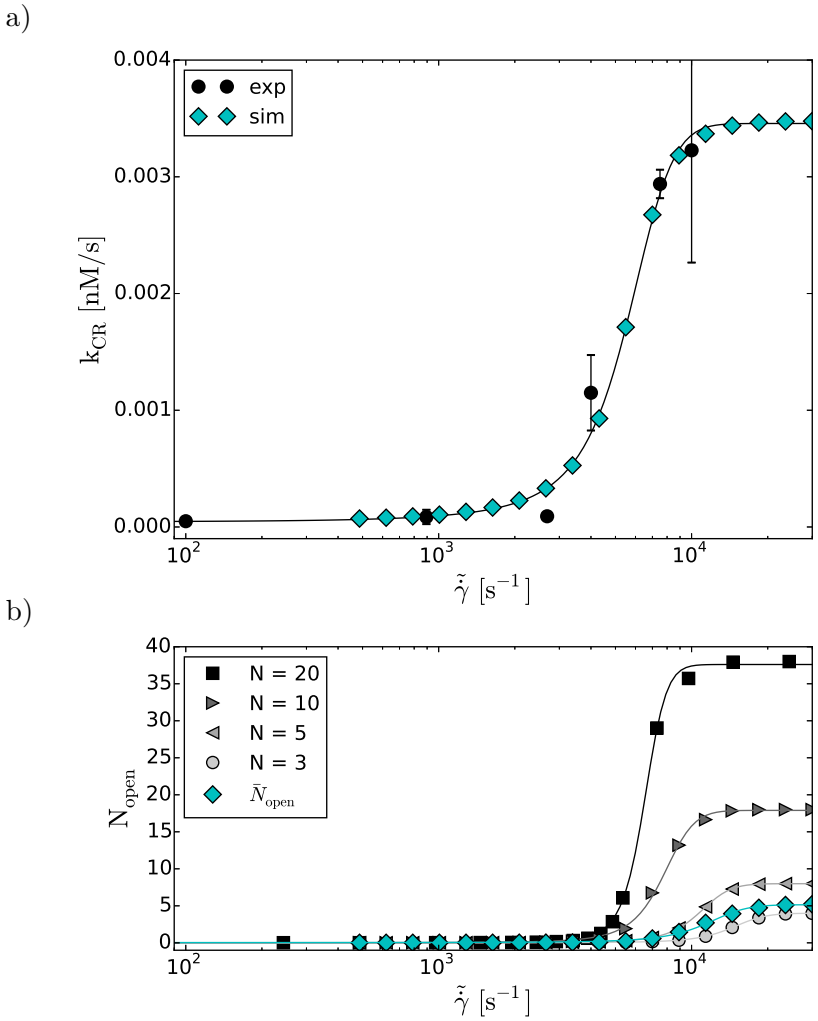

Figure 4.8: a) Experimental data for the cleavage rate of VWF in blood plasma (black symbols, data from [146]) as a function of shear rate is described by the phenomenological sigmoidal function, eq. (4.18), as a solid line. Assuming a stochastic model for the description of the probability of a subunit to be open, eq. (4.13), and the mean number of open cleavage sites $\bar{N}_{\text{open}}$ to determine the substrate concentration in the Morrison eq. (4.11), agreement with simulation data (cyan symbols) is obtained for fitting parameter values $\Delta\tilde{F} = 8.5\,\text{kT}$, $\tilde{f}_e = 0.06\,\text{pN}$, and a catalytic rate constant $\tilde{k}_{\text{cat}} = 0.0027\,\text{s}^{-1}$. b) Simulation results for the mean number of open cleavage sites, eq. (4.16), as a function of shear rate for a few different chain lengths N. The size-averaged number $\bar{N}_{\text{open}}$ according to eq. (4.17) is denoted by cyan symbols. Lines are fits to a sigmoidal function according to eq. (4.18).

square fit, as seen in fig. 4.8a, simulations results (cyan symbols) match the sigmoidal description (solid line) of the experimental data. We obtain the fit parameters $\Delta F = 8.5$ in units of kT and $f_e = 1.0$ characterizing the probability of single subunits to be accessible, eq. (4.13), as well as the catalytic rate constant $\tilde{k}_{\mathrm{cat}} = 0.0027\,\mathrm{s}^{-1}$, which is in satisfactory agreement with the $0.001\,\mathrm{s}^{-1}$ obtained in the absence of shear flow, fig. 4.7. The force scale in physical units is given by $\tilde{f}_e = 0.06\,\mathrm{pN}$. Notice that the length scale $\tilde{x}_c \approx \tilde{x}_e = \mathrm{kT}/\tilde{f}_e = 69\,\mathrm{nm}$ associated with the distance along the reaction coordinate between the open state and the transition state is comparable the contour length of the A2 domain of 58 nm [136].

The dependence of the mean number of open monomers on the chain length N is illustrated in fig. 4.8b. For a few different lengths we plot N_{open} as a function of the shear rate, using the parameters obtained before: $\Delta F = 8.5$ and $f_e = 1.0$. Lines represent sigmoidal fits according to eq. (4.18). The saturating value is proportional to the contour length and with increasing N the transition shifts towards lower values of the shear rate indicating that the probability to find open cleavage sites is higher for longer polymers. We also plot the size-averaged number according to eq. (4.17) denoted by cyan symbols.

4.4.4 Alternative models for mean number of accessible cleavage sites

4.4.4.1 Alternative model I

In this section, we present an alternative definition of the mean number of open cleavage sites $\bar{N}_{\mathrm{open}}$, eq. (4.17), that describes the shear-dependence of the cleavage rate, eq. (4.11). We employ an analytical approach to calculate the probability of cleavage sites to be open based on our scaling results from sec. 4.3.1.1. While the model eq. (4.13) includes simulations results directly via the measured average forces, f_i, along the polymer chains, here we consider the mean force, $f_i \approx f_{\mathrm{mean}}$, which depends on the shear rate according to $f_{\mathrm{mean}} \sim \dot{\gamma}^{1.8}$, as seen in fig. 4.3b. We thus assume equal probability for any cleavage site to be open and obtain for the mean number of open cleavage sites

$$\bar{N}_{\mathrm{open}} = N_m \frac{1}{1 + e^{\Delta F} e^{-(\tilde{\dot{\gamma}}/\tilde{\dot{\gamma}}_e)^{1.8}}}, \tag{4.19}$$

where the average number of monomers is given by eq. (4.12). Following the same fitting procedure as before, we obtain the fit parameters $\Delta F = 4.9$, $\tilde{\dot{\gamma}}_e = 3322\,\mathrm{s}^{-1}$, and $\tilde{k}_{\mathrm{cat}} = 0.0028\,\mathrm{s}^{-1}$ and plot the result in fig. 4.9 as a red dashed line. The analytical approach using a power law for the shear-dependence of the mean tensile forces yields a suitable description of the experimentally observed cleavage rate. Compared to the result from sec. 4.4.3, the catalytic rates agree very well but the free energy difference is smaller by 3.6 kT. We conclude that based on the quality of fits in fig. 4.9 it is not possible to decide whether the assumption underlying eq. (4.17) or eq. (4.19) is valid. This means that it remains unclear to what extent the inhomogeneous force profiles as shown in fig. 4.2 influence the cleavage process of VWF multimers. It might be possible

for instance that cleavage occurs predominantly at the sites of maximal tensile forces along the multimer contour.

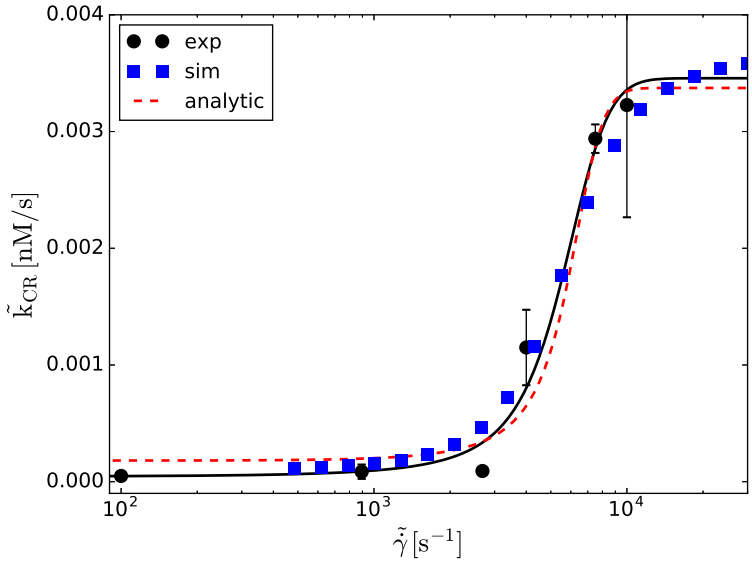

Figure 4.9: Alternative models describing experimental cleavage rates in blood plasma (black symbols) as a function of shear rate. The black solid line represents the phenomenological sigmoidal function, eq. (4.18). The analytical model uses the mean number of open cleavage sites, eq. (4.19), and the fit of eq. (4.11) (red dashed line) yields a very similar result for the cleavage rate. Instead of using the average forces f_i for the calculation of the probability P_i, eq. (4.13), for the blue symbols we use the average of P_i, eq. (4.21), which takes into account the full distribution of tensile forces.

4.4.4.2 Alternative model II

Another method to model the fraction of accessible monomers and thereby the cleavage rate is based on the observation of broad distributions of the tensile forces, shown in fig. 4.2c. These are fitted with a Gaussian,

$$G_i(f) = \exp\left(-\left(f - f_i\right)^2 / \left(2\sigma_i^2\right)\right) / \sqrt{2\pi\sigma_i^2}, \tag{4.20}$$

in order to gather mean force f_i and standard deviation σ_i that are used to calculate the average probability of the cleavage site to be open

$$\hat{P}_i = \int_{-\infty}^{\infty} G_i(f) \frac{1}{1 + e^{\Delta F} e^{-f/f_e}} df. \tag{4.21}$$

In contrast to eq. (4.13), where only the average forces f_i are used to calculate the probability of an open cleavage site, eq. (4.21) takes into account the full distribution of

tensile forces. The result of the fit of eq. (4.11) using $N_{\mathrm{open}}(N) = 2\sum_i^N \hat{P}_i$ and eq. (4.17) is illustrated in fig. 4.9 as blue symbols with fit parameters $\Delta F = 12.5$, $f_e = 1.67$ and $\tilde{k}_{\mathrm{cat}} = 0.0029\,\mathrm{s}^{-1}$. Although this methods leads to an adequate graphical description of the cleavage rate, the interpretation of the result is difficult since we find multiple minima of the non-linear least square method indicating a strong dependence of the parameters ΔF and f_e. The large free energy difference $\Delta F = 12.5$ between the open and the closed state might suggest that when using the full tension distribution one overestimates the influence of the force on the probability to find open monomers. In conclusion, it remains unclear to what extent the strong fluctuations of the tensile force, which are due to the rare events of full polymer unfolding, contribute to the cleavage domain opening that determines the shear-induced cleavage process.

4.4.5 Comparison to VWF A2 domain unfolding upon external stretching force

In the following we make the connection to the force-induced unfolding of the isolated A2 domain measured with optical tweezers [136], where it is hypothesized that unfolding of A2 is required for cleavage by ADAMTS13. In that study, unfolding forces are measured as a function of force loading rates. In line with our assumption, the unfolding rate $k_u = k_u^0 \exp(f/f_u)$ is assumed to increase exponentially with applied force f, and the characteristic force scale f_u of A2 unfolding is determined. Note that the unfolding of A2 probed in the force spectroscopy experiments is not necessarily the same process as probed in the ADAMTS13 cleavage experiments in shear, as we will explain in the following.

In our analysis in sec. 4.4.2 we identify the closing force scale f_c to be the dominating factor governing the force dependence of the probability P_i of cleavage sites to be accessible. In other words, the characteristic force scale of opening, f_o, is not directly accessible in our model as we only determine the effective force scale $f_e \approx f_c \ll f_o$. This is one reason why the effective force scale $f_e = 0.06\,\mathrm{pN}$ characterizing the sigmoidal behavior of P_i in shear flow is very different compared to the force scale for unfolding induced by an external stretching force $f_u = 1.1\,\mathrm{pN}$ [136]. The other reason why the force scales are different could be that cleavage by ADAMTS13 does not require the full unfolding of the A2 domain. Only if the unfolding of the A2 domain would be a necessary step before ADAMTS13 can access the cleavage site, and only if the process of force-induced A2 unfolding was equivalent to the shear-induced opening of the ADAMTS13 cleavage site in VWF, would f_u correspond to the opening force scale f_o. Based on our approach modeling the shear-induced cleavage of VWF, that is close to the physiological situation, one might speculate that the process of force-induced A2 unfolding is fundamentally different. This is in line with literature results [19, 136] that suggest an partially unfolded, intermediate state of the A2 domain to be sufficient for ADAMTS13 cleavage. There are further conceivable mechanisms of how forces might induce increased cleavage activity in VWF. Interactions of multiple domains could, for instance, shield the cleavage site in the

absence of force; only upon applied forces domains might separate and thereby enable cleavage.

Zhang et al. [136] also determined the rate of A2 refolding, employing a model where the refolding rate is described by $k_f \sim \exp\left(-f^2/\left(2\kappa\,\mathrm{kT}\right)\right)$. That model assumes soft compliance of the unfolded state described by a harmonic potential $U_{\mathrm{harm}} \sim -f^2/\kappa \sim \kappa R_{\mathrm{ee}}^2$, where κ denotes the effective spring constants that characterizes the polymer elasticity and R_{ee} is the polymer end-to-end distance. Due to the different modeling for the closing rate, we can only compare the rates in the absence of force and thus the equilibrium constant, or equivalently the free energy difference between the two states. As a result, we obtain from our fit an estimate for the energy difference $\Delta\tilde{F} = 8.5\,\mathrm{kT}$, which is higher by about 2 kT compared to the single barrier A2 unfolding and refolding kinetic model [136]. Although we would have expected a smaller free energy difference since shear presumably only partially unfolds the A2 domain, this difference is not surprising given the different model assumptions that go into the analysis of the experimental data. In terms of enzyme activity, Zhang et al. determined a catalytic rate constant of $0.14\,\mathrm{s}^{-1}$ for single, accessible A2 domains and varying enzyme concentration [136]. The cleavage of A2 fragments independent of unfolding is presumably a less physiological situations. Since we considered shear-induced cleavage of full-length VWF in blood plasma the smaller rate constant that we obtained, $\tilde{k}_{\mathrm{cat}} = 0.0027\,\mathrm{s}^{-1}$, might not be surprising.

4.5 Summary and conclusion

In the present study we investigate the tension profile of collapsed homopolymers in shear flow by Brownian hydrodynamics simulations. Profiles for long polymers exhibit a characteristic double-peak structure that we argue is related to polymeric protrusions and forms the basis of a nucleation argument used in previous work to explain the instability mechanism behind shear-induced unfolding [58, 61]. The range of shear rates where the double-peak structure in the tension profiles occurs roughly coincides with the peak of the variance of the chain extension, which was previously used to define the critical shear rate of unfolding. By heuristic fits of the simulation results, we find scaling relations $f_p \sim \dot{\gamma}^{1.6}$ and $l_p \sim \dot{\gamma}^{1.2}$ for the peak force and the average protrusion length, respectively. Average protrusions lengths are in the range $1 < l_p < 10$. For fixed shear rate, the protrusion length decreases with increasing globule size according to $l_p \sim R^{-1}$. In terms of the cohesive strength, protrusions occur for collapsed globules $\varepsilon > \varepsilon_{\mathrm{col}}$ and for fixed shear rate the protrusion length decreases roughly linearly with ε until the globule undergoes a freezing transition and protrusions disappear at about $\varepsilon \approx 3$. The peak force decreases roughly linearly both as a function of globule size and cohesive strength.

A quasi-equilibrium theory with a few fit parameters describes the behavior of the average protrusion length only in parts. This might be due to the fact that the transition between collapsed and unfolded state is slow compared to the shortest relevant time scale in the system, which is the period of globule rotation. Rare events of full polymer elongations

are thus not accurately described by a quasi-equilibrium model. On the other hand, the previously established nucleation model can be successfully used to predict the critical shear rate at which unfolding sets in [58]. Since we do not observe a double-peak structure in the free draining case, we conclude that the protrusion mechanism for unfolding only applies to the case when hydrodynamic interactions are taken into account. This is is an interesting observation in comparison with previous scaling arguments [58].

In the second part we consider experiments of ADAMTS13-mediated VWF cleavage. First we analyze the Morrison kinetics of the cleavage process without shear flow in denaturing buffer and obtain $K_M = 2.3\,\mathrm{nM}$ and the catalytic rate constant $\tilde{k}_{\mathrm{cat}} = 0.001\,\mathrm{s}^{-1}$. Under such denaturing conditions, we find that only a small average number of cleavage sites $\bar{N}_{\mathrm{open}} = 0.04$ is accessible per multimer. Our results suggest domain opening to be the cleavage rate limiting factor rather than the ADAMTS13 concentration. Next we connect the simulated tension profile, via a stochastic two state model for the cleavage domain opening of each monomer, to the experimentally measured shear-dependent cleavage rate of VWF in blood plasma. Due to the occurrence of protrusions one can speculate that ADAMTS13 is likely to cut VWF multimers towards the terminal ends, which are pulled out of the globules and therefore are most accessible. Our model qualitatively describes the sigmoidal increase of the cleavage rate with increasing shear rate and we obtain as a main result the parameters characterizing the probability of an individual cleavage domain to be accessible, i.e., the effective force scale $\tilde{f}_e = 0.06\,\mathrm{pN}$ and the free energy difference between open and closed state $\Delta\tilde{F} = 8.5\,\mathrm{kT}$. Furthermore, the catalytic rate constant of the cleavage process is found to be $\tilde{k}_{\mathrm{cat}} = 0.0027\,\mathrm{s}^{-1}$, in satisfactory agreement with $\tilde{k}_{\mathrm{cat}} = 0.001\,\mathrm{s}^{-1}$ obtained for cleavage in denaturing buffer.

The present study further elucidates the complex dynamical behavior of collapsed polymers in shear as the basis for non-equilibrium phenomena with high physiological relevance. The shear-induced VWF unfolding leads to inhomogeneous tensile force distributions and thereby strongly influences the susceptibility to proteolytic cleavage. Our findings are not limited to VWF's hemostatic function but are relevant for a number of nanotechnological and biomedical applications where functional polymers or proteins are engineered as shear-responsive smart materials or drug delivery systems. Future lines of work might involve further components that modulate the cleavage of VWF in blood plasma. It has been shown that the presence of coagulation factor VIII [149] as well as platelets [150] increases the susceptibility of VWF to cleavage by ADAMTS13. Including additional particles in the simulation model could yield valuable insight into the interplay of cofactors that bind to the polymeric monomers, conformational changes and the tension profile that in turn affects the cleavage activity. In fact, simulations of VWF and platelets have been conducted observing the formation of reversible aggregates under shear flow conditions [8]. Further VWF domain model refinements might capture atomistic details that influence the cleavage process. Domain shielding renders VWF inactive for adhesion or proteolysis [138]. On an even smaller length scale, local mutations in the VWF A2 domain that are known to affect the ADAMTS13 susceptibility [151] and also environmental conditions play a crucial role, e.g. calcium stabilizes the A2 domain and thus regulates the unfolding [152].

It would be desirable to capture such effects in simple physical models that might be able to relate mutations directly to hemostatic dysfunction.

Chapter 5

Summary and Outlook

The aim of this dissertation has been to elucidate the complex dynamics of biophysical polymeric systems such as the large multimeric blood protein von Willebrand factor using fundamental concepts of polymer physics. Motivated by experimental findings of the somewhat counterintuitive behavior such as shear-induced activation, adhesion and degradation of VWF in the context of blood clotting, we theoretically investigated a number of non-equilibrium phenomena using a collapsed homopolymer model that represents a minimal coarse-grained model for VWF. In particular, we examined the role of shear on the dynamics and the adsorption behavior of polymeric globules. As a primary tool we employed solvent-implicit Brownian hydrodynamics simulations.

First, we investigated the adsorption behavior of a single polymer next to adsorbing surfaces presenting simple potential-based binding models. In Chapter 2, as a result of extensive simulations and global parameter variation, we have obtained state diagrams with several distinct dynamical states and transitions, depending on the characteristic parameters such as shear rate as well as adhesive and cohesive strengths. For the homogeneous surface we detected and characterized transitions between different rolling and slipping states, prolate-oblate shape transitions as well as periodic stretching-refolding of the polymeric globule. As a main result, an increase in shear does not lead to enhanced adsorption. This means that the increased hydrodynamic lift force due to shear is not compensated by an enhanced binding of the unfolded polymer to the potential-based homogeneous surface. Whether friction effects represent an alternative mechanism for shear-induced adsorption was addressed in the second part of Chapter 2 where we introduced an inhomogeneous surface potential consisting of an ordered array of discrete attractive binding sites. High lateral surface friction, as a result from low density of the binding sites with short interaction range, leads to new dynamical states such as conformations that are temporarily stuck on the surface, as opposed to the continuous slipping or rolling that is observed on homogeneous surfaces. However, the adsorption behavior does not change qualitatively. We conclude that for a generic coarse-grained simple polymer model that is entirely based on time-independent energy-conserving pair potentials between monomers and the surface, the globule adsorption is not enhanced by the presence of shear. Hydrodynamic shear flow always favors the desorbed state of a single globular or coiled polymer. This stands in contrast with experimental findings and thus demonstrates that in order to obtain shear-induced adsorption behavior, a more complex binding mechanism including saturating bonds or catch bonds is necessary.

Second, we examined the adsorption of a polymeric globule in shear flow applying stochastic two-state surface-monomer bonds. In Chapter 3, we addressed the question what the minimal conditions are in order to observe shear-induced adsorption and extended earlier theoretical studies showing that slip-resistant catch bonds with long lifetimes are a necessary ingredient. We constructed adsorption state diagrams as a function of the three parameters characterizing the kinetics of the surface-monomer bonds: the rates of bond formation, the rate of bond dissociation as well as an effective catch bond parameter that allows to continuously change from slip to catch bond behavior. Shear-induced adsorption is obtained only in a narrow range of parameters for low dissociation rates and similarly low association rates and only when the surface-monomer bonds are adjusted close to the transition between slip and catch bond behavior. Our results thus elucidate the underlying physical mechanism: a globular polymer remains collapsed at low shear flow. When it approaches the surface, only few monomers get into the surface interaction range and adhesion is suppressed by low associations rates. By contrast, once a bond is formed and the shear rate is large enough, the polymer tethered to the surface readily unfolds. Under the conditions of a large timescale for bond dissociation compared to the timescale of shear-dependent globule unfolding, more monomers can bind to the surface resulting in shear-enhanced adsorption. This explains the necessary condition of bonds having a low dissociation rate and that are, to some extend, resistant against tensile force. However, too strong catch bond behavior would result in permanent adsorption also for vanishing flow. In fact, we showed that the shear-induced adsorbed state is reversible in the sense that the adsorbed globule readily desorbs when the flow is suddenly switched off. We conclude that biological systems such as VWF have to be finely adjusted in terms of their surface binding in order for flow effects to enhance adsorption. By mapping of the kinetic two-state model parameters onto a surface-monomer interaction model based on conservative pair potentials, we estimated the potential parameters necessary to observe shear-induced surface adsorption phenomena. We thereby addressed the intriguing question of how macromolecules achieve catch bond behavior when interacting via pair potentials. By construction, the simple potential-based model does not allow for negative effective catch bond parameters, i.e. only slip bond behavior is possible. However, by reducing the surface interaction range we obtained very small positive values for the effective catch bond parameter and thus bonds with a weak slip behavior. On the other hand, our model lacks an additional energy barrier preventing adsorption in the case of vanishing shear flow. We concluded that it remains unclear what a minimal model based on pair potentials is that exhibits catch bond behavior and is able to describe shear-induced adsorption.

Third, we explored the interplay between shear flow, globule unfolding, and the enzymatic cleavage of VWF that requires force-induced A2 domain opening. In Chapter 4, we have shown that the shear-induced tensile force distributions along the backbone of polymeric globules in an unbound fluid exhibit under certain conditions a characteristic double-peak structure, a feature that is a direct consequence of polymeric protrusions that are pulled out from the globule due to hydrodynamic shear forces. We thus corroborate the protrusion mechanism for the unfolding of sheared polymer globules and determined

scaling relations for the average protrusion length and the maximal force as a function of shear rate, chain length, and cohesive strength. The connection of the shear-induced internal tension in a polymeric globule to the experimentally measured shear-dependent cleavage rate of VWF in blood plasma has been established. A simple stochastic model was employed to describe the kinetics of the VWF cleavage domain opening and, as a main result, we obtained parameters characterizing the probability of individual cleavage sites to be accessible for cleavage. In sum, we elucidated how the non-equilibrium dynamics of collapsed polymers determines biological processes such as the degradation of VWF by an intricate relation of shear-induced globule unfolding and domain opening.

Summarizing, the present work has demonstrated how simple coarse-grained models and Brownian hydrodynamics simulations allow for new microscopic insights into the shear-induced phenomena of globular polymeric systems. We have provided detailed insight into the complex dynamics of collapsed polymers near adsorbing surfaces that are important with regard to various biophysical processes ranging from transport of cells or vesicles to the specific function of VWF in primary hemostatis. The results obtained in this study might be relevant not only for biological systems but also for nanotechnological developments such as rheology modifiers and drag reducing agents. One aim of this work has been to understand the counterintuitive behavior of shear-induced adsorption and degradation. We have elucidated the presumable physical mechanism that leads to shear-induced globule adsorption and characterized the conditions of the biological bonds that mediate such behavior in principle. We have shown that studying the conformational behavior of globular polymers in shear flow including protrusion-induced unfolding and the resulting tensile force profiles can be used to explain experimental data for the shear-sensitive enzymatic degradation of biopolymers.

5.1 Future work

The investigations in the present work revealed that more elaborate potential-based binding models should be developed in order to better understand the molecular mechanism underlying catch bond phenomena. Future lines of work might thus be targeted at model refinements that could include a more detailed description of the VWF domain structure and the dynamic characteristics of bonds between VWF and the surface. As will be explained below, the competition between adhesion and cohesion due to saturated binding sites could lead to the possibility of surface adhesion only in the case when the cohesive intra-VWF bonds are weakened or broken in shear flow, which in turns could yield a mechanism of adsorption enhancement due to applied shear. A further extension of the present study would be not only to describe the surface adhesion potential by a kinetic two-state model but also the intra-VWF cohesive interactions. Shear-induced adsorption might occur whenever the adhesive bonds show less slip behavior than the cohesive bonds, a hypothesis that has to be scrutinized in detail. In terms of VWF degradation, prospective research efforts should include further components that modulate the

cleavage in blood plasma such as coagulation factor VIII or platelets. The addition of small hydrophobic particles in the simulation model would be interesting with respect to conformational changes of the polymer that influence the tensile forces and thereby affect the cleavage activity. In the following we specify aforementioned prospective research and present some preliminary work.

5.1.1 Model for bond activation and saturation

The experimental observation that the VWF is activated by high shear flow, leading to unfolding and simultaneously to surface adsorption, is not reproduced in our potential-based coarse-grained polymer model where each VWF dimer is modeled as a sphere with isotropic cohesive interactions. In this thesis we have shown, using a bond model based on stochastic on-off reaction kinetics, that a necessary condition for such a shear-induced adsorption are bonds having a long lifetime and that are resistant against forces.

In the following we suggest an extension of the potential-based model. The goal is to devise a VWF dimer model, which responds to forces by a slight unfolding and thereby activates binding sites for the adsorption onto the surface. One way to achieve this is by using saturating or shielding bonds that can only bind to either surface or monomer, but not to both at the same time. This might lead to the possibility of enhanced surface adhesion in the case when cohesive intra-VWF bonds are weakened or broken in shear flow and thus could constitute a physical (i.e. potential-based) mechanism for shear-induced adsorption enhancement without the need to postulate surface catch bond.

A simple way of achieving saturating bonds is schematically illustrated in fig. 5.1a. Large spherical monomers shown in grey are combined with attractive sites that have a relatively short range, as illustrated by the small red beads. Only every second monomer is decorated with such a red bead that can freely move on the surface of the grey bead. This presents a simple model for the dimeric VWF structure since dimers will form for large enough cohesive attraction between the red beads. The cohesive interaction strength and range of the red binding sites can be tuned such that one binding site can only bind to at most one other binding site, which would thus correspond to a saturating bond. If the red beads also bind to the surface sites, as schematically illustrated in fig. 5.1b, we also have bond shielding, meaning that the surface-binding site is shielded by the VWF-VWF binding site. On a molecular level, this shielding can result from the close proximity of binding sites that are responsible for the VWF dimer cohesion and the VWF-surface binding. The basic idea behind this model is that at low shear rates the polymer is collapsed, stabilized by saturated bonds between the monomers (fig. 5.1a). In this state, all surface binding sites on the VWF are shielded and are therefore not available to form bonds with binding sites on the surface. As a consequence, adsorption cannot occur. Only when bonds between the VWF monomers are broken due to shear flow, binding sites are exposed to the surface and the polymer can adsorb (fig. 5.1b). A goal for future work would be therefore to understand the competition between adhesion

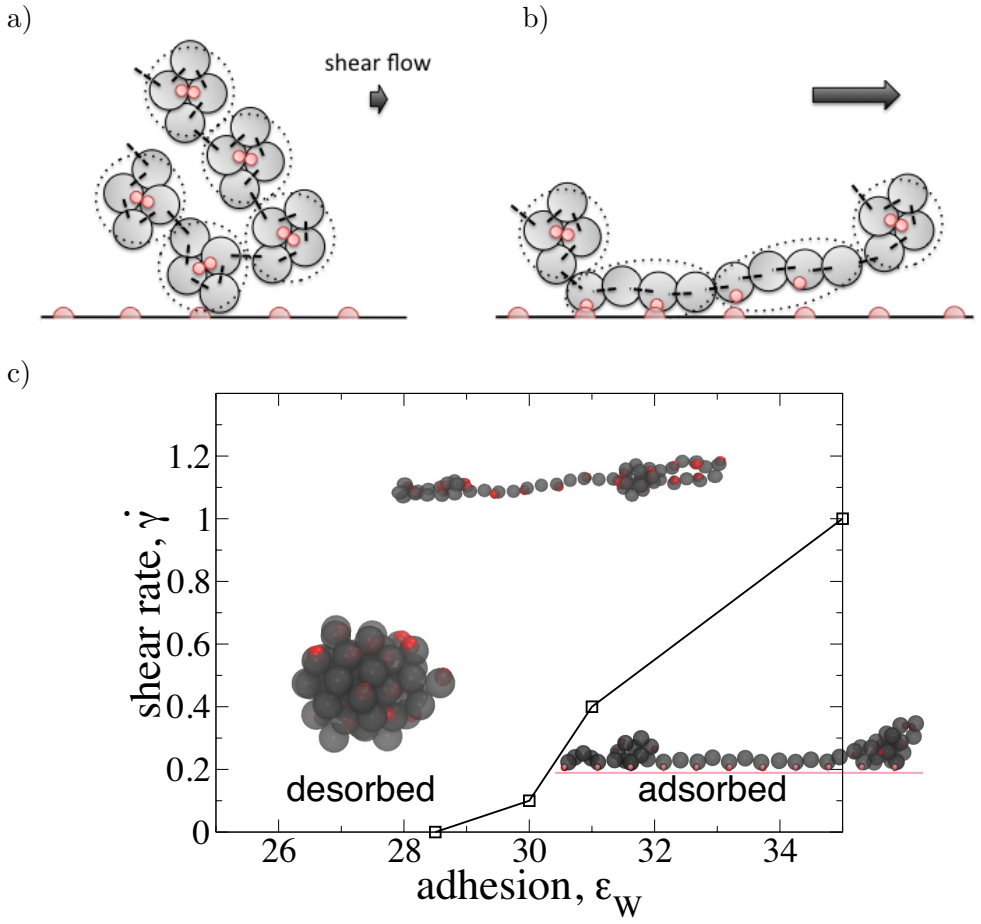

Figure 5.1: a,b) Illustration of a polymer model where the building blocks (encircled by dashed circles or ellipses and corresponding to a VWF dimer) consist of four grey beads, connected to a chain by stiff springs (short dashed lines). Every second monomer has a binding site represented by a small red bead bound to the surface of the monomer. a) At low shear flow, the polymer is collapsed. The binding sites are hidden and cannot attach to the surface binding sites that are indicated by red half beads. b) Only when the monomer bonds break in high shear flow, the binding sites are exposed to the surface and the polymer adsorbs. c) State diagram showing the adsorption transition of a globule with $N = 50$ and cohesive strength $\varepsilon = 2$ where red beads have cohesive strength $\varepsilon_H = 3$. The interaction range between red binding sites is $\sigma_H = 0.5$ and the interaction range with the surface sites is $\sigma_W = 1.5$. Hydrodynamic interactions are neglected. Snapshots in the desorbed region illustrate a globule at low shear rate, where most binding sites are hidden, and an extended conformation at high shear rate, where binding sites are exposed. For high enough adhesion the polymer adsorbs onto the lattice of surface binding sites. For this set of parameters there is no shear-induced adsorption.

and cohesion in the presence of saturating and shielding binding sites under applied shear flow.

In preliminary unpublished work we obtained a state diagram as a function of shear rate and adhesive strength shown in fig. 5.1c. We realized that the choice of the interaction ranges of the cohesive and adhesive binding sites are crucial. For the particular set of cohesive and adhesive range parameters utilized in fig. 5.1c, a very high adhesion ε_W is needed in order to adsorb the polymer, while shear promotes desorption. It will be interesting to explore whether there are values for the interaction ranges, which schematically correspond to the radii of the red and grey beads in fig. 5.1, for which shear induces adsorption. The underlying question being whether bond saturation and bond shielding constitutes a mechanism for shear-induced adsorption of polymer globules, which would be a potential-based alternative to the mechanism based on surface-VWF catch bond behavior. This leads to a number of interesting questions concerning the importance of collective phenomena, for example to what extent collectivity plays a role in the friction-dominated dynamics of a polymer that is adsorbed on an inhomogeneous surface.

5.1.2 First-order transition of polymer collapse induced by reversibly associating hydrophobic molecules

Biopolymers in a number of microbiological situations are known for associating with small proteins or other molecules in order to facilitate transport and thermodynamic behavior. In the context of blood clotting, a physiologically relevant situation concerns the interaction between factor VIII and VWF that tends to adsorb factor VIII and thereby provides transportation and protection against degradation. In preliminary unpublished work in cooperation with Prof. Charles Sing and Prof. Alfredo Alexander-Katz (MIT) we focused on a single VWF interacting with a gas of hydrophobic particles, which mimic a solution of factor VIII particles. We demonstrated that the collapse of a homopolymer under Θ-solvent conditions can be driven by the addition of hydrophobic particles that bind to the chain according to a kinetic two-state model. The added particles interact effectively with each other through the chain connectivity, and induce a first-order polymer collapse transition.

We conducted Brownian dynamics simulations of a polymer with $N = 50$ beads and cohesive strength $\varepsilon = 0.35$ that interacts with a gas of hydrophobic particles of the same size as the monomers but with a larger cohesive strength $\varepsilon_H > \varepsilon$. For interspecies-interaction we used $\sqrt{\varepsilon_H\,\varepsilon}$. Associations between monomers and hydrophobic particles were modeled by two-state reaction kinetics similar to that used in chapter 3 with an energy difference between bound and unbound state set to $\Delta E = 3$ and a catch bond parameter $x = 0.1$. Existing bonds were modeled by a stiff spring, equal to the monomer-connection potential. The concentration of unbound hydrophobic particles is kept constant, i.e. we consider a grand-canonical ensemble.

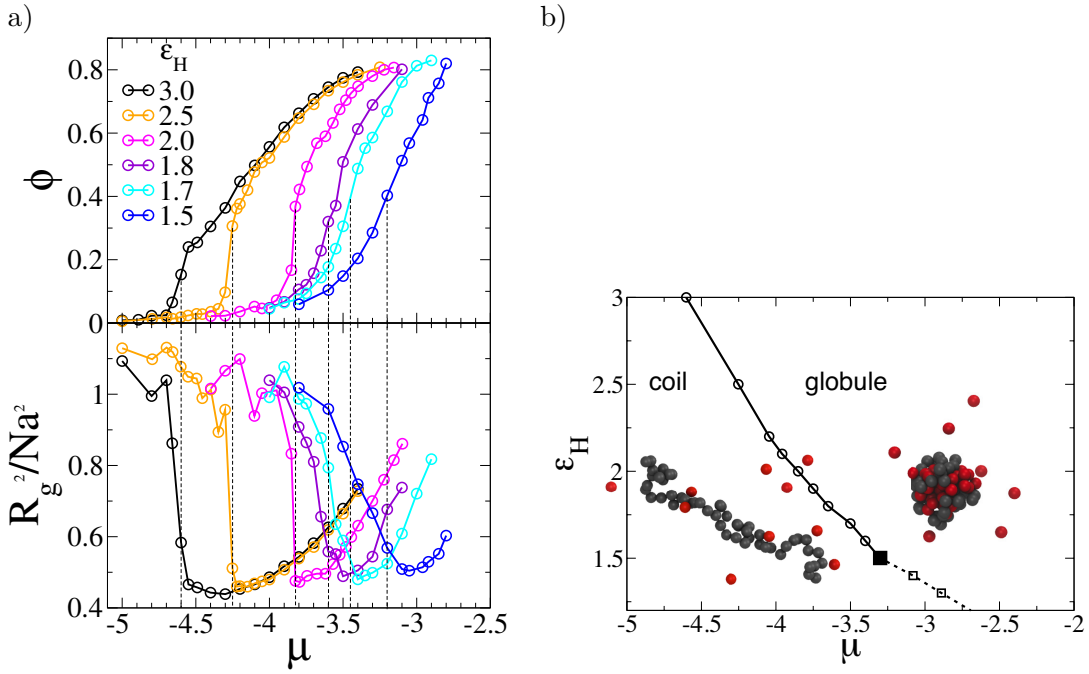

Figure 5.2: a) Fraction of bonded monomers ϕ for varying chemical potential $\mu = \log(\rho)$ of the gas of hydrophobic particles with density ρ for a few different values of hydrophobic particle interaction ε_H. For $\varepsilon_H > 1.7$ there is a jump in ϕ as the chemical potential increases corresponding to a sudden decrease of the rescaled radius of gyration R_g^2/Na^2. The discontinuous transition from a swollen polymer chain to a globular conformation is indicating by vertical dashed lines. Below $\varepsilon_H \approx 1.5$ the transition becomes continuous. b) Phase diagram of the association-induced collapse transition of a single chain. For low values of polymer cohesion ε_H and chemical potential μ of the hydrophobic particles (red), the polymer chain remains in a coiled state, similar to the situation in the absence of binding particles. The boundary to a collapsed conformation is denoted by a solid black line for the discontinuous transition, which changes at the tricritical point (black filled square) to a continuous transition marked by a dashed line.

Results for the average fraction of bonded monomers ϕ and the rescaled squared radius of gyration R_g^2/Na^2 are shown in fig. 5.2a as a function of chemical potential $\mu = \log(\rho)$ for a few values of ε_H. With increasing chemical potential μ (or density ρ) the fraction of bonded monomers suddenly increases while the gyradius decreases in a discontinuous fashion well below the size of a Θ-polymer. The higher the cohesive strength ε_H, the lower is the critical value of μ, indicated in fig. 5.2a by dashed lines. This corresponds to a first-order collapse transition from a coil to a collapsed conformation of the polymer. The corresponding phase diagram is shown in fig. 5.2b including representative snapshots of a swollen polymer coil on the left hand side of the collapse transition, which is denoted by the black line, and, on the right hand side, a collapsed state induced by the addition of the red hydrophobic binders. The discontinuous collapse transition (solid black line) changes at the tricritical point $\varepsilon_H \approx 1.5$ to a continuous transition (dashed black line).

Future work should consider the interplay of binding particles of different size with a polymer in shear flow and near adsorbing surfaces. In the context of biopolymer degradation, it would be interesting to explore how additional binding particles affect the conformational behavior in shear, which might have consequences on the internal tension distribution and thus on the enzymatic cleavage activity.

A

Appendix

A.1 Derivation of homogeneous surface potential

In the following we consider an inhomogeneous surface consisting of a square lattice of discrete binding sites having a distance b, surface interaction range σ_W, and adhesive strength ε_W. The energy potential for N particles interacting with the surface is given by

$$U_{\text{inh}} = \sum_{i,k} \epsilon_W \left(\frac{\sigma_W^{12}}{(\sigma_W + r_{ik})^{12}} - \frac{2\sigma_W^6}{(\sigma_W + r_{ik})^6} \right), \tag{A.1}$$

where r_{ik} is the distance between particle i and binding site k. Using polar coordinates, the contribution of a single particle with the distance $r_{ik} = \sqrt{r^2 + (z - z_W)^2}$ to a single binding site on the surface at $z_W = 2$ is given by

$$u(z, r) = \epsilon_W \left(\frac{\sigma_W^{12}}{(\sigma_W + \sqrt{r^2 + (z - z_W)^2})^{12}} - \frac{2\sigma_W^6}{(\sigma_W + \sqrt{r^2 + (z - z_W)^2})^6} \right). \tag{A.2}$$

In the limit of high binding site density, $\rho_W = 1/b^2 > \sigma_W^{-2}$, we obtain a smooth surface energy term by integration

$$u_{\text{hom}}(z) = \rho_W \int_0^{2\pi} d\phi \int_0^{\infty} dr\, r\; u(z, r). \tag{A.3}$$

With substitution by the variable $r' = \sqrt{r^2 + (z - z_W)^2}$ we obtain

$$\begin{aligned} u_{\text{hom}}(z) &= 2\pi\epsilon_W \rho_W \int_{|z - z_W|}^{\infty} dr' \left(\frac{r' \sigma_W^{12}}{(\sigma_W + r')^{12}} - \frac{2r' \sigma_W^6}{(\sigma_W + r')^6} \right) \\ &= 2\pi\epsilon_W \rho_W \left[\frac{\sigma_W^{12}(11r' + \sigma_W)}{110(r' + \sigma_W)^{11}} - \frac{2\sigma_W^6(5r' + \sigma_W)}{20(r' + \sigma_W)^5)} \right]_{|z - z_W|} \\ &= \frac{\pi}{5} \epsilon_W \rho_W \sigma_W^2 \left(\frac{(11|z - z_W| + \sigma_W)\sigma_W^{10}}{11(|z - z_W| + \sigma_W)^{11}} - \frac{(5|z - z_W| + \sigma_W)\sigma_W^4}{(|z - z_W| + \sigma_W)^5} \right) \end{aligned} \tag{A.4}$$

The full homogeneous potential energy is obtained by summation over all particles,

$$U_{\text{hom}} = \sum_i \frac{\pi}{5} \varepsilon_W \rho_W \sigma_W^2 \left(\frac{(11|z_i - 2| + \sigma_W)\, \sigma_W^{10}}{11\, (\sigma_W + |z_i - 2|)^{11}} - \frac{(5|z_i - 2| + \sigma_W)\, \sigma_W^4}{(\sigma_W + |z_i - 2|)^5} \right). \tag{A.5}$$

A.2 Mean first passage time for one-dimensional Smoluchowski equation

For a one-dimensional process described by a Smoluchowski equation, the mean first passage time in a potential $U(y)$ out of the interval $[a, b]$ is a solution of the differential equation [130]

$$-D\,U'(y)t'(y) + \frac{D}{\beta}\,t''(y) = -1, \tag{A.6}$$

with the diffusion constant $D = \mu_0\,\mathrm{kT}$ and $\beta = 1/\mathrm{kT}$. The particle is injected at the position $y_{\min}$ and the boundary conditions are absorbing, $t(a) = 0$ and $t(b) = 0$. Multiplying eq. (A.6) by $e^{-\beta U(y)}$ and integration leads to

$$\begin{aligned} -D\int_a^y e^{-\beta U(\bar{y})}U'(\bar{y})t'(y)d\bar{y} + \frac{D}{\beta}\int_a^y e^{-\beta U(\bar{y})}t''(\bar{y})d\bar{y} &= -\int_a^y e^{-\beta U(\bar{y})}d\bar{y} \\ \frac{D}{\beta}\int_a^y \frac{d}{d\bar{y}}\left[e^{-\beta U(\bar{y})}t'(\bar{y})\right]d\bar{y} &= -\int_a^y e^{-\beta U(\bar{y})}d\bar{y} \\ \frac{D}{\beta}\left[e^{-\beta U(y)}t'(y) - e^{-\beta U(a)}t'(a)\right] &= -\int_a^y e^{-\beta U(\bar{y})}d\bar{y}. \end{aligned} \tag{A.7}$$

By integration of eq. (A.7) from $y = a$ to $y = y_{\min}$ and using the absorbing boundary condition we obtain

$$\begin{aligned} \int_a^{y_{\min}} t'(y)dy &= \int_a^{y_{\min}} e^{\beta U(y)}e^{-\beta U(a)}t'(a)dy - \frac{\beta}{D}\int_a^{y_{\min}} e^{\beta U(y)}\int_a^y e^{-\beta U(\bar{y})}d\bar{y}dy \\ t(y_{\min}) &= e^{-\beta U(a)}t'(a)\int_a^{y_{\min}} e^{\beta U(y)}dy - \frac{\beta}{D}\int_a^{y_{\min}} e^{\beta U(y)}\int_a^y e^{-\beta U(\bar{y})}d\bar{y}dy. \end{aligned} \tag{A.8}$$

On the other hand, integration of eq. (A.7) from $y = a$ to $y = b$,

$$\int_a^b t'(y)dy = \int_a^b e^{\beta U(y)}e^{-\beta U(a)}t'(a)dy - \frac{\beta}{D}\int_a^b e^{\beta U(y)}\int_a^y e^{-\beta U(\bar{y})}d\bar{y}dy, \tag{A.9}$$

yields

$$-e^{-\beta U(a)}t'(a) = -\frac{\beta}{D}\frac{\int_a^b e^{\beta U(y)}\int_a^y e^{-\beta U(\bar{y})}d\bar{y}dy}{\int_a^b e^{\beta U(y)}dy} \tag{A.10}$$

Thus, using eq. (A.8) and eq. (A.10), we obtain the theoretical result for the mean first passage time $\tau_{\mathrm{mfpt}} = t(y_{\min})$ to hit either of the two absorbing boundaries at $y = a$ and $y = b$, starting in the minimum at $y_{\min} \in [a, b]$, given by

$$\begin{aligned} \tau_{\mathrm{mfpt}} = \frac{\beta}{D}\frac{\int_a^b e^{\beta U(y)}\int_a^y e^{-\beta U(\bar{y})}d\bar{y}dy}{\int_a^b e^{\beta U(y)}dy}\int_a^{y_{\min}} e^{\beta U(y)}dy \\ -\frac{\beta}{D}\int_a^{y_{\min}} e^{\beta U(y)}\int_a^y e^{-\beta U(\bar{y})}d\bar{y}dy. \end{aligned} \tag{A.11}$$

A.3 Mobility in one-dimensional periodic potential

We consider the motion of a single Brownian particle in the one-dimensional, corrugated, and periodic potential $U_{\mathrm{inh}}(y)$ and under the influence of an external force f_{ext}; the total potential reads $U(y) = U_{\mathrm{inh}}(y) - y\, f_{\mathrm{ext}}$. The corresponding stationary Fokker-Planck equation for the probability density $P(y,t)$ is given in a dimensionless form by

$$\frac{\partial}{\partial t}P(y,t) = \frac{\partial}{\partial y}\left(\frac{\partial U(y)}{\partial y} + \frac{\partial}{\partial y}\right)P(y,t) = 0. \tag{A.12}$$

For the time-independent potential $U(y)$ that consists of a linear part and a periodic contribution $U_{\mathrm{inh}}(y) = U_{\mathrm{inh}}(y+b)$, the exact solution [131] of eq. (A.12) is given by

$$P(y) = \frac{e^{-U(y)}}{Q}\left[\frac{\int_0^b e^{U(\bar{y})}d\bar{y}}{1-e^{-bf_{\mathrm{ext}}}} - \int_0^y e^{U(\bar{y})}d\bar{y}\right] \tag{A.13}$$

with normalization constant

$$Q = \frac{\int_0^b e^{-U(y)}dy \int_0^b e^{U(\bar{y})}d\bar{y}}{1-e^{-bf_{\mathrm{ext}}}} - \int_0^b e^{-U(y)}\int_0^y e^{U(\bar{y})}d\bar{y}dy. \tag{A.14}$$

The rescaled mobility follows as

$$\mu = \frac{\tilde{\mu}}{\mu_0} = \frac{\langle\dot{y}\rangle}{f_{\mathrm{ext}}} = \frac{1}{f_{\mathrm{ext}}}\int_0^b \dot{y}\,P(y)dy = \frac{1}{f_{\mathrm{ext}}}\int_0^b -\frac{\partial U(y)}{\partial y}P(y)dy, \tag{A.15}$$

where the overdamped Langevin equation has been used to substitute the particle velocity $\dot{y} = -\partial_y U(y) + \xi$; the average of the random force term ξ vanishes. By partial integration of eq. (A.15) we obtain

$$\begin{aligned}
\mu &= \frac{1}{f_{\mathrm{ext}}}\int_0^b -\frac{\partial U(y)}{\partial y}\frac{e^{-U(y)}}{Q}\left[\frac{\int_0^b e^{U(\bar{y})}d\bar{y}}{1-e^{-bf_{\mathrm{ext}}}} - \int_0^y e^{U(\bar{y})}d\bar{y}\right]dy \\
&= \frac{1}{Qf_{\mathrm{ext}}}\int_0^b \frac{\partial}{\partial y}\left(e^{-U(y)}\right)\left[\frac{\int_0^b e^{U(\bar{y})}d\bar{y}}{1-e^{-bf_{\mathrm{ext}}}} - \int_0^y e^{U(\bar{y})}d\bar{y}\right]dy \\
&= \frac{1}{Qf_{\mathrm{ext}}}\left[\frac{\int_0^b e^{U(\bar{y})}d\bar{y}}{1-e^{U(b)-U(0)}}\left(e^{-U(b)}-e^{-U(0)}\right) - e^{-U(b)}\int_0^b e^{U(\bar{y})}d\bar{y} + \int_0^b e^{-U(y)}e^{U(y)}dy\right] \\
&= \frac{1}{Qf_{\mathrm{ext}}}\left[\frac{e^{-U(b)}-e^{-U(0)}-e^{-U(b)}\left(1-e^{U(b)-U(0)}\right)}{1-e^{U(b)-U(0)}}\int_0^b e^{U(\bar{y})}d\bar{y} + b\right] \\
&= \frac{b}{Qf_{\mathrm{ext}}}
\end{aligned} \tag{A.16}$$

and thus, using eq. (A.14), the mobility is given by

$$\begin{aligned}
\mu = \frac{b\left(1-e^{-bf_{\mathrm{ext}}}\right)}{f_{\mathrm{ext}}}\Bigg[&\int_0^b e^{-U(y)}dy\int_0^b e^{U(y)}dy \\
&- \left(1-e^{-bf_{\mathrm{ext}}}\right)\int_0^b\int_0^y e^{-U(y)+U(\bar{y})}d\bar{y}dy\Bigg]^{-1}
\end{aligned} \tag{A.17}$$

Within linear response, i.e. for $f_{\text{ext}} \to 0$, the double integral term vanishes and the mobility reads

$$\mu = b \left[\int_0^b e^{-U_{\text{inh}}(y)} dy \int_0^b e^{U_{\text{inh}}(y)} dy \right]^{-1} \tag{A.18}$$

A.4 Rotation and diffusion of globular polymer

In order to determine the angular velocity of a globular polymer, we consider the velocities of single beads within the time interval Δ defined by

$$\mathbf{v}_i = (\mathbf{r}'_i - \mathbf{r}_i)/\Delta, \tag{A.19}$$

where the the center-of-mass motion is removed,

$$\mathbf{r}_i = \mathbf{r}_i(t) - \sum_j \mathbf{r}_j(t)/N \tag{A.20}$$

$$\mathbf{r}'_i = \mathbf{r}_i(t+\Delta) - \sum_j \mathbf{r}_j(t+\Delta)/N. \tag{A.21}$$

The average angular velocity with respect to the y-axis is then defined by

$$w = \langle L_y/J_y \rangle \tag{A.22}$$

$$= \left\langle \frac{\sum_i^N (\mathbf{r}_i \times \mathbf{v}_i) \cdot \hat{\mathbf{y}}}{\sum_i^N ((\mathbf{r}_i \cdot \hat{\mathbf{x}})^2 + (\mathbf{r}_i \cdot \hat{\mathbf{z}})^2)} \right\rangle \tag{A.23}$$

$$= \left\langle \frac{\sum_i^N (\mathbf{r}_i \times \mathbf{r}'_i) \cdot \hat{\mathbf{y}}/\Delta}{\sum_i^N ((\mathbf{r}_i \cdot \hat{\mathbf{x}})^2 + (\mathbf{r}_i \cdot \hat{\mathbf{z}})^2)} \right\rangle, \tag{A.24}$$

where hats denote unit vectors in the corresponding direction.

A homopolymer forms for large cohesion a compact spherical object, which rotates in unbound linear shear flow with a frequency similar to the prediction for a solid perfect sphere, $\omega = \dot{\gamma}/2$. This is shown in Fig. A.1a, where we plot the rescaled angular velocity, eq. (A.24), of a globule in constant shear flow $\dot{\gamma} = 1$ as a function of the cohesion ε. Simulations are performed as described in Section 2.2.

The effective translational mobility as obtained from simulations of globules under constant force is shown in Fig. A.1b as black circles and compares well with the corresponding Stokes mobility of a homogeneous sphere of radius $R = \sqrt{5/3} R_g$, where R_g denotes the globule radius of gyration. Since the size of a compact globule scales as $R \sim R_g \sim aN^{1/3}$, the mobility according to the Stokes law scales as $\mu \sim 1/R \sim N^{-1/3}$, as denoted by the solid straight line in Fig. A.1b.

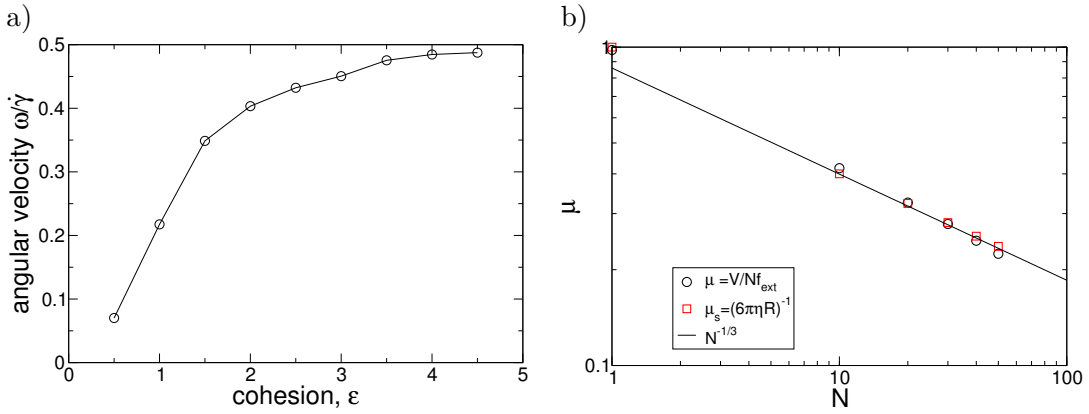

Figure A.1: a) The rescaled angular velocity $\omega/\dot{\gamma}$ approaches the prediction for a hard sphere in shear flow, $\omega = \dot{\gamma}/2$, as the cohesion ε increases. Here, we used a moderate shear rate of $\dot{\gamma} = 1$. b) By applying a constant rescaled force $f_{\text{ext}} = 1$ to all monomers, the effective mobility $\mu = V/Nf_{\text{ext}}$ of a highly compact globule with adhesion $\varepsilon_W = 3$ is obtained from the average center-of-mass velocity $V = \langle|\mathbf{r}_{\text{com}}(t+\Delta) - \mathbf{r}_{\text{com}}(t)|/\Delta\rangle$ as a function of chain length N, it agrees well with the Stokes mobility $\mu_s = 1/6\pi\eta R$ of a homogeneous sphere with radius R. The effective sphere radius R is obtained from the radius of gyration R_g via the relation $R = \sqrt{5/3}R_g$ valid for a compact solid sphere.

A.5 Tension of dimer in shear flow

We consider the simple case of a rotating dimer in shear flow and measure the average tension $f = f_{i=1}$ as a function of shear rate $\dot{\gamma}$. The potential energy U is given by eq. (4.3) with $N = 2$ and cohesive strength $\varepsilon = 2$. Results from Brownian dynamics simulations based on the Langevin eq. (4.1) are shown in fig. A.2 for free draining (FD) as well as hydrodynamic simulations (HI) and are rescaled by the average equilibrium tension $f_0 = f(\dot{\gamma} = 0) \approx 1.52$, which is calculate according to the Boltzmann distribution,

$$f_0 = \frac{\int_0^\infty e^{-U(r)}\kappa(r-2)d\mathbf{r}}{\int e^{-U(r)}d\mathbf{r}}. \tag{A.25}$$

For simulations including hydrodynamic interaction we obtain the scaling behavior $f - f_0 \sim \dot{\gamma}^{0.9}$; free draining simulation results exhibit a linear scaling with the shear rate, $f - f_0 \sim \dot{\gamma}^{1.0}$. We remark that a much simpler model, the harmonic dumbbell with the potential $U_{\text{harm}} = \frac{\kappa}{2}R^2$, with the connecting vector $R = r_{1,2}$, can be evaluated analytically [46]. Without hydrodynamic interactions and neglected excluded volume interactions, the average squared extension of a harmonic dumbbell in linear shear flow is given by

$$\left\langle R^2 \right\rangle = \frac{3}{\kappa} + \frac{\dot{\gamma}^2}{(2\kappa)^3}. \tag{A.26}$$

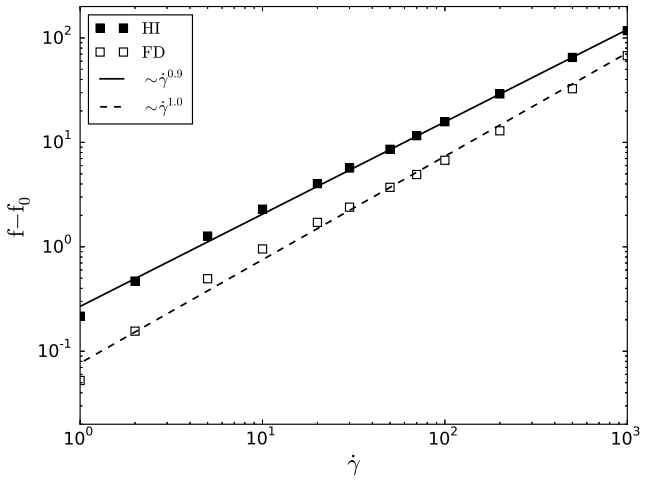

Figure A.2: Average tensile force f between a dimer with $\varepsilon = 2$ as a function of shear rate $\dot{\gamma}$; the tension at zero shear f_0, eq. (A.25), is substracted. Open symbols are results for free draining simulations, closed symbols include hydrodynamic interactions between the two beads. The force scales linear with shear rate in FD case (dashed line) and almost linear for HI (solid line), $f \sim \dot{\gamma}^{0.9}$.

This gives a hint for the shear dependence of the tensile force $f \sim \langle R \rangle \sim \sqrt{\langle R^2 \rangle} \sim \dot{\gamma}$, as seen in fig. A.2 for simulations using the potential eq. (4.3).

List of Publications

The present thesis is based on the following manuscripts, which have been published in peer-reviewed journals:

[i] Matthias Radtke and Roland R. Netz. Shear-induced dynamics of polymeric globules at adsorbing homogeneous and inhomogeneous surfaces. *The European Physical Journal E*, 37(3):20, March 2014.

[ii] Matthias Radtke and Roland R. Netz. Shear-enhanced adsorption of a homopolymeric globule mediated by surface catch bonds. *The European Physical Journal E*, 38(6):69, June 2015.

[iii] Svenja Lippok, Matthias Radtke, Tobias Obser, Lars Kleemeier, Reinhard Schneppenheim, Ulrich Budde, Roland R. Netz, and Joachim O. Rädler. Shear-induced unfolding and enzymatic cleavage of full-length VWF multimers *Biophysical Journal*, 100(3):545-554, February 2016.

[iv] Matthias Radtke, Svenja Lippok, Joachim O. Rädler, and Roland R. Netz. Internal tension in a collapsed polymer under shear flow and the connection to enzymatic cleavage of von Willebrand factor *The European Physical Journal E*, 39(32), April 2016.

Bibliography

[1] A. Y. Grosberg. *Statistical physics of macromolecules*. AIP series in polymers and complex materials. AIP Press, New York, 1994.

[2] Michael Rubinstein. *Polymer physics*. Oxford University Press, New York, 2003.

[3] M. Doi and S. F. Edwards. *The theory of polymer dynamics*, volume 73. Oxford University Press, 1988.

[4] R. G. Larson. The rheology of dilute solutions of flexible polymers: Progress and problems. *J. Rheol.*, 49(1):1–70, January 2005.

[5] Philippe Cordier, François Tournilhac, Corinne Soulié-Ziakovic, and Ludwik Leibler. Self-healing and thermoreversible rubber from supramolecular assembly. *Nature*, 451(7181):977–980, February 2008.

[6] Aaron M Kushner and Zhibin Guan. Modular design in natural and biomimetic soft materials. *Angew. Chem. Int. Ed.*, 50(39):9026–9057, 2011.

[7] Alfredo Alexander-Katz. Toward novel polymer-based materials inspired in blood clotting. *Macromolecules*, 47(5):1503–1513, March 2014.

[8] Hsieh Chen and Alfredo Alexander-Katz. Structure and dynamics of blood-clotting-inspired polymer-colloid composites. *Soft Matter*, 9(43):10381, 2013.

[9] W. E. Thomas, V. Vogel, and E. Sokurenko. Biophysics of catch bonds. *Annu. Rev. Biophys.*, 37(1):399–416, June 2008.

[10] Innocent B. Bekard, Peter Asimakis, Joseph Bertolini, and Dave E. Dunstan. The effects of shear flow on protein structure and function. *Biopolymers*, 95(11):733–745, 2011.

[11] J. Evan Sadler. Biochemistry and genetics of von Willebrand factor. *Annu. Rev. Biochem.*, 67(1):395–424, 1998.

[12] Zaverio M. Ruggeri. Structure of von Willebrand factor and its function in platelet adhesion and thrombus formation. *Best. Pract. Rres. Cl. Ha.*, 14(2):257–279, June 2001.

[13] Augusto B. Federici. The factor VIII/von Willebrand factor complex: basic and clinical issues. *Haematologica*, 88(6):EREP02, June 2003.

[14] Denisa D. Wagner. Cell biology of von Willebrand factor. *Annu. Rev. Cell Biol.*, 6(1):217–242, 1990.

[15] T. Nightingale and D. Cutler. The secretion of von Willebrand factor from endothelial cells; an increasingly complicated story. *J. Thromb. Haemost.*, 11:192–201, June 2013.

[16] Volker Huck, Matthias F. Schneider, Christian Gorzelanny, and Stefan W. Schneider. The various states of von Willebrand factor and their function in physiology and pathophysiology. *Thromb. Haemost.*, 111(4):598–609, April 2014.

[17] M. Zhou, X. Dong, C. Baldauf, H. Chen, Y. Zhou, T. A. Springer, X. Luo, C. Zhong, F. Grater, and J. Ding. A novel calcium-binding site of von Willebrand factor A2 domain regulates its cleavage by ADAMTS13. *Blood*, 117(17):4623–4631, April 2011.

[18] Weiqiang Gao, Patricia J. Anderson, Elaine M. Majerus, Elodee A. Tuley, and J. Evan Sadler. Exosite interactions contribute to tension-induced cleavage of von Willebrand factor by the antithrombotic ADAMTS13 metalloprotease. *Proc. Natl. Acad. Sci.*, 103(50):19099–19104, December 2006.

[19] C. Baldauf, R. Schneppenheim, W. Stacklies, T. Obser, A. Pieconka, S. Schneppenheim, U. Budde, J. Zhou, and F. Gräter. Shear-induced unfolding activates von Willebrand factor A2 domain for proteolysis. *J. Thromb. Haemost.*, 7(12):2096–2105, December 2009.

[20] Svenja Lippok, Tobias Obser, Jochen P. Müller, Valentin K. Stierle, Martin Benoit, Ulrich Budde, Reinhard Schneppenheim, and Joachim O. Rädler. Exponential size distribution of von Willebrand factor. *Biophys. J.*, 105(5):1208–1216, September 2013.

[21] Ulrich Budde and Reinhard Schneppenheim. Von Willebrand factor and von Willebrand disease. *Rev. Clin. Exp. Hematol.*, 5(4):335–368, December 2001.

[22] J. Evan Sadler. New concepts in von Willebrand disease. *Annu. Rev. Med.*, 56(1):173–191, February 2005.

[23] J. E. Sadler. Von Willebrand factor, ADAMTS13, and thrombotic thrombocytopenic purpura. *Blood*, 112(1):11–18, February 2008.

[24] Y.-F. Zhou, E. T. Eng, J. Zhu, C. Lu, T. Walz, and T. A. Springer. Sequence and structure relationships within von Willebrand factor. *Blood*, 120(2):449–458, July 2012.

[25] Eric G. Huizinga, Shizuko Tsuji, Roland A. P. Romijn, Marion E. Schiphorst, Philip G. de Groot, Jan J. Sixma, and Piet Gros. Structures of glycoprotein Ibalpha and its complex with von Willebrand factor A1 domain. *Science*, 297(5584):1176–1179, August 2002.

[26] Miguel A. Cruz, Huabing Yuan, Joseph R. Lee, Robert J. Wise, and Robert I. Handin. Interaction of the von Willebrand factor (vWF) with collagen. localization of the primary collagen-binding site by analysis of recombinant vWF a domain polypeptides. *J. Biol. Chem.*, 270(18):10822–10827, May 1995.

[27] T. A. Springer. Biology and physics of von Willebrand factor concatamers. *J. Thromb. Haemost.*, 9:130–143, July 2011.

[28] W E Fowler, L J Fretto, K K Hamilton, H P Erickson, and P A McKee. Substructure of human von Willebrand factor. *J. Clin. Invest.*, 76(4):1491–1500, October 1985.

[29] I. Singh, H. Shankaran, M. E. Beauharnois, Z. Xiao, P. Alexandridis, and S. Neelamegham. Solution structure of human von Willebrand factor studied using small angle neutron scattering. *J. Biol. Chem.*, 281(50):38266–38275, December 2006.

[30] George A Truskey, Fan Yuan, and David F Katz. *Transport phenomena in biological systems*. Pearson/Prentice Hall, Upper Saddle River, N.J., 2004.

[31] S. W. Schneider, S. Nuschele, A. Wixforth, C. Gorzelanny, A. Alexander-Katz, R. R. Netz, and M. F. Schneider. Shear-induced unfolding triggers adhesion of von Willebrand factor fibers. *Proc. Natl. Acad. Sci.*, 104(19):7899–7903, 2007.

[32] B. Furie and B. C. Furie. Molecular and cellular biology of blood coagulation. *N. Engl. J. Med.*, 326(12):800–806, March 1992.

[33] Alfred Link and Juergen Springer. Light scattering from dilute polymer solutions in shear flow. *Macromolecules*, 26(3):464–471, 1993.

[34] Rahul Roy, Sungchul Hohng, and Taekjip Ha. A practical guide to single-molecule FRET. *Nat. Methods*, 5(6):507–516, June 2008.

[35] Nils G Walter, Cheng-Yen Huang, Anthony J Manzo, and Mohamed A Sobhy. Do-it-yourself guide: how to use the modern single-molecule toolkit. *Nat. Methods*, 5(6):475–489, June 2008.

[36] Ido Golding and Edward C. Cox. Physical nature of bacterial cytoplasm. *Phys. Rev. Lett.*, 96(9):098102, March 2006.

[37] Douglas Magde, Elliot Elson, and W. W. Webb. Thermodynamic fluctuations in a reacting System—Measurement by fluorescence correlation spectroscopy. *Phys. Rev. Lett.*, 29(11):705–708, September 1972.

[38] R. Rigler, Ü. Mets, J. Widengren, and P. Kask. Fluorescence correlation spectroscopy with high count rate and low background: analysis of translational diffusion. *Eur. Biophys. J.*, 22(3), August 1993.

[39] Hanna Engelke, Ingmar Dorn, and Joachim O. Rädler. Diffusion and molecular binding in crowded vesicle solutions measured by fluorescence correlation spectroscopy. *Soft Matter*, 5(21):4283, 2009.

[40] Keir C. Neuman and Attila Nagy. Single-molecule force spectroscopy: optical tweezers, magnetic tweezers and atomic force microscopy. *Nat. Methods*, 5(6):491–505, June 2008.

[41] Pierre-Gilles De Gennes. *Scaling concepts in polymer physics*. Cornell University Press, 1979.

[42] Paul J Flory. *Principles of polymer chemistry*. Cornell University Press, 1953.

[43] Prince E. Rouse. A theory of the linear viscoelastic properties of dilute solutions of coiling polymers. *J. Chem. Phys.*, 21(7):1272, 1953.

[44] Bruno H. Zimm. Dynamics of polymer molecules in dilute solution: Viscoelasticity, flow birefringence and dielectric loss. *J. Chem. Phys.*, 24(2):269, 1956.

[45] P. G. De Gennes. Coil-stretch transition of dilute flexible polymers under ultrahigh velocity gradients. *J. Chem. Phys.*, 60(12):5030, 1974.

[46] A. Puliafito and K. Turitsyn. Numerical study of polymer tumbling in linear shear flows. *Physica D*, 211(1-2):9–22, November 2005.

[47] A Celani, A Puliafito, and K Turitsyn. Polymers in linear shear flow: A numerical study. *Europhys. Lett.*, 70(4):464–470, May 2005.

[48] Hongbo Ma and Michael D. Graham. Theory of shear-induced migration in dilute polymer solutions near solid boundaries. *Phys. Fluids*, 17(8):083103, 2005.

[49] Douglas E. Smith, Hazen P. Babcock, and Steven Chu. Single-polymer dynamics in steady shear flow. *Science*, 283(5408):1724–1727, March 1999.

[50] Charles Schroeder, Rodrigo Teixeira, Eric Shaqfeh, and Steven Chu. Characteristic periodic motion of polymers in shear flow. *Phys. Rev. Lett.*, 95(1), July 2005.

[51] C. Sendner and R. R. Netz. Single flexible and semiflexible polymers at high shear: Non-monotonic and non-universal stretching response. *Eur. Phys. J. E*, 30(1):75–81, September 2009.

[52] T. T. Perkins. Single polymer dynamics in an elongational flow. *Science*, 276(5321):2016–2021, June 1997.

[53] C. M. Schroeder. Observation of polymer conformation hysteresis in extensional flow. *Science*, 301(5639):1515–1519, September 2003.

[54] C. E. Sing and A. Alexander-Katz. Elongational flow induces the unfolding of von Willebrand factor at physiological flow rates. *Biophys. J.*, 98(9):L35–L37, May 2010.

[55] P. S. Doyle, B. Ladoux, and J. L. Viovy. Dynamics of a tethered polymer in shear flow. *Phys. Rev. Lett.*, 84(20):4769–4772, May 2000.

[56] Juan Jaspe and Stephen J. Hagen. Do protein molecules unfold in a simple shear flow? *Biophys. J.*, 91(9):3415–3424, November 2006.

[57] P. Szymczak and Marek Cieplak. Proteins in a shear flow. *J. Chem. Phys.*, 127(15):155106, 2007.

[58] A. Alexander-Katz, M. F. Schneider, S. Schneider, A. Wixforth, and R. R. Netz. Shear-flow-induced unfolding of polymeric globules. *Phys. Rev. Lett.*, 97(13):138101, September 2006.

[59] A. Halperin and E. B. Zhulina. On the deformation behaviour of collapsed polymers. *Europhys. Lett.*, 15(4):417, June 1991.

[60] A. Buguin and F. Brochard-Wyart. Unwinding of globular polymers under strong flows. *Macromolecules*, 29(14):4937–4943, January 1996.

[61] A. Alexander-Katz and R. R. Netz. Dynamics and instabilities of collapsed polymers in shear flow. *Macromolecules*, 41(9):3363–3374, May 2008.

[62] A. Alexander-Katz and R. R. Netz. Surface-enhanced unfolding of collapsed polymers in shear flow. *Europhys. Lett.*, 80(1):18001, October 2007.

[63] Y. von Hansen, M. Hinczewski, and R. R. Netz. Hydrodynamic screening near planar boundaries: Effects on semiflexible polymer dynamics. *J. Chem. Phys.*, 134(23):235102, 2011.

[64] A. Milchev and K. Binder. Static and dynamic properties of adsorbed chains at surfaces: Monte Carlo simulation of a bead-spring model. *Macromolecules*, 29(1):343–354, 1996.

[65] Ajay S. Panwar and Satish Kumar. Brownian dynamics simulations of polyelectrolyte adsorption in shear flow. *J. Chem. Phys.*, 122(15):154902, 2005.

[66] N. Hoda and S. Kumar. Brownian dynamics simulations of polyelectrolyte adsorption in shear flow with hydrodynamic interaction. *J. Chem. Phys.*, 127(23):234902, 2007.

[67] G.-L. He, R. Messina, and H. Löwen. Statistics of polymer adsorption under shear flow. *J. Chem. Phys.*, 132(12):124903, 2010.

[68] A. Serr, C. Sendner, F. Müller, T. R. Einert, and R. R. Netz. Single-polymer adsorption in shear: Flattening vs. hydrodynamic lift and surface potential corrugation effects. *Europhys. Lett.*, 92(3):38002, November 2010.

[69] M. Möddel, W. Janke, and M. Bachmann. Comparison of the adsorption transition for grafted and nongrafted polymers. *Macromolecules*, 44(22):9013–9019, November 2011.

[70] Lin Fang, Hua Hu, and Ronald G. Larson. DNA configurations and concentration in shearing flow near a glass surface in a microchannel. *J. Rheol.*, 49(1):127, 2005.

[71] Gui-Li He, René Messina, Hartmut Löwen, Anton Kiriy, Vera Bocharova, and Manfred Stamm. Shear-induced stretching of adsorbed polymer chains. *Soft Matter*, 5(16):3014, 2009.

[72] P. G. De Gennes. Polymer solutions near an interface. adsorption and depletion layers. *Macromolecules*, 14(6):1637–1644, November 1981.

[73] E. Eisenriegler, K. Kremer, and K. Binder. Adsorption of polymer chains at surfaces: Scaling and Monte Carlo analyses. *J. Chem. Phys.*, 77(12):6296, 1982.

[74] R. R. Netz and D. Andelman. Neutral and charged polymers at interfaces. *Phys. Rep.*, 380(1-2):1–95, June 2003.

[75] N. Hoda and S. Kumar. Brownian dynamics simulations of polyelectrolyte adsorption in shear flow: Effects of solvent quality and charge patterning. *J. Chem. Phys.*, 128(16):164907, 2008.

[76] C. E. Sing, J. G. Selvidge, and A. Alexander-Katz. Von Willebrand adhesion to surfaces at high shear rates is controlled by long-lived bonds. *Biophys. J.*, 105(6):1475–1481, September 2013.

[77] A. J. Goldman, R. G. Cox, and H. Brenner. Slow viscous motion of a sphere parallel to a plane wall—I motion through a quiescent fluid. *Chem. Eng. Sci.*, 22(4):637–651, April 1967.

[78] Udo Seifert. Hydrodynamic lift on bound vesicles. *Phys. Rev. Lett.*, 83(4):876–879, July 1999.

[79] Jeffrey R. Smart and David T. Leighton. Measurement of the drift of a droplet due to the presence of a plane. *Phys. Fluids A*, 3(1):21–28, January 1991.

[80] B. Lorz, R. Simson, J. Nardi, and E. Sackmann. Weakly adhering vesicles in shear flow: Tanktreading and anomalous lift force. *Europhys. Lett.*, 51(4):468, August 2000.

[81] Sreejith Sukumaran and Udo Seifert. Influence of shear flow on vesicles near a wall: A numerical study. *Phy. Rev. E*, 64(1), June 2001.

[82] Y.-L. Chen, M. D. Graham, J. J. de Pablo, K. Jo, and D. C. Schwartz. DNA molecules in microfluidic oscillatory flow. *Macromolecules*, 38(15):6680–6687, 2005.

[83] O. Berk Usta, Jason E. Butler, and Anthony J. C. Ladd. Transverse migration of a confined polymer driven by an external force. *Phys. Rev. Lett.*, 98(9), February 2007.

[84] C. Sendner and R. R. Netz. Shear-induced repulsion of a semiflexible polymer from a wall. *Europhys. Lett.*, 81(5):54006, March 2008.

[85] Z. M. Ruggeri. von Willebrand factor. *J. Clin. Invest.*, 99(4):559, 1997.

[86] Tadayuki Yago, Jizhong Lou, Tao Wu, Jun Yang, Jonathan J. Miner, Leslie Coburn, Jose A. Lopez, Miguel A. Cruz, Jing-Fei Dong, Larry V. McIntire, Rodger P. McEver, and Cheng Zhu. Platelet glycoprotein Ibα forms catch bonds with human WT vWF but not with type 2B von Willebrand disease vWF. *J. Clin. Invest.*, 118(9):3195–3207, September 2008.

[87] Jongseong Kim, Cheng-Zhong Zhang, Xiaohui Zhang, and Timothy A. Springer. A mechanically stabilized receptor–ligand flex-bond important in the vasculature. *Nature*, 466(7309):992–995, August 2010.

[88] G. Bell. Models for the specific adhesion of cells to cells. *Science*, 200(4342):618–627, May 1978.

[89] Evgeni V. Sokurenko, Viola Vogel, and Wendy E. Thomas. Catch-bond mechanism of force-enhanced adhesion: Counterintuitive, elusive, but ... widespread? *Cell Host Microbe*, 4(4):314–323, October 2008.

[90] M. Dembo, D. C. Torney, K. Saxman, and D. Hammer. The reaction-limited kinetics of membrane-to-surface adhesion and detachment. *Proc. R. Soc. Lond., B, Biol. Sci.*, 234(1274):55–83, June 1988.

[91] Bryan T. Marshall, Mian Long, James W. Piper, Tadayuki Yago, Rodger P. McEver, and Cheng Zhu. Direct observation of catch bonds involving cell-adhesion molecules. *Nature*, 423(6936):190–193, May 2003.

[92] E. Evans, A. Leung, V. Heinrich, and C. Zhu. Mechanical switching and coupling between two dissociation pathways in a P-selectin adhesion bond. *Proc. Natl. Acad. Sci.*, 101(31):11281–11286, August 2004.

[93] K. K. Sarangapani, T. Yago, A. G. Klopocki, M. B. Lawrence, C. B. Fieger, S. D. Rosen, R. P. McEver, and C. Zhu. Low force decelerates L-selectin dissociation from P-selectin glycoprotein ligand-1 and endoglycan. *J. Biol. Chem.*, 279(3):2291–2298, January 2004.

[94] Michael T. Beste and Daniel A. Hammer. Selectin catch–slip kinetics encode shear threshold adhesive behavior of rolling leukocytes. *Proc. Natl. Acad. Sci.*, 105(52):20716–20721, 2008.

[95] R. P. McEver and C. Zhu. Rolling cell adhesion. *Annu. Rev. Cell Dev. Biol.*, 26(1):363–396, November 2010.

[96] B. Guo and W. H. Guilford. Mechanics of actomyosin bonds in different nucleotide states are tuned to muscle contraction. *Proc. Natl. Acad. Sci.*, 103(26):9844–9849, June 2006.

[97] F. Kong, A. J. Garcia, A. P. Mould, M. J. Humphries, and C. Zhu. Demonstration of catch bonds between an integrin and its ligand. *J. Cell Biol.*, 185(7):1275–1284, June 2009.

[98] S. Rakshit, Y. Zhang, K. Manibog, O. Shafraz, and S. Sivasankar. Ideal, catch, and slip bonds in cadherin adhesion. *Proc. Natl. Acad. Sci.*, 109(46):18815–18820, November 2012.

[99] Kristine Manibog, Hui Li, Sabyasachi Rakshit, and Sanjeevi Sivasankar. Resolving the molecular mechanism of cadherin catch bond formation. *Nat. Commun.*, 5:3941, 2014.

[100] Yuriy V. Pereverzev and Oleg V. Prezhdo. Force-induced deformations and stability of biological bonds. *Phy. Rev. E*, 73(5), May 2006.

[101] Wendy Thomas, Manu Forero, Olga Yakovenko, Lina Nilsson, Paolo Vicini, Evgeni Sokurenko, and Viola Vogel. Catch-bond model derived from allostery explains force-activated bacterial adhesion. *Biophys. J.*, 90(3):753–764, February 2006.

[102] O. Yakovenko, S. Sharma, M. Forero, V. Tchesnokova, P. Aprikian, B. Kidd, A. Mach, V. Vogel, E. Sokurenko, and W. E. Thomas. FimH forms catch bonds that are enhanced by mechanical force due to allosteric regulation. *J. Biol. Chem.*, 283(17):11596–11605, April 2008.

[103] Jizhong Lou and Cheng Zhu. A structure-based sliding-rebinding mechanism for catch bonds. *Biophys. J.*, 92(5):1471–1485, March 2007.

[104] Yuriy V. Pereverzev, Oleg V. Prezhdo, Manu Forero, Evgeni V. Sokurenko, and Wendy E. Thomas. The two-pathway model for the catch-slip transition in biological adhesion. *Biophys. J.*, 89(3):1446–1454, September 2005.

[105] Yuriy V. Pereverzev, Eugenia Prezhdo, and Evgeni V. Sokurenko. The two-pathway model of the biological catch-bond as a limit of the allosteric model. *Biophys. J.*, 101(8):2026–2036, 2011.

[106] V. Barsegov and D. Thirumalai. Dynamics of unbinding of cell adhesion molecules: Transition from catch to slip bonds. *Proc. Natl. Acad. Sci.*, 102(6):1835–1839, February 2005.

[107] Yohichi Suzuki and Olga K. Dudko. Single-molecule rupture dynamics on multidimensional landscapes. *Phys. Rev. Lett.*, 104(4):048101, January 2010.

[108] Yohichi Suzuki and Olga K. Dudko. Biomolecules under mechanical stress: A simple mechanism of complex behavior. *J. Chem. Phys.*, 134(6):065102, 2011.

[109] C. B. Korn and U. S. Schwarz. Dynamic states of cells adhering in shear flow: From slipping to rolling. *Phy. Rev. E*, 77(4):041904, April 2008.

[110] Z. M. Ruggeri. Von Willebrand factor, platelets and endothelial cell interactions. *J. Thromb. Haemost.*, 1(7):1335–1342, 2003.

[111] R. Descas, J.-U. Sommer, and A. Blumen. Static and dynamic properties of tethered chains at adsorbing surfaces: A Monte Carlo study. *J. Chem. Phys.*, 120(18):8831, 2004.

[112] C. Sendner and R. R. Netz. Hydrodynamic lift of a moving nano-rod at a wall. *Europhys. Lett.*, 79(5):58004, September 2007.

[113] C. E. Sing and A. Alexander-Katz. Non-monotonic hydrodynamic lift force on highly extended polymers near surfaces. *Europhys. Lett.*, 95(4):48001, August 2011.

[114] G. K. Batchelor. *An Introduction to Fluid Dynamics*. Cambridge University Press, 2000.

[115] John Happel and Howard Brenner. *Low Reynolds number hydrodynamics*, volume 1 of *Mechanics of fluids and transport processes*. Springer Netherlands, Dordrecht, 1981.

[116] Osborne Reynolds. An experimental investigation of the circumstances which determine whether the motion of water shall be direct or sinuous, and of the law of resistance in parallel channels. *Proc. R. Soc. Lond.*, 35(224-226):84–99, 1883.

[117] Sangtae Kim. *Microhydrodynamics: principles and selected applications*. Butterworth-Heinemann series in chemical engineering. Butterworth-Heinemann, Boston, 1991.

[118] Jens Rotne and Stephen Prager. Variational treatment of hydrodynamic interaction in polymers. *J. Chem. Phys.*, 50(11):4831, 1969.

[119] Hiromi Yamakawa. Transport properties of polymer chains in dilute solution: Hydrodynamic interaction. *J. Chem. Phys.*, 53(1):436, 1970.

[120] J. R. Blake. A note on the image system for a stokeslet in a no-slip boundary. In *Proc. Camb. Phil. Soc.*, volume 70, page 303–310, 1971.

[121] Yong Woon Kim and Roland R. Netz. Electro-osmosis at inhomogeneous charged surfaces: Hydrodynamic versus electric friction. *J. Chem. Phys.*, 124(11):114709, 2006.

[122] Burkhard Dünweg and Anthony J. C. Ladd. Lattice boltzmann simulations of soft matter systems. In Prof Christian Holm and Prof Kurt Kremer, editors, *Advanced Computer Simulation Approaches for Soft Matter Sciences III*, number 221 in Advances in Polymer Science, pages 89–166. Springer Berlin Heidelberg, January 2009.

[123] G. Gompper, T. Ihle, D. M. Kroll, and R. G. Winkler. Multi-particle collision dynamics: A particle-based mesoscale simulation approach to the hydrodynamics of complex fluids. In Prof Christian Holm and Prof Kurt Kremer, editors, *Advanced Computer Simulation Approaches for Soft Matter Sciences III*, number 221 in Advances in Polymer Science, pages 1–87. Springer Berlin Heidelberg, January 2009.

[124] C. E. Sing and A. Alexander-Katz. Dynamics of collapsed polymers under the simultaneous influence of elongational and shear flows. *J. Chem. Phys.*, 135(1):014902, 2011.

[125] M. Kraus, W. Wintz, U. Seifert, and R. Lipowsky. Fluid vesicles in shear flow. *Phys. Rev. Lett.*, 77(17):3685–3688, 1996.

[126] A. Serr and R. R. Netz. Enhancing polymer adsorption by lateral pulling. *Europhys. Lett.*, 78(6):68006, June 2007.

[127] Hsieh Chen and Alfredo Alexander-Katz. Polymer-based catch-bonds. *Biophys. J.*, 100(1):174–182, January 2011.

[128] Matthias Radtke and Roland Netz. Shear-induced dynamics of polymeric globules at adsorbing homogeneous and inhomogeneous surfaces. *Eur. Phys. J. E*, 37(3):20, March 2014.

[129] T. R. Einert, C. E. Sing, A. Alexander-Katz, and R. R. Netz. Conformational dynamics and internal friction in homopolymer globules: equilibrium vs. non-equilibrium simulations. *Eur. Phys. J. E*, 34(12):130, December 2011.

[130] Peter Hänggi, Peter Talkner, and Michal Borkovec. Reaction-rate theory: fifty years after Kramers. *Rev. Mod. Phys.*, 62(2):251–341, April 1990.

[131] H. Risken. *The Fokker-Planck equation: methods of solution and applications*. Number v. 18 in Springer series in synergetics. Springer-Verlag, New York, 2nd ed edition, 1996.

[132] H. Chen, M. A. Fallah, V. Huck, J. I. Angerer, A. J. Reininger, S. W. Schneider, M. F. Schneider, and A. Alexander-Katz. Blood-clotting-inspired reversible polymer–colloid composite assembly in flow. *Nat. Commun.*, 4:1333, January 2013.

[133] R. Schneppenheim and U. Budde. von Willebrand factor: the complex molecular genetics of a multidomain and multifunctional protein. *J. Thromb. Haemost.*, 9 Suppl 1:209–215, July 2011.

[134] Z. M. Ruggeri. Activation-independent platelet adhesion and aggregation under elevated shear stress. *Blood*, 108(6):1903–1910, September 2006.

[135] Matthias Radtke and Roland R. Netz. Shear-enhanced adsorption of a homopolymeric globule mediated by surface catch bonds. *Eur. Phys. J. E*, 38(6):69, June 2015.

[136] X. Zhang, K. Halvorsen, C.-Z. Zhang, W. P. Wong, and T. A. Springer. Mechanoenzymatic cleavage of the ultralarge vascular protein von Willebrand factor. *Science*, 324(5932):1330–1334, June 2009.

[137] Hans Ulrichts, Miklós Udvardy, Peter J. Lenting, Inge Pareyn, Nele Vandeputte, Karen Vanhoorelbeke, and Hans Deckmyn. Shielding of the A1 domain by the D'D3 domains of von Willebrand factor modulates its interaction with platelet glycoprotein Ib-IX-V. *J. Biol. Chem.*, 281(8):4699–4707, February 2006.

[138] Camilo Aponte-Santamaría, Volker Huck, Sandra Posch, Agnieszka K. Bronowska, Sandra Grässle, Maria A. Brehm, Tobias Obser, Reinhard Schneppenheim, Peter Hinterdorfer, Stefan W. Schneider, Carsten Baldauf, and Frauke Gräter. Force-sensitive autoinhibition of the von Willebrand factor is mediated by interdomain interactions. *Biophys. J.*, 108(9):2312–2321, May 2015.

[139] Zaverio M. Ruggeri. Platelets in atherothrombosis. *Nat. Med.*, 8(11):1227–1234, November 2002.

[140] Shaun P. Jackson. The growing complexity of platelet aggregation. *Blood*, 109(12):5087–5095, June 2007.

[141] Han-Mou Tsai. Pathophysiology of thrombotic thrombocytopenic purpura. *Int. J. Hematol.*, 91(1):1–19, January 2010.

[142] M. Furlan. Von Willebrand factor: molecular size and functional activity. *Ann. Hematol.*, 72(6):341–348, June 1996.

[143] J. E. Sadler. A new name in thrombosis, ADAMTS13. *Proc. Natl. Acad. Sci.*, 99(18):11552–11554, September 2002.

[144] J.-f. Dong. ADAMTS-13 rapidly cleaves newly secreted ultralarge von Willebrand factor multimers on the endothelial surface under flowing conditions. *Blood*, 100(12):4033–4039, December 2002.

[145] Junyi Ying, Yingchen Ling, Lisa A. Westfield, J. Evan Sadler, and Jin-Yu Shao. Unfolding the A2 domain of von Willebrand factor with the optical trap. *Biophys. J.*, 98(8):1685–1693, April 2010.

[146] Svenja Lippok, Matthias Radtke, Tobias Obser, Lars Kleemeier, Reinhard Schneppenheim, Ulrich Budde, Roland R. Netz, and Joachim O. Rädler. Shear-induced unfolding and enzymatic cleavage of full-length VWF multimers. *Biophysical Journal*, 110(3):545–554, February 2016. 1512.05127.

[147] Theo GM Van de Ven. *Colloidal hydrodynamics*. Academic Press, 1989.

[148] J.F. Morrison. Kinetics of the reversible inhibition of enzyme-catalysed reactions by tight-binding inhibitors. *Biochim. Biophys. Acta*, 185(2):269–286, August 1969.

[149] W. Cao, S. Krishnaswamy, R. M. Camire, P. J. Lenting, and X. L. Zheng. Factor VIII accelerates proteolytic cleavage of von Willebrand factor by ADAMTS13. *Proc. Natl. Acad. Sci.*, 105(21):7416–7421, May 2008.

[150] C. G. Skipwith, W. Cao, and X. L. Zheng. Factor VIII and platelets synergistically accelerate cleavage of von Willebrand factor by ADAMTS13 under fluid shear stress. *J. Biol. Chem.*, 285(37):28596–28603, September 2010.

[151] A. J. Xu and T. A. Springer. Mechanisms by which von Willebrand disease mutations destabilize the A2 domain. *J. Biol. Chem.*, 288(9):6317–6324, March 2013.

[152] Arjen J. Jakobi, Alireza Mashaghi, Sander J. Tans, and Eric G. Huizinga. Calcium modulates force sensing by the von Willebrand factor A2 domain. *Nat. Commun.*, 2:385, July 2011.

Abstract

A fundamental understanding of the dynamical behavior of biopolymers under non-equilibrium conditions is essential to the investigation of biological systems on the microscopic scale. The blood clotting protein von Willebrand factor presents a prominent example of current biophysical research on the relationship between structural and functional properties of multimeric proteins under flow conditions with the aim to explain and predict complex biological processes. The present thesis theoretically investigates several non-equilibrium phenomena associated with collapsed biopolymers in shear flow. Specifically, we explore shear-induced dynamics, adsorption, unfolding, activation, and degradation of von Willebrand factor and associated polymeric systems by means of Brownian hydrodynamics simulations using coarse-grained models.

We first examine the dynamics and adsorption behavior of a single collapsed homopolymer globule on homogeneous and inhomogeneous surfaces in shear flow. Dynamic state diagrams as a function cohesion, adhesion, and shear rate feature distinct dynamical adsorbed states being classified into rolling and slipping states, globular and coil-like states, as well as isotropic and prolate states. We observe stick-roll motion for highly corrugated inhomogeneous surface potentials due to high lateral surface friction. Despite low drift velocities and reduced hydrodynamic lift forces on such inhomogeneous surfaces that are entirely based on energy-conserving pair potentials, a shear-induced adsorption is not found.

Second, we study adsorption of a globule under shear on smooth surfaces with stochastic surface-monomer bonds whose two-state kinetics is characterized by the bond formation rate, bond dissociation rate and an effective catch bond parameter describing how force acting on a bond influences the dissociation rate. Constructing adsorption state diagrams as a function of shear rate and all three bond parameters, we find shear-induced adsorption in a small range of parameters for low dissociation and association rates and only when the bond is near the transition between slip and catch bond behavior. We argue that more elaborate potential-based models are necessary to observe catch bond behavior that allow for shear-induced surface adsorption phenomena.

Third, we show that the internal tension distribution along the contour of a globule in shear flow is inhomogeneous and above a threshold shear rate exhibits a double-peak structure. We argue that these tension maxima close to the termini of the polymer chain reflect the presence of polymeric protrusions and establish the connection to shear-induced globule unfolding. By means of heuristic scaling laws and an quasi-equilibrium theory, simulation results of average protrusion lengths and maximal tensions are analyzed. Our results are used to explain experimental data for the shear-sensitive enzymatic degradation of collapsed biopolymers. In particular, we relate the cleavage rate of von Willebrand factor in blood plasma to the probability of single cleavage sites to be accessible for the protease.

Kurzfassung

Ein fundamentales Verständnis des dynamischen Verhaltens von Biopolymeren unter Nicht-Gleichgewichtsbedingungen ist essentiell für die Untersuchung mikroskopischer biologischer Systeme. Das Blutgerinnungsprotein von-Willebrand-Faktor ist ein bedeutendes Beispiel für aktuelle biophysikalische Forschung über die Beziehung zwischen strukturellen und funktionellen Eigenschaften von multimeren Proteinen unter Flussbedingungen mit dem Ziel komplexe biologische Prozesse erklären und vorhersagen zu können. Die vorliegende Arbeit untersucht theoretisch verschiedene Nicht-Gleichgewichtsphänomene im Zusammenhang mit kollabierten Biopolymeren im Scherfluss. Insbesondere erforschen wir scher-induzierte Dynamik, Adsorption, Entfaltung, Aktivierung und Degradation des von-Willebrand-Faktors und ähnlichen Polymersystemen mittels Brownscher-Hydrodynamik-Simulationen und grobkörnigen Modellen.

Erstens untersuchen wir die Dynamik und das Adsorptionsverhalten eines kollabierten Homopolymer-Globules an homogenen und inhomogenen Oberflächen im Scherfluss. Die erfassten dynamischen Zustandsdiagramme als Funktion von Kohäsion, Adhäsion und Scherrate weisen unterschiedliche dynamische, adsorbierte Zustände auf, welche in rollende und gleitenden, globuläre und gewundene sowie isotrope und prolate Zustände klassifiziert werden. Stark gewellte, inhomogene Oberflächenpotentiale führen zu einer Anhaft-Roll-Bewegung aufgrund hoher Oberflächenreibung. Obwohl diese inhomogenen Oberflächen basierend auf konservativen Paarpotentialen zu geringen Driftgeschwindigkeiten und schwacher hydrodynamischer Liftkraft führen, wird keine scher-induzierte Adsorption beobachtet.

Zweitens studieren wir die Adsorption eines Globules im Scherfluss an glatten Oberflächen mit stochastischen Oberflächen-Monomer-Bindungen, deren Kinetik durch zwei Zustände und entsprechende Raten für Assoziation und Dissoziation von Bindungen sowie eines effektiven Catch-Bindungsparameters, der den Einfluss von Kraft auf die Dissoziation bestimmt, charakterisiert ist. Wir konstruieren Adsorptions-Zustandsdiagramme als Funktion der Scherrate und den drei Bindungsparametern und entdecken scher-induzierte Adsorption in einem kleinen Parameterbereich niedriger Assoziations- und Dissoziationsraten und nur für Bindungen nahe dem Übergang von Slip- zu Catch-Bindungsverhalten. Wir zeigen, dass kompliziertere potentialbasierte Modelle nötig sind, um Catch-Bindungen zu erhalten, die scher-induzierte Oberflächenadsorption erlaubt.

Drittens zeigen wir die inhomogene, interne Spannungsverteilung entlang der Kontour eines Globules im Scherfluss, welche über einer Grenzscherrate eine Doppel-Peak-Strukture aufweist. Spannungsmaxima nahe der Polymerenden sind auf die Existenz von Polymer-Protrusionen zurückzuführen, wobei der Zusammenhang mit scher-induzierter Globule-Entfaltung hergestellt wird. Mittels heuristischer Skalengesetze und einer Quasigleichgewichtstheorie werden mittlere Protrusionslängen und maximale Spannungen analysiert. Unsere Ergebnisse werden genutzt, um experimentelle Daten von scher-sensitiver enzymatischer Degradation von kollabierten Biopolymeren zu erklären. Insbesondere wird die Spaltungsrate des von-Willebrand-Faktors in Blutplasma mit der der Wahrscheinlichkeit zugänglicher Spaltungsstellen für die Protease in Verbindung gesetzt.

Erklärung

Hiermit erkläre ich, dass ich die vorliegende Dissertationsschrift mit dem Titel

Shear-induced Phenomena of a Collapsed Polymer

selbständig angefertigt und hierfür keine anderen als die angegebenen Hilfsmittel verwendet habe. Die Arbeit ist weder in einem früheren Promotionsverfahren angenommen noch als ungenügend beurteilt worden.

Berlin, 2. März 2016